

---

# **Optical spectroscopy of micro- and nano-structured semiconductors**

---

Der Fakultät für Physik der  
Universität Duisburg-Essen  
vorgelegte Dissertation zum Erwerb eines  
Doktors für Naturwissenschaften

von

**Aswin Asaithambi**

aus

Tamil Nadu, India

Tag der Disputation: 28. Januar 2020

Erstgutachter: Prof. Dr. Axel Lorke

Zweitgutachter: Prof. Dr. Andreas Wieck

# DuEPublico

Duisburg-Essen Publications online

UNIVERSITÄT  
DUISBURG  
ESSEN

*Offen im Denken*

ub | universitäts  
bibliothek

Diese Dissertation wird über DuEPublico, dem Dokumenten- und Publikationsserver der Universität Duisburg-Essen, zur Verfügung gestellt und liegt auch als Print-Version vor.

**DOI:** 10.17185/duepublico/71317

**URN:** urn:nbn:de:hbz:464-20200302-151811-2

Alle Rechte vorbehalten.

*யாதும் ஊரே! யாவரும் கேளிர்!*

"Yaadhum Oore Yaavarum Kelir"

*Everywhere is our place, everyone our kin*

---

Kaniyan Pungundranar  
(Tamil astronomer)



# Zusammenfassung

Den Schwerpunkt dieser Dissertation bilden Photolumineszenz (PL)-untersuchungen von drei Halbleitermaterialien: Silizium-Nanopartikel, WS<sub>2</sub>-Monolagen und BODIPY- Mikrostäbchen. Silizium Nanopartikel (Durchmesser 3 nm) gehören zu den sogenannten Quantenpunkten, d.h. sie zeigen in diesem Größenbereich Quanteneffekte. WS<sub>2</sub>-Monolagen gehören zur Klasse der zweidimensionalen Halbleiter und BODIPY-Mikrostäbchen zur Klasse der organischen Halbleiter.

Die Emissionseigenschaften von Siliziumnanopartikeln (SiNP) wurden mittels PL Spektroskopie untersucht. Die SiNP-Ensembles zeigten eine breite PL-Emission, deren Breite durch die Größenstreuung bedingt ist. Sie zeigten außerdem ein gestrecktes exponentielles PL-Abklingverhalten. Die SiNP wurden auf Si/SiO<sub>2</sub>-, Ag- und Au-Substrate zur Untersuchung ihrer Wechselwirkung mit den Substraten abgeschieden. Kleine Agglomerate hatten eine PL-Lebensdauer von 54  $\mu$ s auf Si/SiO<sub>2</sub>-Substrat, welche deutlich auf 37  $\mu$ s bzw. 32  $\mu$ s reduziert wurde auf Gold- und Silbersubstraten. Diese Reduktion der PL-Lebensdauer ist auf den SEF-Effekt (*Surface Enhanced Fluorescence*) zurückzuführen. Es zeigte sich, dass Silber am besten geeignet ist, um die PL von SiNP zu verstärken. Infolge dieser Verstärkung konnten spektroskopische Untersuchungen an Si-Einzelpartikel auf einer Silberoberfläche durchgeführt werden. Einzelne SiNP „blinkten“, was auf das Vorhandensein einer Auger-Rekombination im Nanopartikel zurückgeführt wird. Statistiken der 'An' und 'Aus' -Zeiten folgen einem Potenzgesetz. Auch spektrales Wandern von einzelnen SiNP wurde beobachtet, welches auf den *Quantum Confined Stark Effect* zurückzuführen ist.

Es wurden zwei Chargen von WS<sub>2</sub>-Monolagen, die durch chemische Gasphasenabscheidung gewachsen wurden, mittels temperatur- und anregungsleistungsabhängiger PL-Spektroskopie untersucht. PL-Spektren, die bei niedrigen Temperaturen aufgenommen wurden, zeigen neben der exzitonischen Emission eine zusätzliche defektkorrelierte Emissionsbande. WS<sub>2</sub>-Monolagen aus der ersten Charge zeigten bereits nach dem Wachstum eine defektkorrelierte Emissionsbande (D<sub>0</sub>), während dies für Charge zwei nicht der Fall war. Durch Bestrahlung der WS<sub>2</sub>-Monolagen mit verschiedenen Xe<sup>30+</sup> -Ionenflüssen wurden unterschiedliche Defektdichten erzeugt. Charge eins zeigte danach die gleiche Emissionsbande wie zuvor und Charge zwei zeigte zwei neue defektkorrelierte Emissionsbanden D<sub>1</sub> und D<sub>2</sub>. Mittels anregungsleistungsabhängiger PL- und anschließenden Temperaturzyklen wurden alle diese defektkorrelierten Emissionen verändert und Defekte unter hoher Laserleistung (1 mW) z.T. umgewandelt. Ein möglicher Ursprung der defektkorrelierten Emission wird diskutiert.

Die PL-Spektroskopie mikrometergroßer kristalliner BODIPY-Stäbchen zeigte, dass jedes Stäbchen charakteristisches, sichtbares Licht unterschiedlicher Farbe emittiert. Für eine Sorte wurden optische Heterostrukturen, d.h. spektral unterschiedlich emittierender Bereiche innerhalb eines einzigen Stäbchens, beobachtet. Raumtemperatur PL-Spektren von grünen und roten Stäbchen zeigten mehrere Lumineszenzbanden, die auf das Vorhandensein von Mikrodomänen hindeuten. Temperaturabhängige PL-Messungen untermauerten dies, da mit sinkenden Temperaturen die rote Emission abnimmt und die grüne Emission zunimmt. Diese Beobachtungen werden mittels eines Modells basierend auf kristallinem Polymorphismus diskutiert. PL im grünen Spektralbereich zeigte eine Reihe von scharfen Linien bei Energien, die einer 1/n<sup>2</sup> -Beziehung folgen. Ein solches Verhalten, das von Rydberg-Atomen und Wannier-Exzitonen bekannt ist, wurde hier nicht erwartet. Emissionen mit den Hauptquantenzahlen von n = 3 bis n = 16 wurden beobachtet. Diese Beobachtungen werden anhand des Wannier-Exzitonenmodells untersucht.



# Abstract

This dissertation mainly contains photoluminescence (PL) studies of three semiconductor material systems: silicon nanoparticles, WS<sub>2</sub> monolayers and boron-dipyrromethene (BODIPY) micro-rods. Silicon nanoparticles (diameter  $\approx 3$  nm) are quantum dots, that is, they show quantum confinement at this size regime. WS<sub>2</sub> monolayers are two-dimensional semiconductors, and BODIPY micro-rods are organic semiconductors.

The emission characteristics of silicon nanoparticles (SiNP) were investigated via PL spectroscopy. An ensemble of SiNP shows broad PL emission, with broadness due to size dispersion and exhibit a stretched exponential PL decay behaviour. The SiNP are deposited on Si/SiO<sub>2</sub>, Ag and Au substrates to study their interaction with the substrates. Small agglomerates have PL lifetime of 54  $\mu$ s on Si/SiO<sub>2</sub> substrate, which was reduced to 37  $\mu$ s and 32  $\mu$ s on gold and silver substrates respectively. This reduction in the PL lifetime is due to the surface-enhanced fluorescence (SEF) effect. We show that, silver is best suited to enhance the PL of SiNP. As a result of this enhancement, single particle spectroscopic studies could be performed on SiNP on a silver surface. Single SiNP show PL blinking and this is attributed to the presence of Auger recombination in the nanoparticle. Statistics of 'on' and 'off' times reveal a power law behaviour. Also, spectral jittering of the PL from single SiNP was observed which is due to quantum-confined Stark effect.

Two batches of WS<sub>2</sub> monolayers grown via chemical vapour deposition were investigated via temperature and excitation power dependent PL spectroscopy. Low temperature PL spectra show, besides excitonic emission, an additional emission band due to a defect bound exciton recombination. Pristine WS<sub>2</sub> monolayers from batch one show intrinsic defect bound emission band (D<sub>0</sub>) while batch two shows no defect bound emission at low temperature. Different densities of defects were introduced by irradiating the WS<sub>2</sub> monolayers with different fluences of Xe<sup>30+</sup> ions. Batch one shows the same defect related emission band as before and batch two show two defect bound emission bands D<sub>1</sub> and D<sub>2</sub>. With excitation power dependent PL and temperature cycles, all these defect bound emission were altered and defects were partially transformed with high laser power (1 mW) exposure. A possible origin of the defect bound emission is discussed.

PL spectroscopy of micrometer-size BODIPY crystalline rods reveal that each rod displays characteristic visible light emission of different color. In a particular case, optical heterostructures with discrete, differently colored sections are observed within a single micro-rod. PL spectra of green and red rods at room temperature show multiple contributions, indicating the presence of micro domains. Temperature dependent PL measurements further confirm this, as red emission decreases and green emission increases at lower temperatures. These observations are discussed as a result of crystalline polymorphism. PL from the green region of the spectrum show a set of peaks with energies that follow a  $1/n^2$  rule. Such behaviour is known from Rydberg atoms and Wannier excitons, but it is unexpected for the present PL study of organic semiconductors. Emissions from the principal quantum levels up to  $n = 16$  and down to  $n = 3$  were observed. These findings are discussed using the Wannier exciton model.



# Introduction

Technologies related to micro- and nano- structured materials come under the well known bracket called nanotechnology. Nanotechnology has revolutionized a lot of products starting from phones, televisions etc of an individual to the use of nanotech in large industries. Also, looking at very small things paved the way towards interesting science. For example, bulk gold appears yellowish in colour, but, gold nanoparticles are red in colour due to surface plasmon resonance. [Anderson99] Noble metals are well known for their catalytic behaviour, [BOND74] nanoparticles of such metals are even a better catalyst than their bulk due to larger surface to volume ratio. [Pei19, Xu15] Moving on from metals to semiconductors; semiconductor materials are the most important component in any electronic device. The most exploited semiconductor so far is silicon, all the electronic devices are based on silicon and hence the name Silicon valley came about for an area in California where most of the tech companies in today's world are based. Besides silicon with its indirect bandgap [Cardona66], there are several other direct bandgap semiconductors such as GaAs, CdSe, etc [Richard04] in use today especially in the field of optoelectronics. Nanoparticles of these semiconductors have different bandgap values according to their size compared to that of their bulk counterparts. Direct bandgap semiconductors with bandgap values in the visible range are robust and excellent light emitters. [Klimov10] Different bandgaps indicate differently coloured light, this led to the invention of LEDs. Whilst green and red LEDs were known for decades, the challenge of producing efficient blue LEDs were only solved recently, for which a Nobel prize was awarded in the year 2014. A combination of red, green and blue light gives a white light, hence, energy and cost-effective white LEDs can be produced. Semiconductors in the nano-regime can undergo what is known as quantum confinement effect, hence these materials are called quantum dots (QDs) if they are quantum confined in all three dimensions. As a result, bandgap widens and bands become single energy levels (QDs are also called artificial atoms), resulting also in single-photon emitters. [Klimov10] This is crucial for developing quantum devices such as a quantum computer. [Lent97] Also, QDs such as CdSe are excellent light emitters and like every QDs, show size-dependent bandgap and light emission properties. This property has been exploited in the television technologies for better color contrast and since it is an array of nanoparticles, curved televisions can also be produced. CdSe, however, contains heavy metal and are toxic to the living being. [Godt06] These materials should be replaced by non-toxic, luminescent materials. It would be interesting to replace these with silicon technology, where currently, efforts are made to epitaxially grow III-V semiconductors directly on silicon. Also, silicon nanoparticles might open another route to improve the light emitting properties of silicon. In part II of this thesis, we try to improve the light emission of silicon by using silicon nanoparticles (SiNP) and additionally using metal films that can enhance the radiative rate of SiNP. Single particle spectroscopy of SiNP was also performed to understand the luminescence properties of single SiNP. Nanotechnology also includes two dimensional (2D) materials such as graphene. Graphene is a single layer of carbon

and has  $SP^2$  hybridized bonds between them, it is a zero bandgap material and theoretically has excellent conductivity and is much stronger than steel. [Frank07, Neto09] Graphene is expected to be a crucial component in electronics and already has been used in many industries e.g textile industries. [Alonso18] In the field of electronics, materials with suitable bandgaps are needed to build the necessary devices. Transition metal di-chalcogenide (TMDC) monolayers are a class of materials, that are three atoms thick and has a direct bandgap at the K-point in the Brillouin zone. Different TMDC monolayers can exhibit different bandgaps, use of these monolayers in stacks can result in excellent electronic devices due to easy integration of material combinations of metal-like, semiconducting or insulating sheets, opening up an enormous playground. [Wang12, Withers15] They are expected to be an upgrade to the present day electronics along with miniaturization. But, one massive obstacle in realizing the potential of these materials is the defects present in them, which hinders both their optical and transport properties. In part III, defects in  $WS_2$  monolayers are studied via temperature and power dependent photoluminescence (PL) spectroscopy, and we show that defects can also be transformed by simple exposure to higher powers ( $\approx 1$  mW) of laser light. For almost every inorganic material based devices, organic materials could also be used. Organic electronics are still on the rise, especially in photovoltaics. One of the major challenges in working with organic materials compared to an inorganic counterpart is that the bandgap engineering in inorganic semiconductors are well studied and established. [Fox17] In part IV of this thesis, we study the optical properties of BODIPY micro-rods. BODIPY is a class of organic dye molecules that have found much interest in the field of laser technology, solar cell concentrators, fluorescent labels, LEDs and chemical sensing. [Ehrenschwender11, Monsma89, Shah90, Altan Bozdemir11, Tang87] In this thesis, polymorphism in a single crystalline micro-rod is studied in detail using photoluminescence spectroscopy.

The dissertation can be divided into five parts containing eight chapters and are structured as the following:

- Part I contains two chapters describing the basics of photoluminescence spectroscopy and the experimental set-up used.
  - Chapter 1 describes the essential theory about photoluminescence (PL), band structures, interband luminescence, and excitons. The descriptions are general and are essential for understanding the specialized theories described in the following chapters.
  - Chapter 2 contains the main experimental set-up ( $\mu$ -PL) used. All the components of the set-up are described in detail.
- Part II contains two chapters containing the results from the investigation of PL from silicon nanoparticles with flourine shell.
  - Chapter 3 contains the results and discussion from the spectral and temporal PL studies of SiNP in the vicinity of metal films.
  - Chapter 4 is an extension of chapter 3, where results from single particle spectroscopic studies of SiNP are discussed.
- Part III contains one chapter containing the results and discussion about defect-bound PL emissions from  $WS_2$  monolayers.

- Chapter 5 contains the defect-related PL studies of WS<sub>2</sub> monolayers. The nature of the optically active defects and laser induced defect engineering have been studied in this chapter.
- Part IV contains two chapters containing the spectroscopic characterization of BODIPY semiconducting micro-rods.
  - Chapter 6 contains the spectroscopic characterization of green and red emitting BODIPY rods and the discussion of the results.
  - Chapter 7 is an extension of chapter 6 in which the observation of Rydberg like states in the green emission band of the BODIPY rod is presented.
- Part V contains chapter 8, where results from the previous chapters are summarized and a possible outlook for further work is given.

# Contents

I	General Introduction . . . . .	1
1	Basics of photoluminescence spectroscopy . . . . .	2
1.1	Photoluminescence . . . . .	2
1.2	Bandstructure . . . . .	3
1.3	Interband luminescence . . . . .	4
1.4	Exciton . . . . .	5
2	Experimental set up . . . . .	8
II	Optical spectroscopy of Silicon nanoparticles . . . . .	11
3	Spectral and temporal photoluminescence of ensemble silicon nano-particles in the vicinity of metal films . . . . .	12
3.1	Motivation . . . . .	12
3.2	Band structure . . . . .	13
3.3	Sample synthesis and fabrication . . . . .	14
3.4	Surfaced enhanced PL spectroscopy . . . . .	17
3.5	Results and discussion . . . . .	19
3.5.1	Steady-state and temporal PL properties of ensemble SiNP . . . . .	19
3.5.2	Steady-state PL properties of ensemble SiNP on different substrates . . . . .	21
3.5.3	Time resolved PL properties of ensemble SiNP on different substrates . . . . .	22
3.6	Conclusion . . . . .	25
4	Single silicon-dot spectroscopy . . . . .	26
4.1	Motivation . . . . .	26
4.2	Sample fabrication . . . . .	26
4.3	Results and discussion . . . . .	28
4.4	Conclusion . . . . .	32
III	WS <sub>2</sub> monolayers . . . . .	33
5	Defect studies on WS <sub>2</sub> monolayers . . . . .	34
5.1	Motivation . . . . .	34
5.2	Sample synthesis and fabrication . . . . .	34
5.3	Bandstructure . . . . .	35
5.4	Results and discussion . . . . .	38
5.4.1	WS <sub>2</sub> sample batch 1 . . . . .	38
5.4.2	WS <sub>2</sub> sample batch 2 . . . . .	47
5.5	Comparison between batch 1 and 2 . . . . .	61
IV	Crystalline BODIPY semiconductor rods . . . . .	62
6	Spectroscopic characterisation of BODIPY crystalline rods . . . . .	63
6.1	Motivation . . . . .	63

---

6.2	Sample synthesis and fabrication . . . . .	63
6.3	Results and discussion . . . . .	64
6.4	Conclusion . . . . .	71
7	Rydberg like states in BODIPY rods . . . . .	72
7.1	Motivation . . . . .	72
7.2	Results and discussion . . . . .	72
7.3	Conclusion . . . . .	78
V	Summary and Outlook . . . . .	79
8	Summary and Outlook . . . . .	80
A	Appendix . . . . .	93

**Part I**

**General Introduction**

# Chapter 1

## Basics of photoluminescence spectroscopy

In this chapter, the theory of photoluminescence (PL) spectroscopy is explained using solid semi-conducting systems. Contents and figures in this chapter were taken from the books from [Yu10] and [Fox02].

### 1.1 Photoluminescence

The spontaneous emission of light as a result of a system transitioning from an excited state to a ground state is called luminescence. There are different types of luminescence depending on the excitation of the system to excited states, for example, electro-luminescence, where a system is excited electrically or photo-luminescence where excitation is due to absorption of photons. There are a variety of parameters that influence the luminescence characteristics like the system under study, temperature, and the states (excited and ground) that can be discrete like in atoms and quantum dots or a band like in bulk semiconductors.

Figure 1.1 shows an overview of the different processes involved in photo-luminescence. PL involves, firstly, the excitation of the charge carrier from the ground state to the excited state leaving a hole in the ground state. In most cases, the excitation energy is much larger than required thus resulting in a higher excited state of the system. Secondly, the excited charge carrier relaxes to the lowest point of the conduction band in case of semiconductors or lowest excited discrete level in case of atoms and quantum dots, this process is called the relaxation process. Lastly, the excited charge carrier spontaneously relaxes into the ground state (with holes in it, else, Pauli's exclusion principle will prevent this process) via emitting a photon in due process (radiative recombination). Note, not all the transitions will result in photon emission, some relax non-radiatively without photon emission.

In the case of two-level system, the spontaneous emission rate depends on the number of excited charge carriers ( $N$ ) and the radiative rate at which these charge carriers relax into the ground state. This relation is given in equation 1.1 where  $\Gamma_r$  is the radiative rate and  $K_{nr}$  is the non-radiative rate.

$$\frac{dN}{dt} = -(\Gamma_r + K_{nr})N \quad (1.1)$$

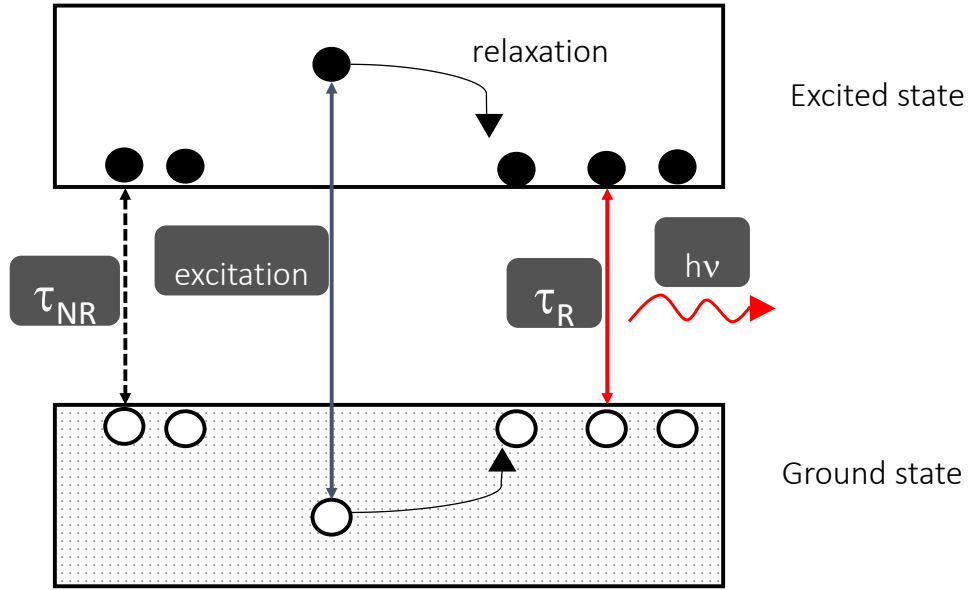


Figure 1.1: Schematic representation of PL in a solid semiconductor, black solid circles represent electrons and white solid circles represent holes.

$$N(t) = N(0)e^{-(\Gamma_r + K_{nr})t} = N(0)e^{-\left(\frac{1}{\tau_r} + \frac{1}{\tau_{nr}}\right)t} \quad (1.2)$$

The solution to this rate equation is given in equation 1.2 where  $N(t)$  is the number of excited charge carrier at time  $t$ ,  $N(0)$  is the number at time  $t = 0$ ,  $\Gamma_r$  is the radiative rate and inverse of which is the excited state radiative lifetime  $\tau_r$ .

## 1.2 Bandstructure

As mentioned earlier, this thesis deals with semiconducting systems (Si, WS<sub>2</sub> monolayers and BODIPY rods) and hence to study the PL from these systems, it is imperative to understand the bandstructure in a semiconductor system. Atoms and molecules have discrete occupied and unoccupied energy levels and these atoms and molecules grow or pack in a certain way to form crystal structures. These atoms have their distinct atomic/molecular orbitals. And when they are specifically placed in their positions in the crystal (lattice) at certain distances and direction from each other, new sets of energy levels and more often bands are formed as a result of the linear combination of those atomic orbitals (LCAO) which is in fact a method for bandstructure construction (using the interaction between atomic states/orbitals). The calculation of bandstructures are explained in detail in several books (content in this section were taken from [Yu10]) and is beyond the scope of this thesis, just to provide a gist, electronic wavefunctions are solved with the help of rotational and translational symmetry of the ideal crystal lattice. The electrons in the crystal lattice follow the Schrödinger equation 1.3 and the hamiltonian is given in equation 1.4 in a one electron time-independent picture.

$$H_e(\psi(\vec{r})) = E(\psi(\vec{r})) \quad (1.3)$$

$$H_e = -\frac{\hbar^2}{2m}\nabla^2 + V(\vec{r}) \quad (1.4)$$

$$\psi_k(\vec{r}) = e^{ik\vec{r}}u_k(\vec{r}) \quad (1.5)$$

Applying the symmetry operation, due to the invariance upon symmetry operations in crystals reduces the complexity of calculating the band structure. When a particle moves in a periodic potential ( $V(\vec{r})$ ) its wavefunction can be expressed in the form of Bloch functions as described in equation 1.5 where  $u_k(\vec{r})$  is the periodic function with the same periodicity as  $V(\vec{r})$  and  $\psi_k(\vec{r})$  is known as Bloch function. This is the basis for several different models to calculate the band structure of a semiconductor (for example LCAO method, k.p method, etc). For this thesis, only the top most filled band called valence band and the lowest empty band called conduction band separated by a bandgap are important, the bandgaps of the semiconductors studied in this thesis are in the order of 1-2 eV depending on the system.

### 1.3 Interband luminescence

Most conventional semiconductors such as GaAs and CdSe have a direct bandgap at the  $\Gamma$ - point in momentum space. Most 2D materials such as transition metal di-chalcogenide monolayers have a direct bandgap at the K point in momentum space, which is described in slightly more detail in chapter 5. Silicon, on the other hand has its valence band maximum at the  $\Gamma$ - point and conduction band minimum in between the  $\Gamma$ - point and the X- point in momentum space, this makes the excitation and emission process different to that of semiconductors with a direct bandgap given the momentum difference between the valence band maximum and the conduction band minimum in indirect bandgap semiconductors.

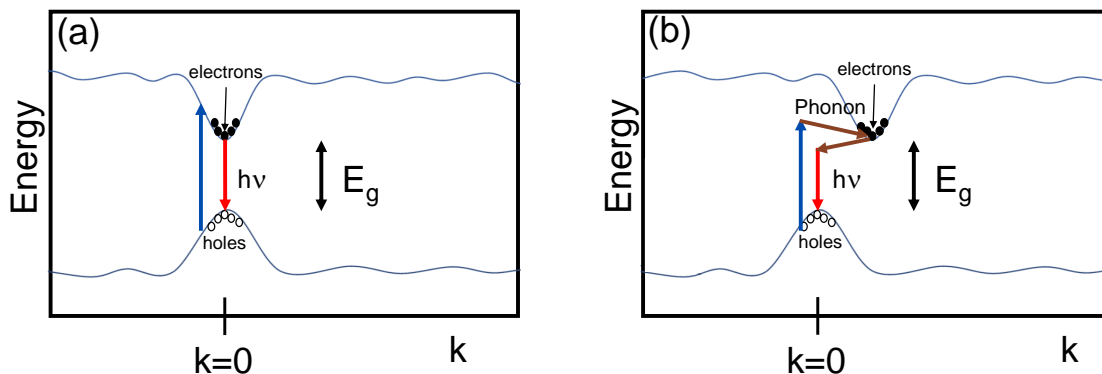


Figure 1.2: PL excitation and emission process in (a) direct band gap semiconductor and (b) indirect band gap semiconductor. Note that this is just a schematic, phonon emission is shown in the schematic, absorption is also possible.

Figure 1.2a shows the excitation and emission behaviour in a direct bandgap semiconductor with bandgap  $E_g$  and Figure 1.2b shows the excitation and emission behaviour in an indirect bandgap semiconductor with the bandgap  $E_g$ . In case of direct bandgap semiconductors, the optical excitation process involves absorption of a photon with energy larger than the bandgap and thereby transfer energy and momentum to the electron in the valence band to overcome the bandgap to reach the conduction band. Because the momentum transferred from the photon is much less than possible electronic momentum within the Brillouin zone, the electron and hole have the same momentum after the transition which is zero in case of the  $\Gamma$ - point. The emission process occurs similarly and the excited state lifetime is usually in the order of few nanoseconds. In case of indirect bandgap semiconductors, valence band maximum and conduction band minimum are at different points in the Brillouin zone, that means, conservation of momentum requires that a phonon must either be emitted or absorbed during the excitation and emission process. Such requirements make the transition probability small and make them a poor light emitter and absorber when compared to a direct bandgap semiconductor. Excited state lifetime is usually larger and depends heavily on the temperature. For example, Si at room temperature has an excited state lifetime in the order of microseconds and at low temperature (10 K) in the order of milliseconds.

## 1.4 Exciton

In the previous sections, it was said that the excitation process results in the accumulation of electrons in the conduction band and holes in the valence band. The coulomb attraction in these situations had been neglected. Because of the attractive force between electron and hole, they tend

to stay together making them a quasi-particle called exciton.

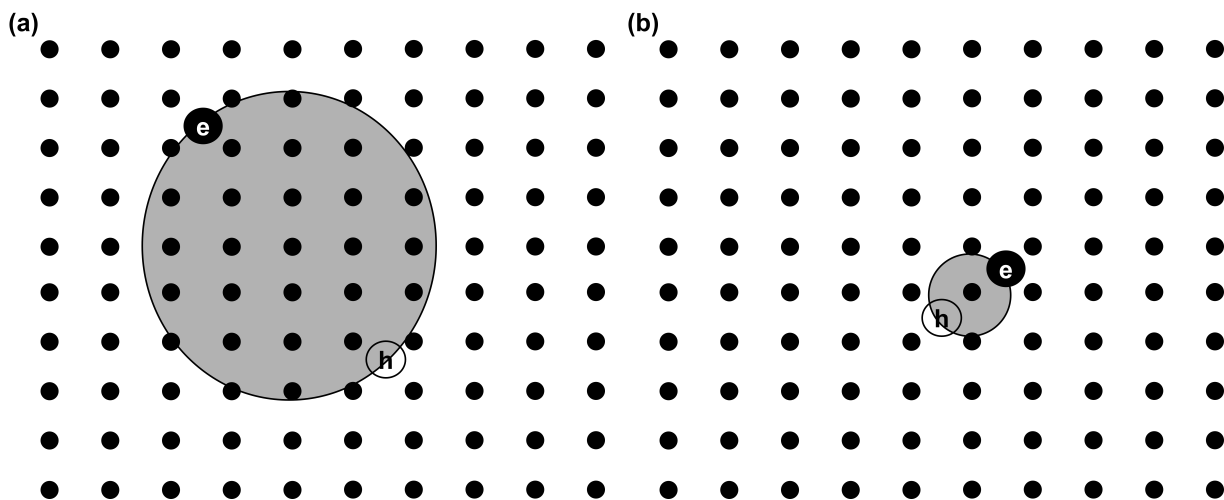


Figure 1.3: (a) Free exciton or Wannier-Mott exciton in a solid and (b) tightly bound exciton or Frenkel exciton in a solid.

Excitons are observed in a wide range of materials, there are two basic types of excitons: Wannier-Mott exciton or free exciton (see Figure 1.3a), Frenkel exciton or tightly bound exciton (see Figure 1.3b) and there is a third kind called Rydberg excitons, which essentially is a Wannier-Mott exciton in higher principal quantum states, where the electron-hole separation is much larger than that of the ground state. The binding energy of the Wannier-Mott exciton of  $\approx 10$  meV is much lower than that of the Frenkel excitation ( $\approx 200$  meV). Due to this fact, observation of the Wannier-Mott exciton (in semiconductors such as GaAs, CdSe etc.) recombination at room temperature is slightly improbable as the thermal energy with temperature (T) goes as  $k_B T$  ( $\approx 25$  meV at RT) provides enough energy to split the electron and hole. In case of a Frenkel exciton, electron and hole do not see the lattice as one dielectric, it is rather tightly bound to one atom or molecule in the lattice, Frenkel excitons are more commonly observed in organic semiconductors. In free exciton model or weakly bound exciton (Wannier-Mott exciton), the electron-hole separation is much larger than the inter-atomic distance and thus, it is a good approximation to average the detailed structures of atoms between electron and hole and consider the exciton as a free moving particle in a dielectric medium. Thereby, interaction in a free exciton model can be considered as that of a hydrogenic system. The internal structure of the movement of electron in a hydrogen atom is given by the equation 1.6 (via the Bohr model), which will be discussed in detail in chapter 7.  $R_H$  is the Rydberg constant of 13.6 eV and  $n$  is the principal quantum number. In case of a free exciton, since the exciton moves in a dielectric, equation 1.6 is then modified to equation 1.7, where  $\mu$  is the reduced mass,  $\epsilon_r$  is the relative dielectric constant and  $R_X$  is the effective Rydberg constant or exciton Rydberg constant.

$$E(n) = -\frac{R_H}{n^2} \quad (1.6)$$

$$E(n) = -\frac{\mu}{m_0} \frac{1}{\epsilon_r^2} \frac{R_H}{n^2} = -\frac{R_X}{n^2} \quad (1.7)$$

## 1.4. EXCITON

---

The energy of the exciton created, including the Coulomb interaction is given by the equation 1.8. The optical probing of these principle quantum states in semiconductors have been realized, for example, via transmission spectroscopy and absorption spectroscopy in  $\text{Cu}_2\text{O}$ . [Kazimierzuk14] Chapter 7 discusses such principle quantum states in BODIPY rods with PL spectroscopy.

$$E_n = E_g - \frac{R_X}{n^2} \quad (1.8)$$

Coulomb interaction between the electron and hole in the exciton effectively reduces the optical transition energy as described in equation 1.8. Therefore the energy of an exciton recombination is always less than the bandgap energy of the semiconductor.

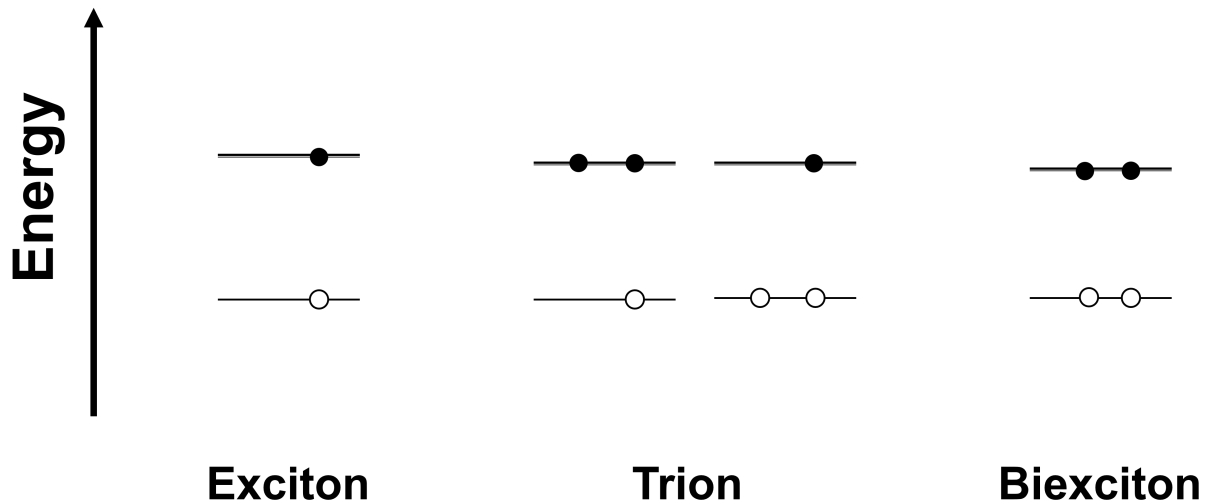


Figure 1.4: Schematics of different excitonic complexes (exciton ( $X_0$ ), trion ( $X^{(+/-)}$ ) and biexciton ( $XX$ )) and their energy levels in a semiconductor.

In optical spectroscopy, for a direct bandgap system, there is a finite probability of observing exciton complexes such as trion and biexciton, which shows different transition energies due to the further coulomb interaction with the additional charges. Figure 1.4 shows the schematics of a typical semiconductor that shows exciton, trion and biexciton in them. Depending on the size of the semiconducting system, it is possible to observe these complexes in the PL spectroscopy. For example, if the size of the semiconducting system is sufficiently small, i.e., in case of quantum dots, recombination of such complexes may result in non-radiative Auger recombination, which is one of the reasons for PL intermittency in a single quantum dot. This phenomenon is explained in detail in chapter 4. In case of 2D semiconducting materials such as  $\text{WS}_2$  (the study of  $\text{WS}_2$  explained in chapter 5), exciton binding energy is large due to less dielectric screening, PL emission due to trions and biexcitons is rather a common sight in a large semiconductors structures such as quantum wells as the size is constrained only in one dimension.

# Chapter 2

## Experimental set up

The experimental set-up is described in this chapter. Photoluminescence spectroscopy had been the main technique used in this thesis, for getting an insight into the different nano and micro semiconducting structure. The PL facility used is a micro PL set-up. A schematic of the set-up is shown in Figure 2.1. As explained in the previous chapter 1, regarding the theory of PL spectroscopy, it requires three main components to perform the PL measurements: an excitation source, a system that interacts with the incident light and a detector that senses the emitted light. To explain the set-up in more detail, different components of the set-up described in the schematics in Figure 2.1, shall be explained from the excitation to the detection of the emitted photon.

Starting with the excitation source, there are four different lasers available, two green lasers (532 nm) and two blue lasers (405 nm). Although only two of them had been used for the experiments described in this thesis, those are Oxxius LMX-532S-300 series solid-state continuous wave (CW) laser with up to 300mW excitation power at 532 nm and a Linos model Nano 250 CW diode laser at 405 nm. In each case, the excitation photon/laser light is coupled into a single mode optical fiber (2.5  $\mu\text{m}$  core diameter). The use of optical fibers allows more flexibility in the set-up as they can be moved around without disrupting the entire alignment. On the downside, these fibers have a breaking threshold of 3 mW and hence, the maximum excitation power had been limited to 1.5 mW for any experiments involving the single mode optical fiber. These in-coupled streams of photons are continuous waves, i.e., there is a constant flow of photons. For time resolved PL decay measurements, a pulsed laser is a requisite. For pulsing the green excitation source, which is used in chapter 3, the photons from the CW laser pass through an acousto optical modulator (AOM), where the CW laser light are pulsed (with pulse duration of 200 ms and total time of 1500 ms before the next pulse) and coupled into a single mode optical fiber.

The optical fibers are then guided and fixed to the respective arms for the green in top and blue in bottom of the microscope head as shown in Figure 2.1. Light from the fibers is collimated using an 4X objective in the excitation arms and goes through a line filter that filters out the non-resonant modes of the laser. The only difference is that a grey filter wheel for excitation power modulation is placed in the arm, after the 4X objective for the blue light whereas the filter wheel is placed in front of the laser itself before the in-coupling of light into the fiber, in case of the green light. The laser light is then incident on steep-edge dichroic for the green or blue laser, respectively. At the dichroic, 99.8 % of laser light is reflected downwards to a 50X ultra long working distance objective with a numerical aperture (NA) of 0.5, which can be moved in the z-direction to change focus. This objective lens has a working distance of 13 mm, which is unusually large for a 50X objective.

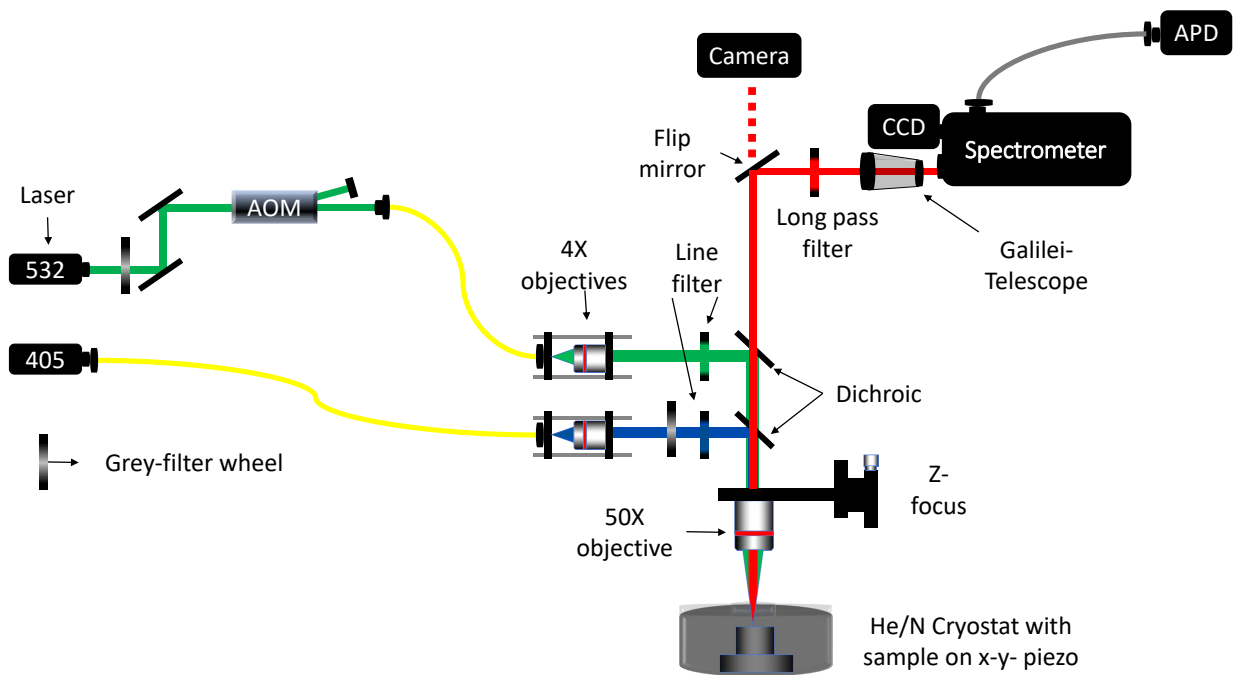


Figure 2.1: Schematic of the PL spectroscopy set-up, description of the set-up is explained in detail in the text.

The second component is the system/material under study in different environments. One of the main advantages of this set-up is that, the system/sample can be placed under different conditions by just having different stages. To emphasize a little more on this flexibility, the sample can be placed on an electrically driven motor stage with multiple degrees of freedom, the sample can be placed in a cryostat or a micromanipulator can be used etc. The work explained in this thesis involves, mainly two stages. One is the motor controlled stage with two degrees of freedom, where RT measurements can be performed on an encoded electrically driven stage, which allows us to make PL maps and the other is a continuous He/N<sub>2</sub> flow cryostat for low temperature PL measurements, with an uncoded piezo driven stage making PL maps much more difficult.

The process of PL explained in chapter 1 means, the focussed laser light is absorbed by the sample and emits light with reduced energy (at longer wavelengths). The emitted light is collected and parallelized by the same 50X objective lens which is again incident on the dichroic but, only this time the beam splitter is >90 % transparent for the emitted light and reflects 99.8 % of the laser light. Transmitted light can be observed with an optical microscope camera at the top. Using an internal flip mirror, the light is guided through a long pass filter which further suppresses the laser light. Light passes through a Galilei telescope and focussed at the center of the entrance slit in front of the spectrometer (Acton Research SpectraPro 2500i with 500mm focal length in a Czerny-Turner Geometry).

The spectrometer is equipped with two different gratings to spectrally resolve the emitted light and a mirror to image the sample (which is used in chapter 4). The two gratings are 150 gr/mm with blaze wavelength 800nm for coarse grating with a resolution of 0.2640 nm and 1200 gr/mm with blaze wavelength 500nm fine grating with a resolution of 0.029994 nm. The spectrally resolved light falls onto a Princeton Instruments Spec-10-CCD with 1340×400 pixels for a steady state

---

spectrum of the PL emission. For time resolved decay measurements, the spectrally resolved emission light is coupled into a multi mode fiber which is connected to an avalanche photo-diode (APD) (PerkinElmer, SPCM-AQR-14-FC 12858), where single photons are counted. For spectral studies, Winspec software is used to provide command and get the return from the CCD and spectrometer. Nanoharp from picoquant is used for reading the signal from the APD.

**Part II**

**Optical spectroscopy of Silicon  
nanoparticles**

# Chapter 3

## Spectral and temporal photoluminescence of ensemble silicon nano-particles in the vicinity of metal films

### 3.1 Motivation

Silicon is one of the most abundant elements present on earth. Due to its semiconducting nature with a bandgap of  $\approx 1$  eV, it has profound use in the field of electronics. Almost, all of the electronic devices present in today's world are silicon based, hence the name "silicon valley" was coined for the place with tech companies in California USA. Quantum dots (QDs) have enormous potential to be realised in the computation sector [Grover97, Bennett00, Meier03], but, after the discovery of II-VI QDs, [Brus84] such as CdS, CdSe, etc. researchers turned their attention towards light emitting devices as well [Schlamp97, Manders15]. One excellent example is the use of CdSe in the QD television for better color contrast used by the manufacturer Samsung and others (e.g Sony). QDs such as CdSe show excellent ensemble and single particle quantum efficiency making them front-runners for light emitting devices barring the toxic nature of Cadmium. Silicon albeit has poor quantum efficiency and indirect bandgap nature in bulk, [Royo17] if improved, can be an excellent candidate for optoelectronic devices as most semiconductor devices in use are silicon based. Currently, there is a growing interest in manipulating silicon to be an excellent light emitter. [Yao15] There are several ways reported by which, luminescence properties of silicon can be improved, for example, introduction of certain defects can facilitate radiative recombination, [Murata11, Min96] most important idea was to exploit the quantum confinement effect as silicon becomes a quantum single emitter with improved quantum efficiency. [Royo17] This was first observed in porous silicon fabricated via etching of silicon wafers. It was found that, as the etching time was increased, pores were getting bigger resulting in smaller quantum dots with improved luminescence showing size dependent optical emission properties. [Pellegrini95, Delerue93] Decrease in excited state lifetime was also observed as the size of the quantum dots were decreased. The plausible reasons are still under debate on whether or not we see a direct transition for smaller quantum dots. It was predicted by that, silicon quantum dots with bandgap greater than 2.5 eV could yield the possibility of direct optical transitions. [Royo17] The smaller the size gets, there is a significant increase in the surface to volume ratio, which means, at smaller scale regimes surface phenomena/passivation will have massive influence on the optical properties of these silicon nano-particles. [Ledoux01, Eyre08]

## 3.2. BAND STRUCTURE

---

The dangling bonds on the surface create deep level states which could potentially result in a non-radiative decay or shift the emission to lower energies. [Wolkin98] It has been observed that partial oxygen termination for smaller SiNP results in a red shift in the emission until about a certain size. More exposure to oxygen can lead to oxidation of the core silicon atoms thus resulting in reduced core size and thereafter a blue shift in the emission of the SiNP. [Eyre08] Surface passivation also influences the temperature-dependent luminescence properties of these SiNP where Suemoto et al found that for oxygen terminated SiNP, maximum luminescence was found at around 70K. [Suemoto94, Lüttjohann07] Daniel Braam in their thesis reproduced the same result for oxygen terminated SiNP and found that for fluorine terminated SiNP forming fluorinated shell, which have been studied as a part of this thesis, maximum luminescence was observed to be closer to room temperature as fluorine-silicon (F-Si) bond is stronger than O-Si or H-Si, hence it can also prevent oxidation and its excellent room temperature luminescence is worth considering for semiconductor devices. [Braam16, Lüttjohann07] Fluorinated SiNP with maximum luminescence still have longer excited state lifetime and SiNP or any fluorophore as a matter of fact, with the correct metal film in the vicinity can have increased radiative rate and reduced PL excited state lifetime. Influence of metal films such as Ag and Au on SiNP are discussed in detail through PL spectroscopy.

### 3.2 Band structure

Silicon forms a diamond like crystal structure (Figure 3.1) with one silicon atom is bonded to four other silicon atoms in an  $sp^3$  hybridization forming a tetrahedron structure with a lattice constant of  $a \approx 0.357$  nm.

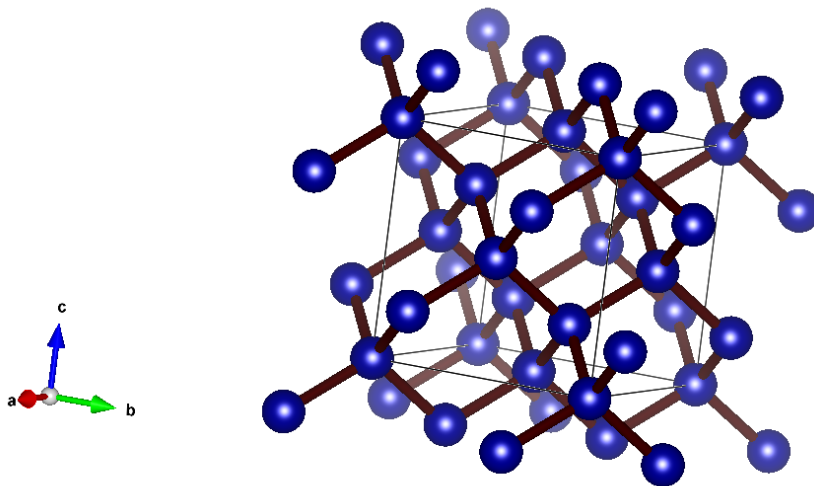


Figure 3.1: Crystal lattice structure of silicon, blue circles correspond to silicon atoms. Graphics were drawn using the software VESTA. [Momma11]

As a result of the crystal packing in silicon crystal, silicon has an indirect bandgap with valence band maximum at the  $\Gamma$  point in momentum space (k-space) and conduction band minimum lies  $(0.82 \cdot 2 \cdot \pi/a) \cdot [001]$  in between  $\Gamma$  and X point in the k-space with a 6-fold symmetry.

Due to the indirect bandgap nature, transitions of charge carriers between valence band maximum and conduction band minimum is less probable. A direct optical excitation of an electron

from the valence band to the conduction band is highly improbable and requires very high energy for a direct excitation. Hence, a single excitation process involves an optical excitation via photon with negligible momentum and requires a transfer of momentum from the phonons. Relaxation of the excited electrons works similarly, hence the quantum efficiency in silicon is low.

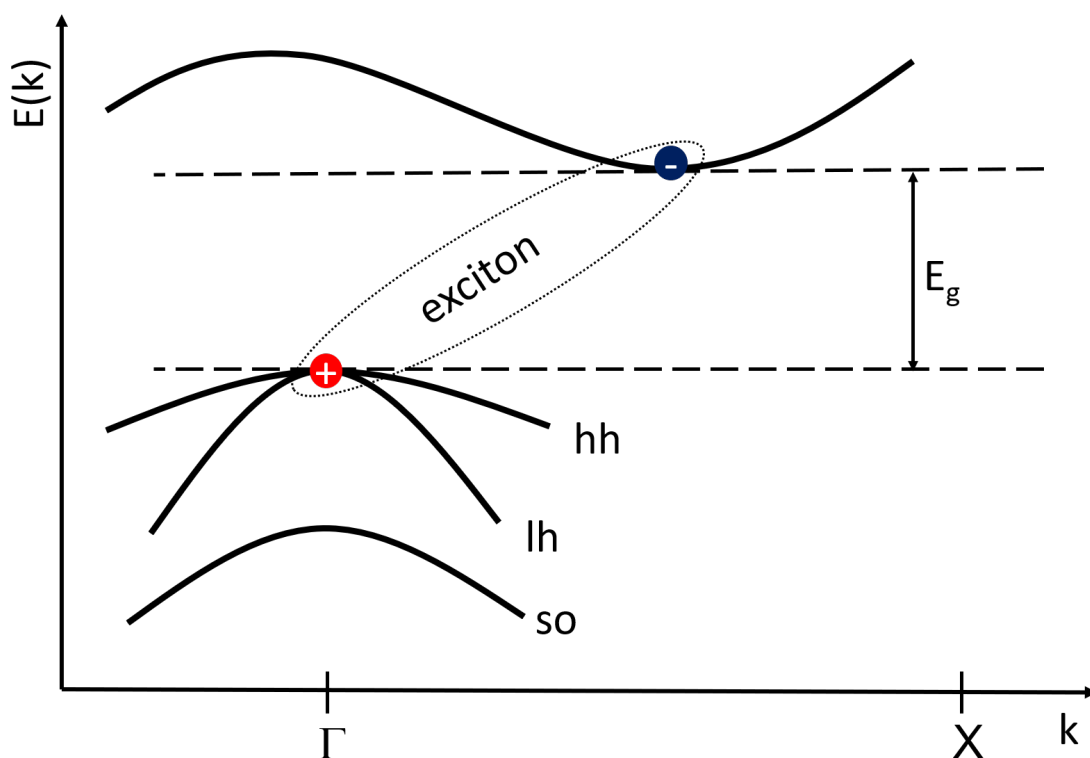


Figure 3.2: Bandstructure model of bulk silicon with an indirect bandgap ( $E_g$ ). hh, lh and so corresponds to heavy hole, light hole and split off bands respectively in the valence band. Red circle and blue circles are hole in the valence band and electron in the conduction band forming an exciton.

### 3.3 Sample synthesis and fabrication

The silicon nanoparticles used in this study were synthesized in the group of Prof. Kortshagen from University of Minnesota, USA, via gas phase large scale synthetic procedure and are capped with fluorine forming the fluorinated shell of the nano-particles. [Mangolini05] This gas phase synthesis method is time effective as it takes just a few milliseconds for the nano-particle formation and has a better yield than liquid phase synthetic method. [Mangolini05] Silane ( $\text{SiH}_4$ ) gas was used as a precursor.  $\text{SiH}_4/\text{He}$  (5%/95%) along with argon (Ar) gas was injected into the quartz tube with a certain pressure that can be controlled. Along the quartz tube, radio frequency (RF) power of 100W at 27.12 MHz is applied through a matching network to two copper electrodes producing a magnetic field which inductively couples to the precursor flowing through the quartz chamber. Precursors get dissociated into gaseous ions and hot electrons, which in turn collides with the precursor forming Si and H. With adequate temperature for nucleation and growth, crystalline nano-particles of silicon are formed. The excess negative charges form a negative shell around the

### 3.3. SAMPLE SYNTHESIS AND FABRICATION

---

nano-particles and thus preventing agglomeration. For fluorine termination of the nano-particles,  $\text{SF}_6$  was added right after silane. [Liptak12, Liptak08]

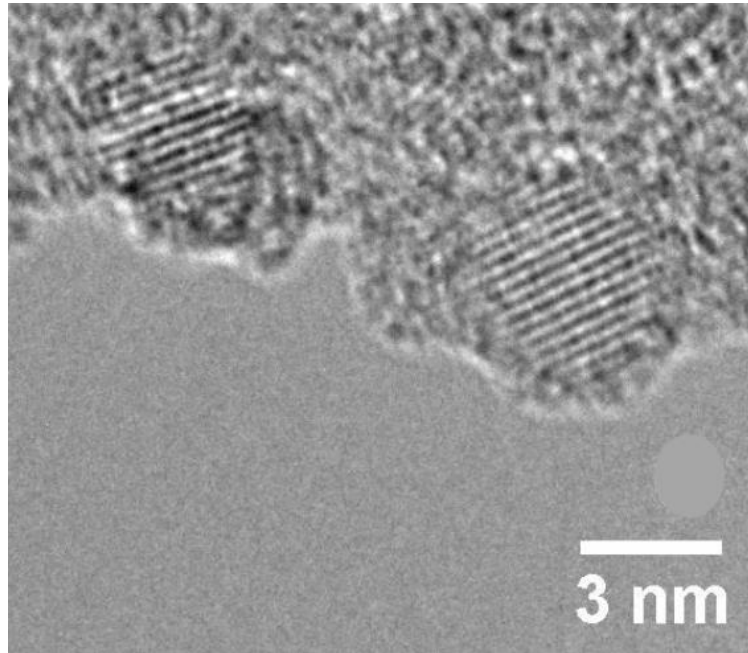


Figure 3.3: TEM image of fluorine passivated SiNP showing  $\{111\}$  lattice fringes. [Liptak08]

Figure 3.3 shows the transmission electron microscope (TEM) image of the synthesized nanoparticles, the size of a single nanoparticle were observed to be around 3 nm.  $\{111\}$  lattice fringes of the SiNP can also be seen via TEM. Silicon and fluorine form a strong bond with bond energies greater than that of oxygen or hydrogen, hence efficient passivation can be expected. Nano-particles are then collected on a steel grid that is kept at room temperature and thus preventing further nucleation and agglomeration.

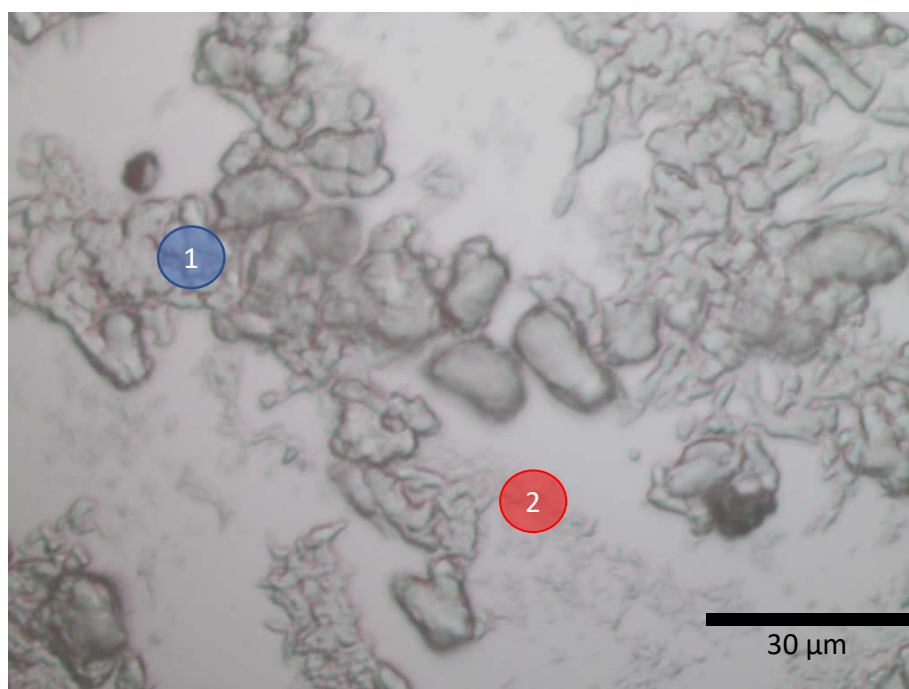


Figure 3.4: Optical microscope image of SiNP on Si/SiO<sub>2</sub> substrate with spot 1 enclosing large agglomerate and spot 2 enclosing small agglomerate of SiNP ensemble.

These fluorine capped SiNP are not solvable in most known solvents and dissolves partially in halogen containing solvents such as chloroform (CHCl<sub>3</sub>) or carbon tetrachloride (CCl<sub>4</sub>). This makes it difficult to control the amount of nano-particles that would be desired for the fabrication of SiNP on a substrate. For fabricating SiNP on solid substrates, simple drop cast technique was used rather than spin coating for ensemble measurements, this is to minimise the loss of nano-particles whilst fabricating as insolubility of SiNP does not guarantee homogeneity and hence, this rather aids in qualitative studies than quantitative. For the initial PL characterization of SiNP, SiNP dissolved in CHCl<sub>3</sub> was drop cast on Si/SiO<sub>2</sub> substrate. Figure 3.4 is an optical image of such drop cast SiNP, agglomerations of SiNP are seen. Spot 1, in the blue circle is a typical example of bigger agglomerate where, any influence from the substrate is expected to be at minimum. Spot 2 enclosed in red is a typical example of a smaller agglomerate, where, influence of the substrate is expected to be more than that of spot 1. For the spectroscopy in the vicinity of metal films, silver and gold were used. Both were thermally evaporated onto the Si/SiO<sub>2</sub> substrate and SiNP were drop cast on top of the metal surface.

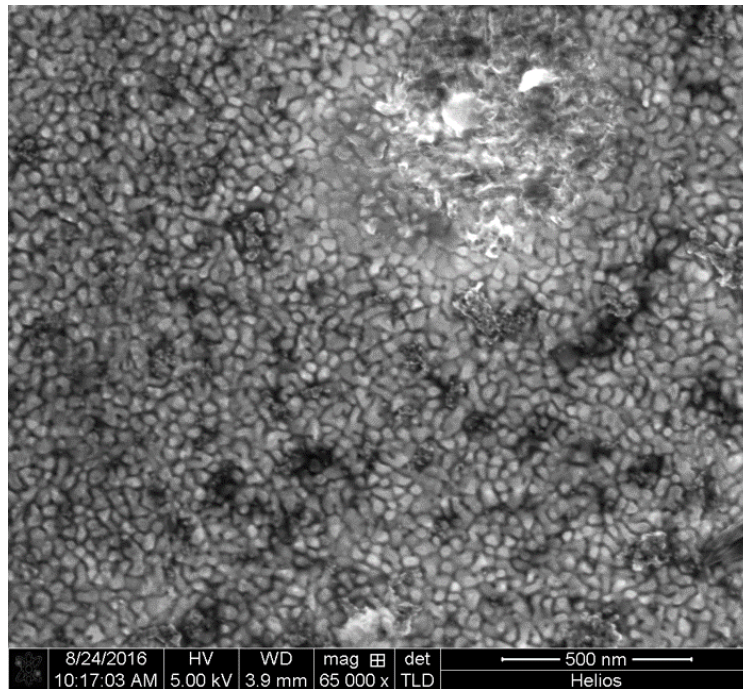


Figure 3.5: Scanning electron microscope image of gold metal film evaporated on Si/SiO<sub>2</sub> substrate. Image taken together with G. Prinz.

The evaporated metal surface, on a closer look via a scanning electron microscope (SEM), showed the rough surface of gold which can act as nano-antennae like structure with different sizes. Field enhancement from nano-antennae is already known and used for surface enhanced fluorescence. [Zhou12] Figure 3.5 is an SEM image of evaporated gold on Si/SiO<sub>2</sub> substrate. From this image, nano-antennae like structure from few nano-meters to tens of nano-meters of size can be seen.

### 3.4 Surfaced enhanced PL spectroscopy

Fluorescence or photoluminescence, as explained in Chapter 1 is the phenomenon describing light emission from a system that was excited to a higher energy state by the incident light (excitation). The excitation and emission process is highly sensitive to the environment for nano-particles, hence, the fluorophore or SiNP in our case, when subjected to a certain environment, their PL properties can be altered. Results of SiNP in the vicinity of metal films are discussed in detail in the forthcoming sections. How does the surface enhanced PL (or surface enhanced fluorescence (SEF)) work? The answer to this question is still under debate. The short explanation in this section is one that is accepted in the scientific community so far.

The use of highly reflective metal films or cavities affect both emission and excitation properties of the system under study. The effect on the excitation process is a straight forward and seemingly obvious one. Excitation intensity or flux of photon ( $I_{exc}$ ) hitting the system resulting in excitation should be increased due to the back reflection of the excitation light by the metal surface. Fort et al, have comprehensively described this in their review article about SEF. [Fort07]

$$MDE = \Gamma_{exc}(r) * Q * MCE(r) \quad (3.1)$$

Enhancement in the PL can be quantified through a quantity called molecular detection efficiency (MDE). [Fort07] MDE depends, as shown in the equation 3.1, on the excitation rate ( $\Gamma_{exc}$ ), quantum yield (Q) and molecular collection efficiency (MCE) of the system which is at a distance "r" from a particular influencing environment, which in this case, is a metal surface. Besides, increasing the excitation rate, enhancement also can occur due to increased detection of the emission. One way is to back reflect the emission using the surface with low refractive index or high reflectivity. In case of metals such as Au and Ag, all the mentioned processes are likely to occur and therefore could enhance the effective detection or collection of the emitted photons. The change in the radiative and non-radiative rates at the optimal condition reduces the effective time constant ( $\tau_{eff}$ ).

$$\tau_{eff} = \frac{1}{\Gamma_r + K_{nr}} \quad (3.2)$$

These metal films, can also increase both radiative and non-radiative rate of the emission, depending on "r" (distance between the fluorophore and the metal surface) and thereby reducing the effective time constant ( $\tau_{eff}$ ), according to the equation 3.2 where  $\Gamma_r$  is the radiative rate and  $K_{nr}$  is the non-radiative rate. When the fluorophore is directly on the metal film or when "r" is zero, it most likely will result in a quenching of the PL due to electron transfer between the fluorophore and the metal.

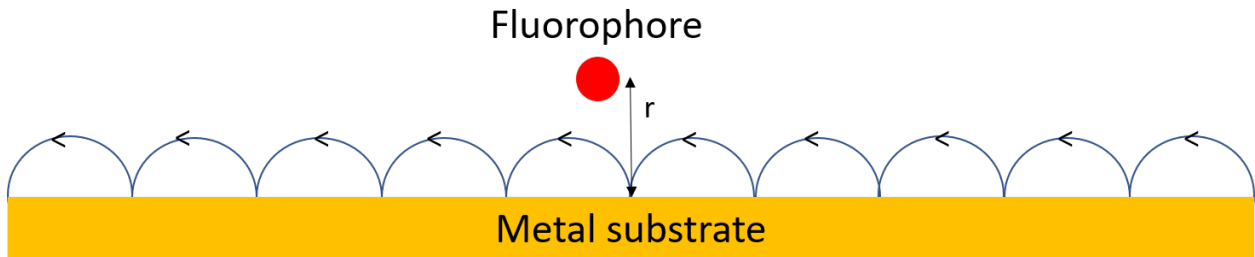


Figure 3.6: A model showing SEF requisites and half circles on top the metal showing the propagation of surface plasmon polaritons (SPPs).

As portrayed in the figure above (3.6), SEF is highly sensitive to the distance between the fluorophore and the metal surface. If the fluorophore is closer to the metal surface, that is, if  $r$  is less than 10 nm, quenching of the PL is observed [Zheng19, Biteen05], mainly due to facilitation of non-radiative pathways and rate ( $K_{nr}$ ), which also results in a decrease in  $\tau_{eff}$ . Above a certain  $r$  (10 nm is the optimal as reported by Biteen et al [Biteen05]), the interaction between the metal and the fluorophore is weak and only at the optimal distance, maximum enhancement is achieved, the interaction between them is expected to be the field enhancement which results in larger transitional dipole moment. To conclude this section, a suitable metal substrate for a fluorophore and spacer in between them is a necessity in order to achieve surface enhanced fluorescence. In

case of ensemble PL measurements for SiNP, SiNP itself can be a spacer and for single dot PL measurements, embedding SiNP in a PMMA matrix would provide the necessary spacing and by chance (statistically expected) few single SiNP would be found at the right distance from the metal. Although, controlled fabrication of such is extremely difficult.

## 3.5 Results and discussion

### 3.5.1 Steady-state and temporal PL properties of ensemble SiNP

Figure 3.7 show the steady state PL spectrum of ensemble SiNP at room temperature deposited on Si/SiO<sub>2</sub> substrate. PL shows a maximum emission around 660nm or 1.87eV through which the mean size of the nanoparticle can be calculated (see equation 3.3). [Ledoux00]

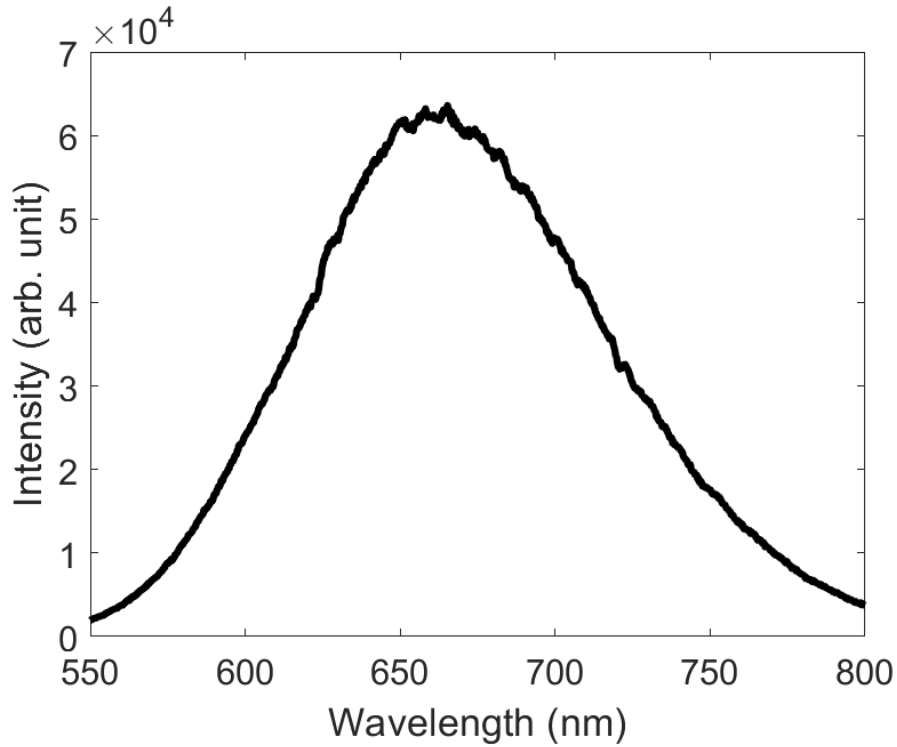


Figure 3.7: PL spectrum from ensemble SiNP on Si/SiO<sub>2</sub> substrate at room temperature

$$E_{em}(d) = E_{gap} + \frac{3.73eV}{d^{1.39}} \quad (3.3)$$

The PL of the ensembles show broad luminescence with the full width at half maximum (FWHM) of about 120nm, indicating the inhomogeneity in the size distribution ((2-5) nm) with the mean value close to 3 nm which corresponds to the measured size via TEM (see Figure 3.3) of the synthesized nanoparticles. Ensemble PL from both small (spot 2) and large (spot 1) agglomerates were similar in profile but, PL from spot 1 had more counts as the number of SiNP is more in a larger agglomerate.

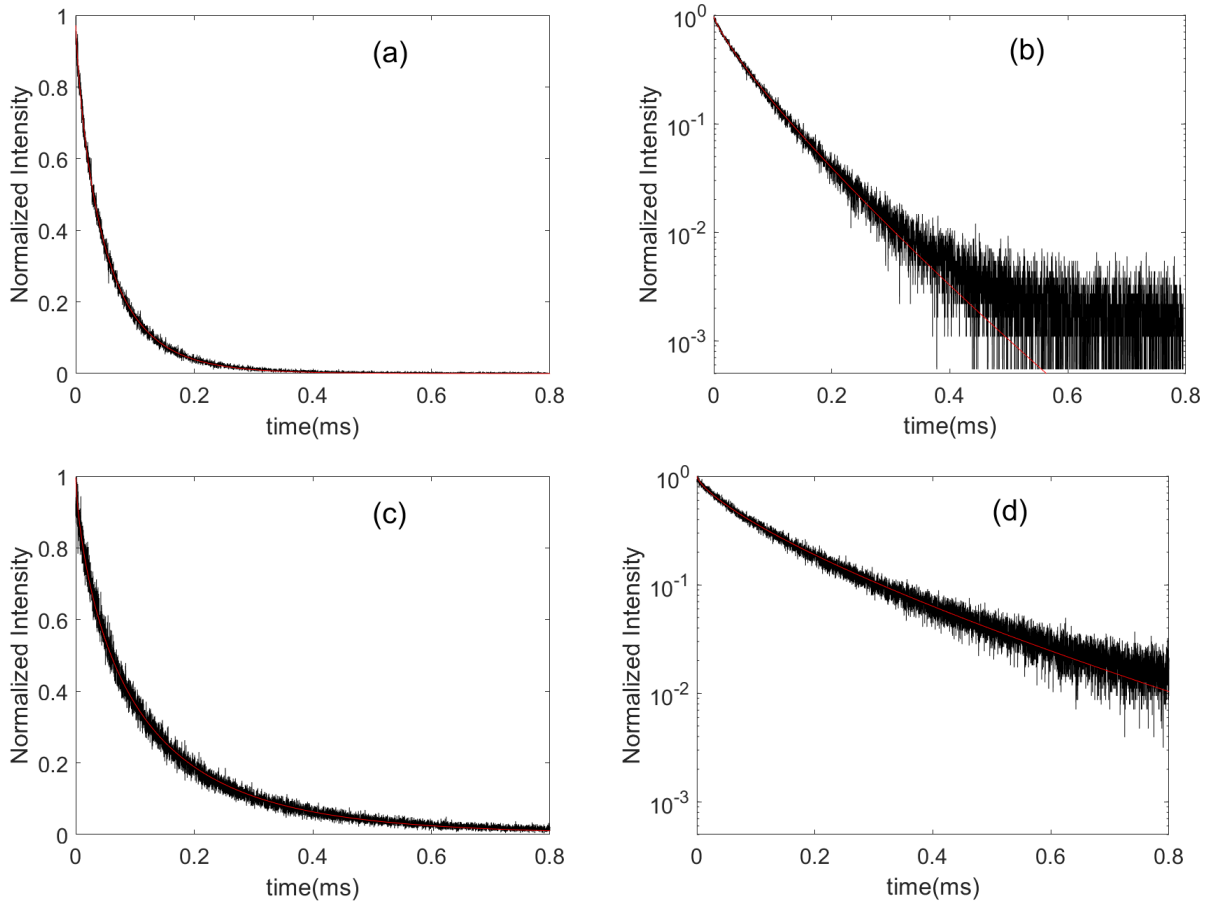


Figure 3.8: Time resolved PL decay of (a) SiNP from spot 2, (b) logarithmic plot of (a), (c) SiNP from spot 1 and (d) logarithmic plot of (c)

Figure 3.8a and 3.8c show a PL decay curve from a small and large agglomerate respectively. Figure 3.8b and 3.8d are the respective PL decay with the y-axis in logarithmic scale. Both curves were fitted with stretched exponential fit function (see equation 3.4) where  $\tau_0$  and  $\beta$  are the time constant and stretching exponent respectively. The effective time constant ( $\tau_{eff}$ ) from the fit was calculated using equation 3.5, where  $\Gamma(\beta^{-1})$  is the Gamma integral of inverse of the stretching exponent. [Zatryb11]

$$I(t) = I_0 \cdot e^{\left(\frac{-t}{\tau_0}\right)^\beta} \quad (3.4)$$

$$\tau_{eff} = \frac{\tau_0}{\beta} \cdot \Gamma\left(\frac{1}{\beta}\right) \quad (3.5)$$

The calculated effective time constant ( $\tau_{eff}$ ) was found to be  $54 \mu s$  from small agglomerate and  $122 \mu s$  from large agglomerate. Now, remember both the decay profiles are from SiNP on Si/SiO<sub>2</sub> substrate. The reason for a decrease in the  $\tau_{eff}$  from small agglomerate is still not clear. It is a well

### 3.5. RESULTS AND DISCUSSION

known fact that PL is extremely sensitive to the environment and besides the total counts,  $\tau_{eff}$  is also sensitive to the environment.  $\tau_{eff}$  is dependent on both radiative rate ( $\Gamma_r$ ) and non-radiative rate ( $K_{nr}$ ) as shown in equation 3.2. From Figure 3.8b and 3.8d, it is clear that there is faster decaying process from small agglomerate and it is rather slow from the larger agglomerate. Since, in the large agglomerate, there is less influence of the substrate and as we do not expect any sort of enhancing ability from the Si/SiO<sub>2</sub> substrate, we attribute this reduction in the  $\tau_{eff}$  for small agglomerates to an increase in the non-radiative decay rate of the PL from SiNP.

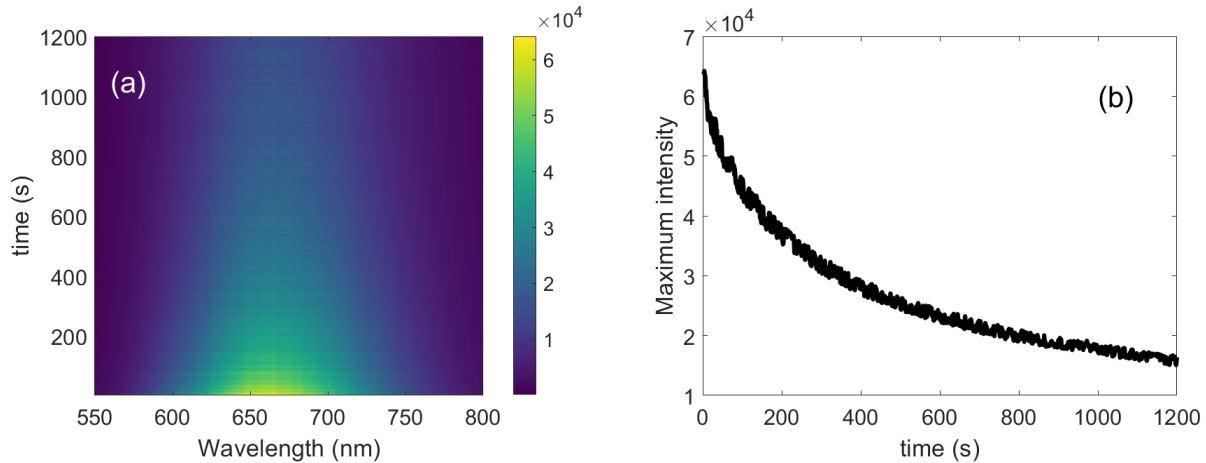


Figure 3.9: (a) Time evolution of PL spectra from ensemble SiNP at 100  $\mu$ W excitation power for 1200s. (b) Time trace of PL maximum intensity at 660nm.

Conventional quantum dots (QDs) such as CdSe, CdS, etc. are fantastically robust to light exposure when compared to organic and inorganic dye molecules which gets depleted/bleached when exposed to light. In case of the convention quantum dots, they rather get oxidized and has an altered emission (blueing [vanSark02]) or surface traps could facilitate non-radiative processes, [vanSark01] but, they show little bleaching. This is one of the major advantage of QDs over dyes for light harvesting applications. SiNPs are expected to behave similar to that of conventional QDs, but, to our surprise, with continuous exposure to light results in a decrease in the PL efficiency, in other words, they do bleach. Figure 3.9a is the color-map showing the evolution of PL spectra from ensemble SiNP over 1200s at continuous excitation with 532nm laser at the power 100  $\mu$ W, it can very well be seen that the intensity of the PL emission goes down with prolonged exposure. This trend is clearly observed in Figure 3.9b which show the maximum intensity at 660 nm dropping as the SiNPs are exposed for more time to the excitation light.

#### 3.5.2 Steady-state PL properties of ensemble SiNP on different substrates

In this sub-section and the subsequent sub-section, steady-state and time resolved or temporal PL measurements are shown, along with Si/SiO<sub>2</sub> substrate, an additional layer of either gold or silver has also been used as a substrate. Figure 3.10 shows the PL spectra of SiNP on three different substrates, on Ag, Au and Si/SiO<sub>2</sub>. The peak positions are quite similar from the particles on bare Si/SiO<sub>2</sub> and on silver (Ag) centered at 660nm, with little blue shift of less than 5nm on gold (Au). The main objective here is to try and observe similarities and differences in the PL spectra from SiNP on different substrates. As discussed in section 3.4, it is quite possible to observe an

enhancement in PL emission, provided, the choice the metal used is rather suitable for the PL enhancement of the fluorophore of interest. But, as mentioned in section 3.3, the amount of nano-particles deposited on different substrates can not be controlled and hence normalized spectra are shown.

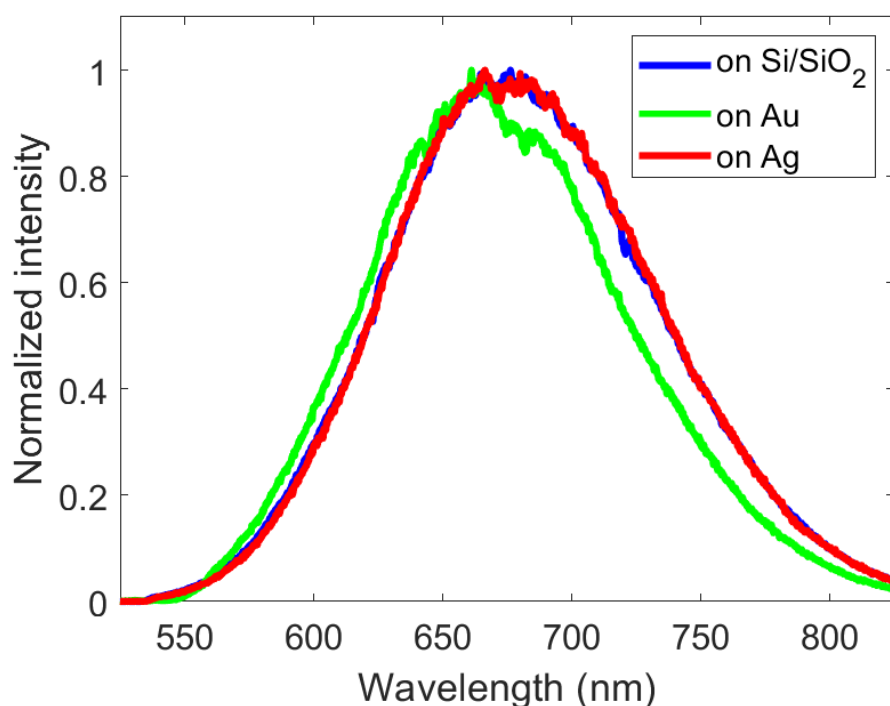


Figure 3.10: Ensemble PL spectra of SiNP on Ag, Au and Si/SiO<sub>2</sub>

Benami et al, in 2012, quantified the enhancement of PL from silicon quantum dots grown via ion implantation fixed in a matrix, in the vicinity of Ag nanoparticles grown via ion implantation. They report that this enhancement of PL by the metal nanoparticles is extremely distance dependent, at higher doses (very short distance between SiNP and Ag nanoparticles) quenching of PL occurs. [Benami12] Biteen et al, used Ag nanoparticles with a variety of diameters, i.e., with different plasmon resonance frequency, were able to selectively increase the PL of SiNP. [Biteen06] These are some of the reports about surface enhanced PL spectroscopy on silicon nano-particles. In our case with SiNP, from the steady state PL, it is most definitely difficult to do such quantitative experiments, because, as mentioned in section 3.3, these SiNP does not dissolve in most solvents and that makes it difficult to have control over the concentration of SiNP deposited on a substrate which influences the PL intensity just by different amounts more than the enhancement might change.

### 3.5.3 Time resolved PL properties of ensemble SiNP on different substrates

Steady state PL could not quite quantify a parameter that would describe any influence of the metal films on SiNP because there was not any control over concentration. To better understand the metal influence, we performed, beside the steady state PL, time resolved PL spectroscopy of SiNP capped with fluorine in the vicinity of metallic surfaces and show that, the effective time

### 3.5. RESULTS AND DISCUSSION

constant (see equation 3.2) of SiNP PL decrease in the presence of metallic surfaces such as Au and Ag. Figure 3.11a and 3.11b show the PL decay curve at 650nm emission of ensemble SiNP on three surfaces: bare Si/SiO<sub>2</sub>, Au and Ag rough metallic surfaces and the logarithmic plot of the time resolved PL decay respectively. Blue curve shows the decay on Si/SiO<sub>2</sub>, green curve on rough Au and red curve on rough Ag surfaces. All the decay curves were fitted with a stretched exponential decay curve (equation 3.4). Time constants obtained from the fit and calculated using equation 3.5 were 54, 37 and 30  $\mu$ s on Si/SiO<sub>2</sub>, Au and Ag respectively with  $\beta$  to be 0.8, 0.49 and 0.70.  $\beta$  gives an idea about the number and amplitude of exponential present in the decay, when  $\beta$  is unity, the curve becomes mono-exponential.

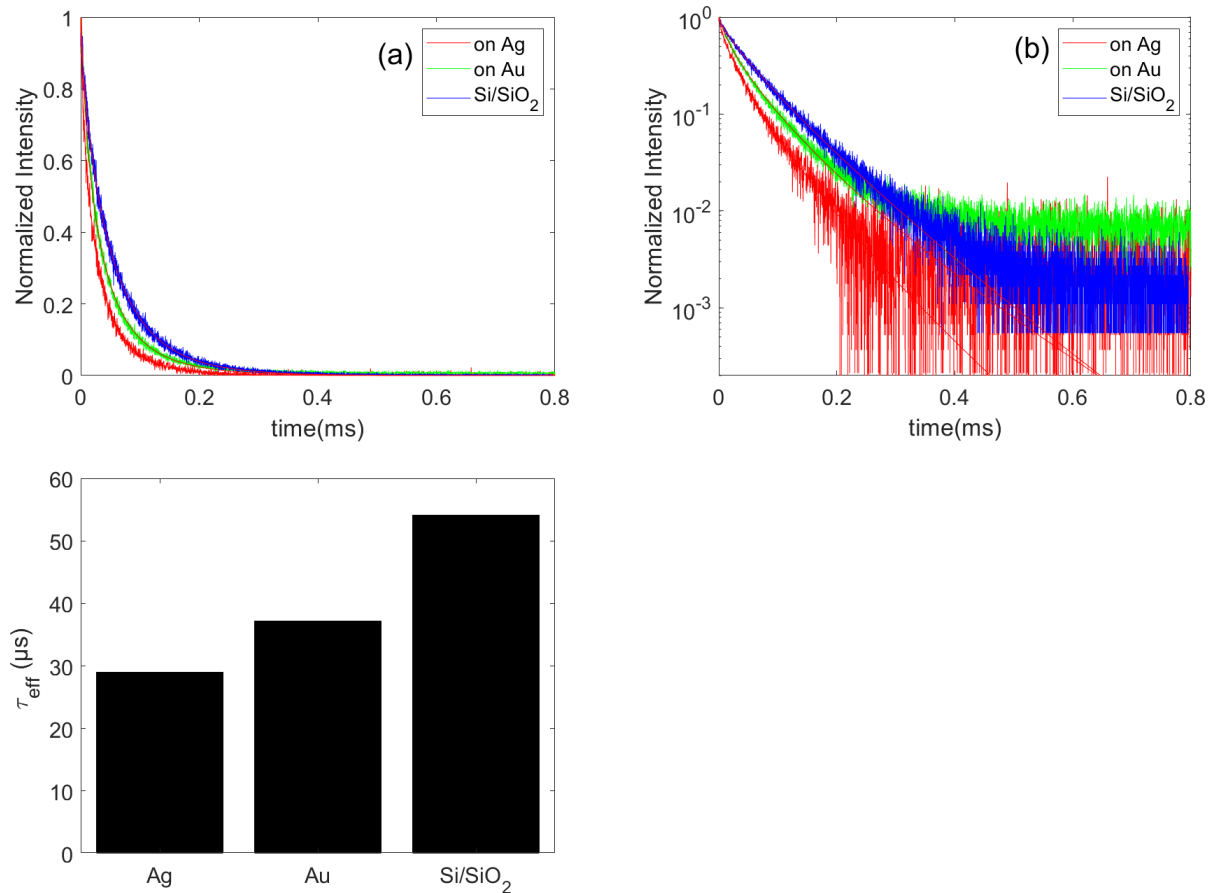


Figure 3.11: From smaller agglomerates (a) PL decay curve of SiNP on Ag, Au and Si/SiO<sub>2</sub>, (b) logarithmic plot of the decay curve and (c) Effective time constants ( $\tau_{eff}$  on three surfaces (Ag, Au and Si/SiO<sub>2</sub>))

It should be mentioned that these measurements were taken from smaller agglomerates like spot 2 as described in section 3.3, and the reason is, at spot 2 more of metal influence are likely to be observed. It is clear from the decay curve that, there is a reduction in the excited state lifetime of the charge carriers when the SiNP is in the vicinity of the metal surface compared to the bare Si/SiO<sub>2</sub> substrate. Shimizu et al also reported a reduction in the PL lifetime of one CdSe nano-particle deposited on rough Au surface. They ascribed this effect to surface enhanced fluorescence (SEF) effect. In their results, they observed a three fold reduction in the PL lifetime of

a single CdSe nanoparticle. [Shimizu02] The reduction in our case of SiNP on Au and Ag surface, were only 40%, but, we have to keep in mind that, due to our sample preparation using drop cast method, agglomerates are formed, field effect from the nano-antennae would have less impact on nanoparticles lying on top (away from the substrate). Most photons obtained from the PL of SiNP, are from the SiNP on the top surface of the ensemble, which means that these SiNP are effectively not in the vicinity of the metallic surface. The exact amount of SiNP which are surface enhanced by the interaction with the metallic surface is hard to estimate. Hence, the observed PL decay is a combination of both.

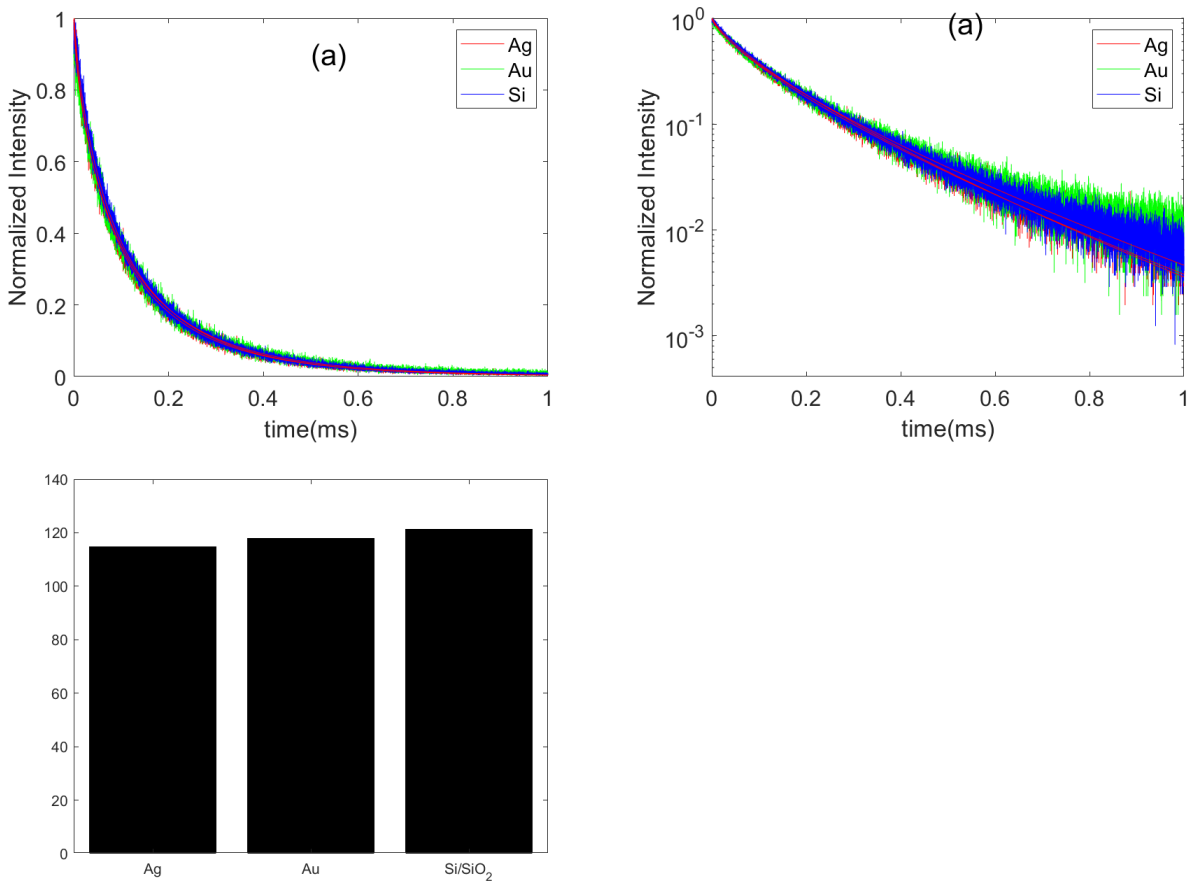


Figure 3.12: From larger agglomerate (a) PL decay curve of SiNP on Ag, Au and Si/SiO<sub>2</sub>, (b) logarithmic plot of the decay curve and (c) Effective time constants ( $\tau_{eff}$  on three surfaces (Ag, Au, and Si/SiO<sub>2</sub>))

In section 3.5.1, a decrease in the PL lifetime ( $\tau_{eff}$ ) was found between spot 1 (large agglomerate) and spot 2 (small agglomerate) from SiNP on Si/SiO<sub>2</sub> substrate. And for comparison between the different substrates from small agglomerate, 40 % decrease in  $\tau_{eff}$  was found between Ag and Si/SiO<sub>2</sub> substrate owing to an increase in the radiative rate ( $\Gamma_r$ ) in presence of Ag metal film. Figure 3.12a and 3.12b show PL decay from SiNP from a larger agglomerate on three different substrates, just like in Figure 3.11c, Figure 3.12c show the  $\tau_{eff}$  from the respective metal films. There was at the least, a 100 % increase in the  $\tau_{eff}$  observed in every case compared to the PL

### 3.6. CONCLUSION

---

decay from small agglomerates.  $\tau_{eff}$  observed were 114  $\mu$ s, 117  $\mu$ s, and 122  $\mu$ s, with  $\beta$  around 0.74 for spot 1 of SiNP on Ag, Au and Si/SiO<sub>2</sub> respectively. There is a significant change in  $\beta$  found for large agglomerate and it is approaching unity as compared to small agglomerate. A clear trend regarding the influence of metals was observed as we see a lowered  $\tau_{eff}$  value in case of Au and Ag. The radical difference in case of the large and small agglomerate is tentatively attributed to the influence of the surrounding, but, it is still not very clear.

## 3.6 Conclusion

Silicon nanoparticles with a mean diameter of 3 nm and an optical bandgap of about 1.8 eV were investigated. These SiNP were synthesised via a gas phase synthetic technique and capped with fluorine shell as silicon and fluorine form a strong bond. Steady state and temporal PL studies were undertaken to study the improvement of the light emitting property of these SiNP in the vicinity of metal films. PL lifetime of SiNP was decreased in the presence of metal films such as Au and Ag, mainly Ag, where 40 % reduction was observed when these SiNP are fairly close to the metal. Since one of the main disadvantages of silicon as the light emitter is its PL lifetime, for both light emitting application and also for studying or performing the fundamentals such as single particle spectroscopy. We have been able to reduce the  $\tau_{eff}$  by at least 40 % and for a single dot closer to a metal it is believed to be even lower. This result will be exploited in the next chapter.

# Chapter 4

## Single silicon-dot spectroscopy

### 4.1 Motivation

The work done in this chapter is an extension of the previous chapter 3. One of the main motivations behind this would be, in a philosophical sense, the realization of the differences in individual and collective behaviour. Individual fluorophores, collectively, they display certain light interaction traits and that cannot be intrapolated to predict the individual as they display different traits. Semiconducting nanoparticles, especially quantum dots are an important class of materials in the field of light emitting devices and computing devices. A single quantum dot is a single photon source and this can be exploited in the said field. Although, several issues are being dealt with these days as these single particles display characters such as PL intermittency, spectral jittering, etc. In this chapter, using the result of previous chapters, these phenomena are studied for single silicon nanoparticles with fluorine shell.

### 4.2 Sample fabrication

In preparation for performing PL measurements on single particles/dots, we first defocused the excitation laser beam to obtain a spot diameter of  $70\mu\text{m}$  (which is schematically shown in Figure 4.1). The entrance slit was opened wide, 50X objective lens with NA of 0.8 was used and the mirror instead of the grating was used to image the spectrally unresolved emission from the sample.

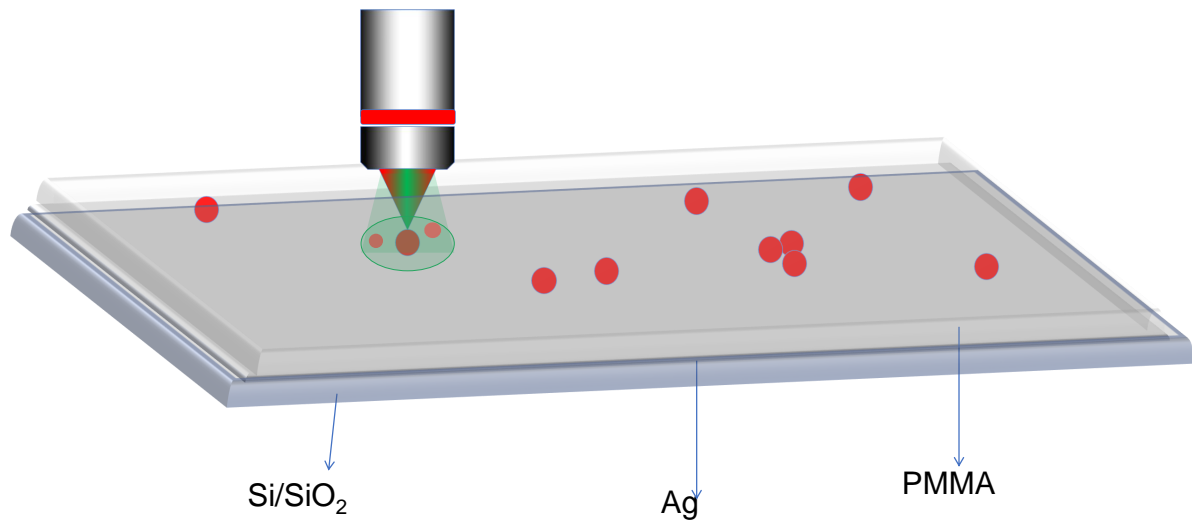


Figure 4.1: Experiment technique to identify emission from a single SiNP embedded in a PMMA matrix

Figure 4.2 is an SEM image of SiNP embedded in a PMMA matrix on Si/SiO<sub>2</sub> substrates with a gold film on top of it. The irregular structure of the PMMA matrix that can be seen in the picture is due to the interaction of PMMA with the electron beam. Enhancement or mainly the reduction in PL lifetime in the PL of SiNP is imperative to realise single particle spectroscopy, though in the previous chapter, we concluded that there is a reduction in the PL lifetime ( $\tau_{eff}$ ) in presence of Ag, for example, this does not necessarily guarantee an increase in photon counts per second. Hartsfield et al reported that smoothness of the surface of the metal layer influences the recombination rate of the emitter (CdSe quantum dot). It was observed that epitaxially grown smooth silver film, significantly reduced the excited state lifetime to a narrow distribution around 5ns, whereas with evaporated rough Ag film, though significant, broader distribution centered at 8 ns spanning from 4-12 ns were observed. One more interesting observation is the effective PL counts from the emitter were larger for the ones in the vicinity of the rough surface rather than the epitaxially grown smooth surface. [Hartsfield16]

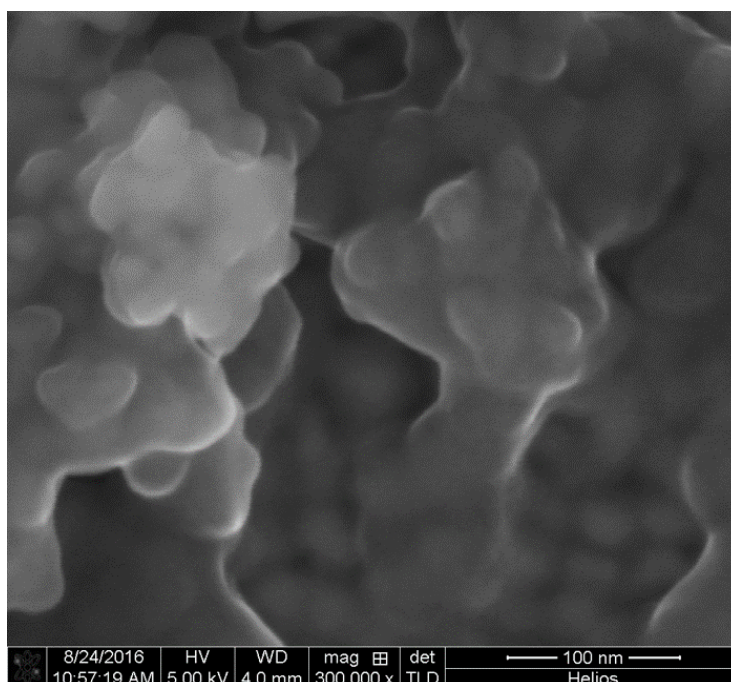


Figure 4.2: SEM image of SiNP embedded in a PMMA matrix on Au substrate. Image taken together with G. Prinz.

This is in agreement with our experimental results, as single SiNP on rough Ag surface were easily observable. To increase the roughness, Si/SiO<sub>2</sub> substrate was first coated with Au<sub>0.75</sub>Ag<sub>0.25</sub> alloy, which was then de-alloyed when treated with hot nitric acid, resulting in the porous sponge-like Au film, [Erlebacher02] thin layer of Ag was thermally evaporated on top of the porous Au film, resulting in an increased roughness of Ag film. This method was adapted from the master thesis of J. Weißbon. [Weißbon12] A dilute solution SiNP in PMMA-CHCl<sub>3</sub> was then spin-coated on top of the substrate to get a well distributed SiNP embedded in the PMMA matrix.

### 4.3 Results and discussion

Combining the excellent room temperature PL properties due to the fluorine shell and an at-least 40% reduction in PL lifetime, especially on the rough Ag surface, single silicon dot phenomena such as PL intermittency and spectral jittering were observed at room temperature for SiNP on a rough Ag surface. The method of the collection of data for PL intermittency studies is described in Figure A.1.

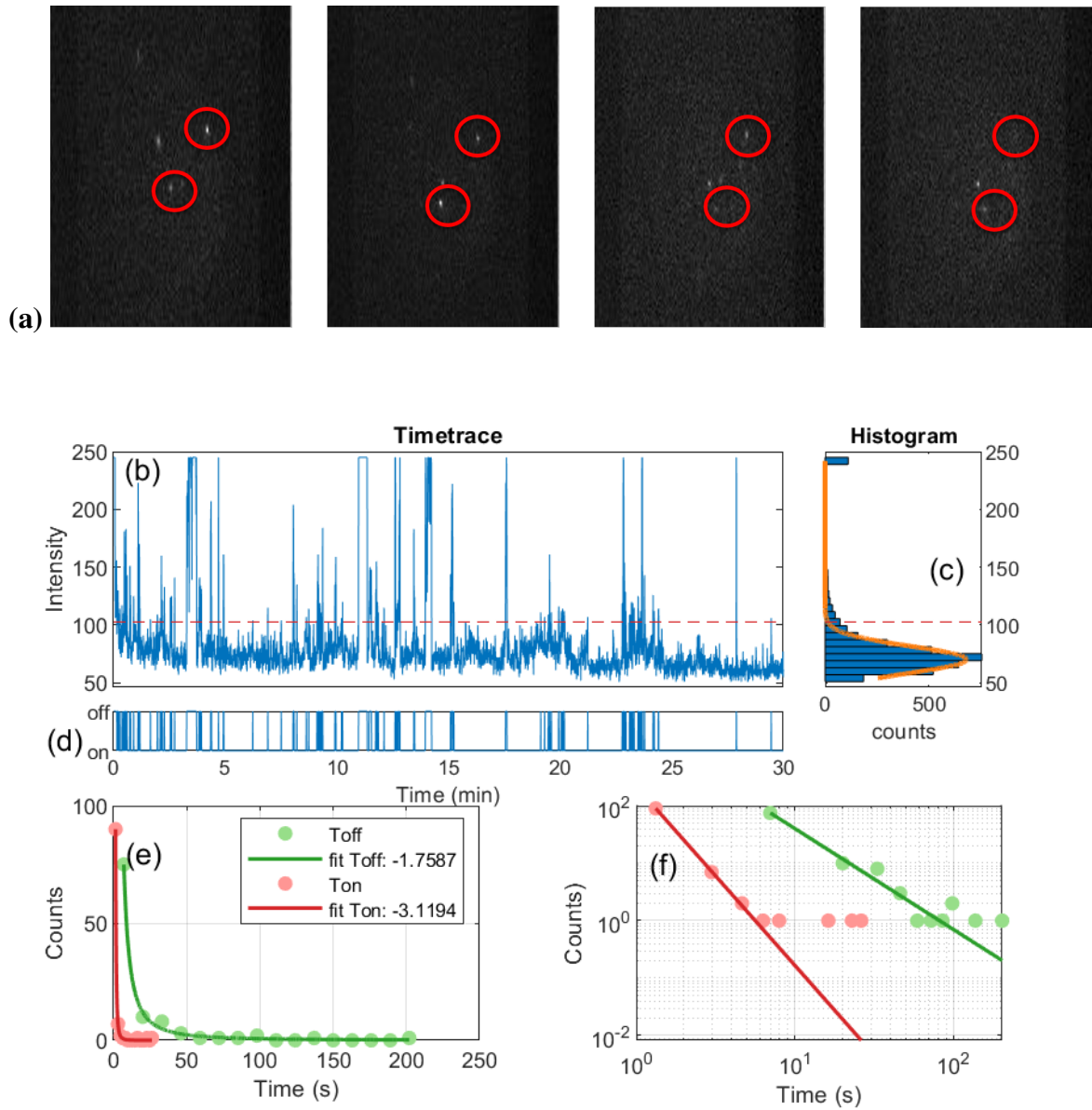


Figure 4.3: (a) Series of images at different times with bright spot corresponds to a single SiNP, (b) time trace of photon counts from one SiNP, (c) bin of intensities to identify the threshold, (d) plot showing binary on-off in the time trace, (e) power law statistics of "on" and "off" times from a single SiNP and (f) logarithmic plot of (e).

Figure 4.3a shows the time evolution of PL from single SiNP (spots enclosed in the red circles in the images). Under continuous excitation with 532nm excitation wavelength and power of  $700\mu\text{W}$  distributed over  $70\mu\text{m}$  spot size on a SiNP, we observed PL intermittency or "blinking" where the QD does not continuously emit light. Figure 4.3b shows the intensity-time trace of one of the SiNP for 30 minutes. The occurrence of particular intensity bins using Scott's normal reference rule, [SCOTT79] from the time trace (Figure 4.3b), along with double gaussian fit can be seen in Figure 4.3c. This is done in order to find a good threshold value (shown as the red dotted line in Figure 4.3b and 4.3c), above which, SiNP is in an emitting state ('on') and below which, SiNP is on a non-emitting state ('off'). Figure 4.3d, shows when SiNP is in 'on' state,

it can be seen that the SiNP is mostly in 'off' state with rare short 'on' states. This PL blinking was first observed in CdSe QDs by Nirmal et al. [Nirmal96] It became a good indication of a confirmation of single particle emissions. Four more time traces and blinking characteristics of single SiNP can be seen in the appendix (Figure A.2, A.3, A.4 and A.5). One of the reasons for the non-continuity in the emission from a single quantum dot is due to the fact that, there is a competing process called Auger recombination (schematically shown in Figure 4.4) as opposed to the radiative exciton recombination, energy from the exciton recombination is transferred to extra charge in the system. Other possible mechanisms would be otherwise called B-type blinking (names coined by Galland et al) as opposed to A-type blinking explained above. In case of B-type, the shell thickness is expected to be rather small and defects on the surface act as trap state for the excited electrons. Differences in these two types of blinking are observed in the lifetime, where, in case of A-type blinking, the reduced lifetime of trion emission is found. [Galland11] We explain the blinking of single SiNP using Efros-Rosen model (see Figure 4.4). [Efros16] In the model, QD is charge neutral during the 'on' state. In presence of an excess charge in the QD, energy from the recombination of electron-hole pair displaces the excess charge rather than emitting a photon, which is the 'off' state.

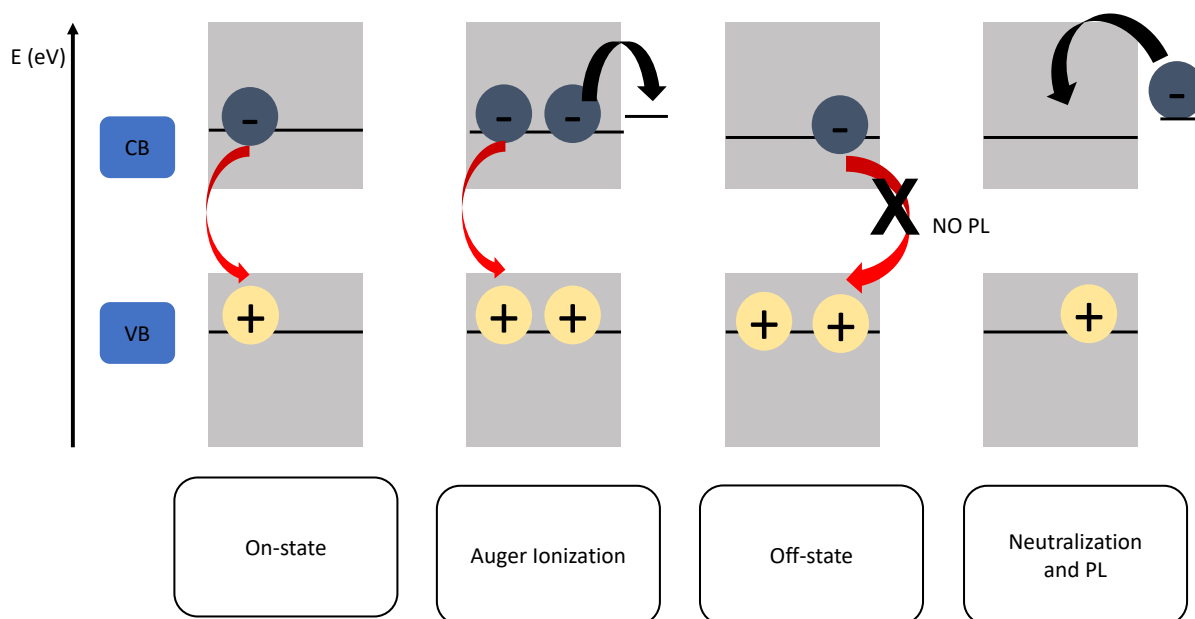


Figure 4.4: Scheme describing processes involved in PL intermittency including Auger ionization process explained using Efros-Rosen model. CB and VB are conduction band and valence band respectively.

Blinking is disadvantageous for any light-emitting application of QDs. Introduction of thick shell with wider bandgap around the core of CdSe QDs led to a drastic reduction in the frequency of short "on" and "off" times and almost no blinking particles, a gradient alloy shell, due to the gradual change in the lattice parameters, further reduced the occurrence of dangling bonds which provides the surface trap states. [Mahler08, Efros16, Ji15] Blinking of this fluorine capped SiNP might also be explained by Efros-Rosen model (see Figure 4.4) where, as a result of Auger recombination, the

### 4.3. RESULTS AND DISCUSSION

core of the quantum dot becomes charged as a result and thus the further excitonic recombination becomes non-radiative, due to an Auger-like recombination in this charged state.

$$p = A \cdot t^{-m} \quad (4.1)$$

The "on" and "off" statistics follow a power law distribution (equation 4.1). "A" in equation 4.1 is the proportionality constant and "m" is the exponent. Exponent "m" value of around -1.5 is found to be consistent with Auger recombination in conventional CdSe QDs. [Frantsuzov08, Efros97, Ye11] Here, in case of SiQDs, the value is found to be -1.8 for the "off" statistics and -2.7 for "on" statistics, but, both "on" and "off" exponent approaches -1.5 with more data. This power law statistics is mainly due to the existence of multiple trap sites and thereby multiple Auger rates. For silicon quantum dots embedded in a SiO<sub>2</sub> matrix, exponential behaviour was observed. For our system, fluorine capped SiNP, behaves more like the colloidal quantum dot which means, there is a presence of more than one trap state with non-converging on/off and off/on switching rates are observed. [Sychugov17]

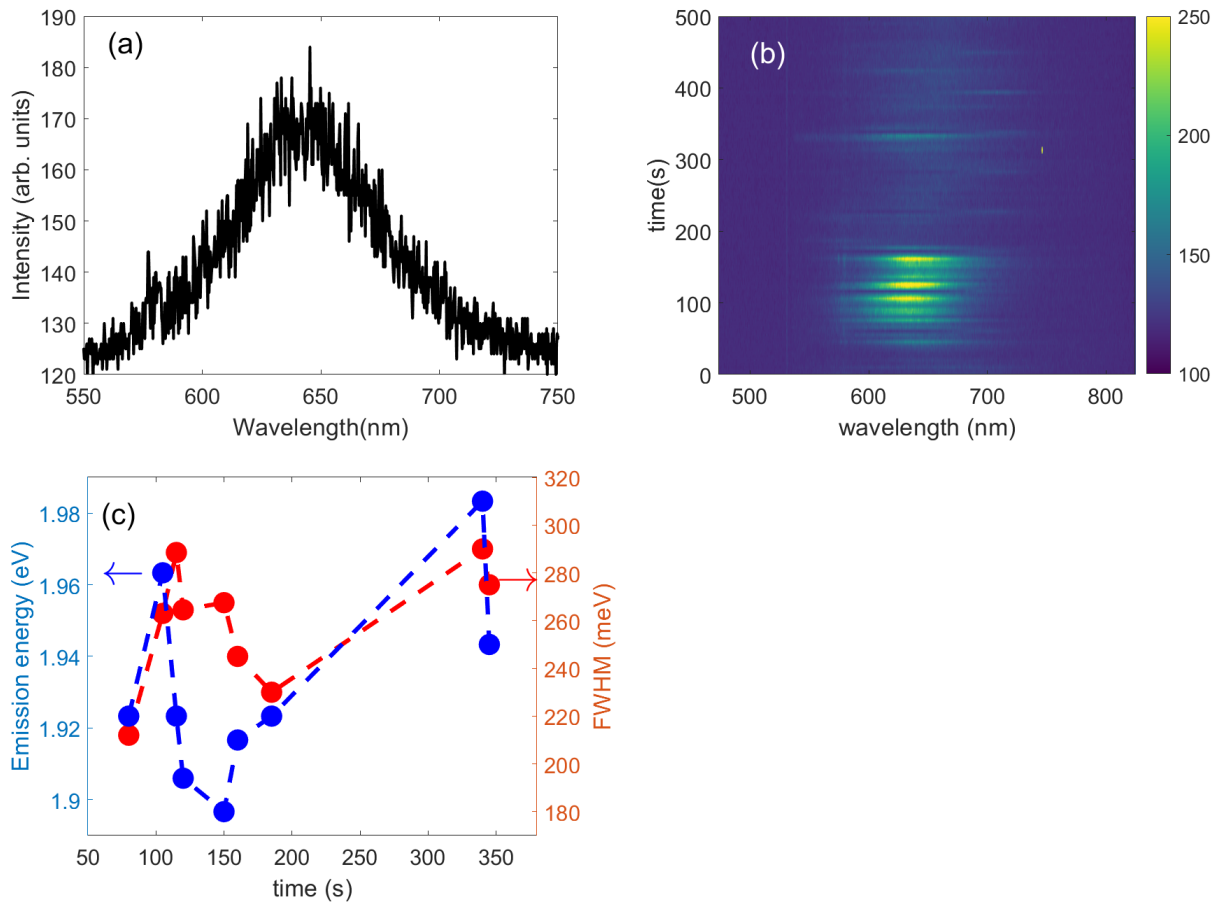


Figure 4.5: (a) PL spectrum of a single or subensemble of SiNP (b) Contour plot showing time evolution spectra from single or subensemble SiNP and (c) plot of emission energy and FWHM against time to assess the correlation between emission energy and FWHM.

The emission from the brightest blinking particle was spectrally resolved by replacing the mirror with a grating in the spectrometer at room temperature. The integration time had to be prolonged from 500ms to 5s for detecting the spectrally resolved time evolution of a single SiNP emission. Different to the spectrum from the ensemble with a peak wavelength at 660 nm with FWHM of at least 120 nm, emission from this single particle had a peak position of  $\approx 645$  nm with FWHM of  $\approx 50$  nm (Figure 4.5a). Decrease in line width is expected for single SiNP and peak position indicates that this particle is smaller than the most common particle size. Figure 4.5a shows PL spectrum from a single particle, both spectrally and temporally resolved PL spectra can be seen in Figure 4.5b. Along with blinking, jitter in the peak position between 640 nm and 650 nm was observed. This phenomenon is known as spectral jittering, which was e.g. also observed for CdSe QDs. [Neuhauser00] Spectral jittering is the result of the quantum-confined Stark effect, where electric fields tilt the bands in the QD and therefore leading to red-shifted emission. This field can be externally applied or introduced by fluctuating charges around the QD. For CdSe, Braam et al., observed an anti-correlation between emission energy and FWHM, which can be understood by the presence of additional charge in the vicinity of the QD. [Braam13] This anti-correlation up to now, have not been observed for the SiNP (see Figure 4.5c), which might be due to a different behaviour of the fluorine capped SiNPs or just due to short time traces and longer bin time. To confirm this, longer time traces are needed, which are hard to obtain due to rather longer "off" times compared to that of CdSe.

## 4.4 Conclusion

Ag film was deposited on sponge-like Au to create a rough Ag surface for better surface enhancement of SiNP. Single particle phenomena like PL intermittency was observed from single SiNP. Blinking or PL intermittency "on/off" statistics revealed a power law behaviour, meaning, multiple Auger rates due to multiple trap sites were present. PL intermittency showed more prolonged "off" times and shorter "on" times. Spectral jittering of single SiNP due to quantum confined Stark effect was observed along with the PL intermittency. The potential anti-correlation between emission energy and FWHM is not observed yet. To understand more of these single particle phenomena, longer time traces are necessary.

## **Part III**

# **WS<sub>2</sub> monolayers**

# Chapter 5

## Defect studies on WS<sub>2</sub> monolayers

### 5.1 Motivation

Tungsten disulfide is one of the prominent transition metal dichalcogenide materials, which shows intriguing optical properties if it is processed to a monolayer. Two dimensional (2D) monolayers of transition metal dichalcogenides (TMDC) have drawn much interest in the recent times due to their excellent physical properties such as indirect to direct bandgap transition (with bandgap energies mostly in visible and near infra-red region) from bulk to monolayers and are thought of as an upgrade to the components in transistors. [Splendiani10] WS<sub>2</sub> monolayers, show higher luminescence quantum yield ( $\approx 6\%$ ) when compared to other TMDC monolayers like MoS<sub>2</sub> ( $< 1\%$ ). [Yuan15] TMDC also show strong spin-orbit coupling, mobility, and exciton interactions. [Xiao12] Also the formation of quantum emitters at defects or engineered by varying strain profiles at certain locations have been shown. [He15] Although it has been over a decade since the discovery of graphene and 2D materials, practical applications of these 2D-TMDC and graphene have not lived up to the expectation. The main reason, besides the growth and fabrication, of which significant improvements have already been realized, is the defect prone nature of these materials. To realize the potential of 2D-TMDC in various applications, defects in these materials must be studied. In graphene, the intensity ratio of D and G peaks from the Raman spectroscopy is used to non-destructively characterize monolayers of graphene. There is, however, no direct correlation for TMDC to characterize defects in monolayers using Raman spectroscopy. Defect bound emissions are observed in the low temperature (LT) photoluminescence (PL) spectroscopy and this technique have proved to be a valuable non-destructive technique to characterize the defects in TMDC monolayers.

### 5.2 Sample synthesis and fabrication

Samples studied in this chapter were grown by the group of Prof. Mattevi from Imperial College London, London. WS<sub>2</sub> flakes were synthesized via chemical vapour deposition (CVD) using a hot-wall quartz tube furnace. 0.2 g of H<sub>2</sub>WO<sub>4</sub> (Sigma, 99.99%) mixed with 0.2 g of NaCl (Sigma, 99.99%) were placed in an alumina boat in the centre of the tubular furnace, whereas 0.6 g of S powder (Sigma, 99.99%) were placed in another boat in the upstream region, controlled independently with another heating module. The substrate was Si/SiO<sub>2</sub> cleaned by ultrasonication in deionized water, acetone and isopropanol and placed close to the W-containing boat in the down-

### 5.3. BANDSTRUCTURE

---

stream direction. The reactor was purged with 200 sccm of high purity argon gas for 30 minutes at 200°C, afterward the furnace was heated up till 850°C at 25°C/min in the meantime the S boat was heated up till 125°C at 5°C/min using 100 sccm of Ar. These temperatures were kept for 15 minutes and then the furnace was naturally cooled down.

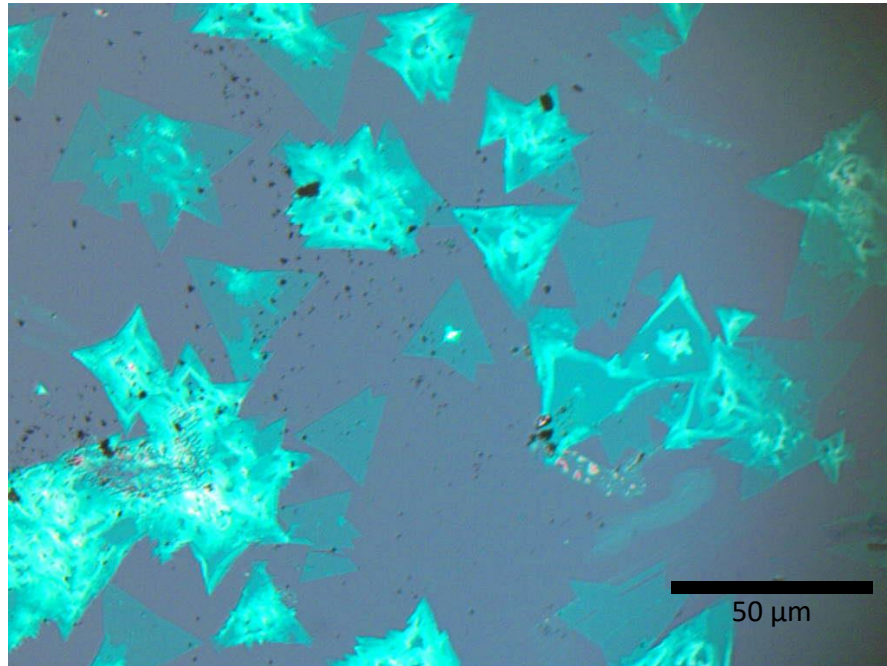


Figure 5.1: Optical micrograph of WS<sub>2</sub> flakes on Si/SiO<sub>2</sub> substrate.

### 5.3 Bandstructure

TMDCs are a class of materials with the empirical formula MX<sub>2</sub>, where M is the transition metal and X is the chalcogen. These materials form a layered structure X-M-X with two planes of X separated by M plane, which constitute a monolayer as shown in Figure ??a. These monolayers when stacked on top of each other are held by weak van der Waals attractive force, forming the bulk form of these semiconductors as shown in Figure ??b. Figure ??c shows the top view of a TMDC monolayer, the X-M-X structure forms a hexagonal lattice with three corners occupied by M atoms and three by X atoms with alternate X of top and bottom position adjacent to M atoms. One M atom is bonded to six X atoms, the overall symmetry of TMDC is hexagonal or rhombohedral, the M has octahedral symmetry (bonded to six X) or trigonal prismatic coordination. [Wang12]

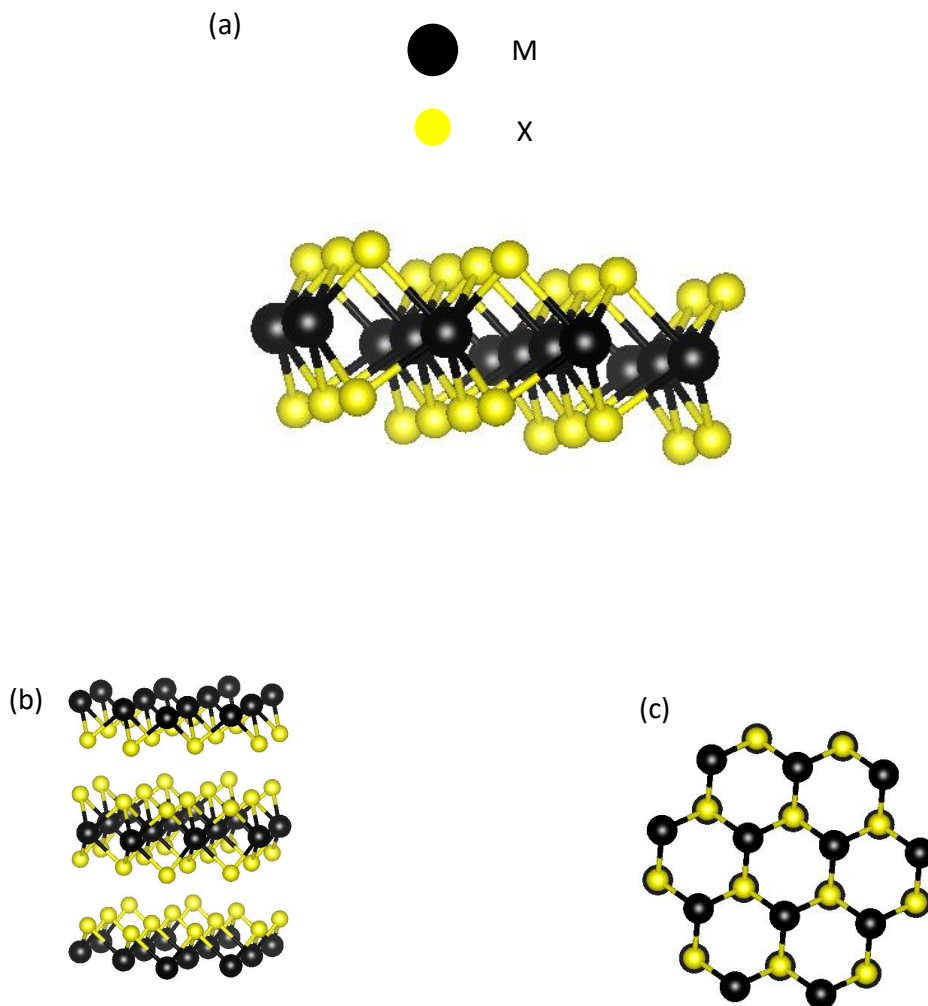


Figure 5.2b and 5.2a shows the bandstructure of  $WS_2$  in the form of multilayer and monolayer respectively. In Figure 5.2a showing bandstructure of bulk  $WS_2$  with a stacked structure, the valence band maximum is found at the  $\Gamma$ - point in the Brillouin zone and the conduction band minimum is found in between the  $\Gamma$ - point and the K- point in the Brillouin zone forming an indirect bandgap semiconductor. There is a secondary valence maximum and conduction minimum at K- point in the Brillouin zone forming a direct bandgap at K- point. [Wang12]

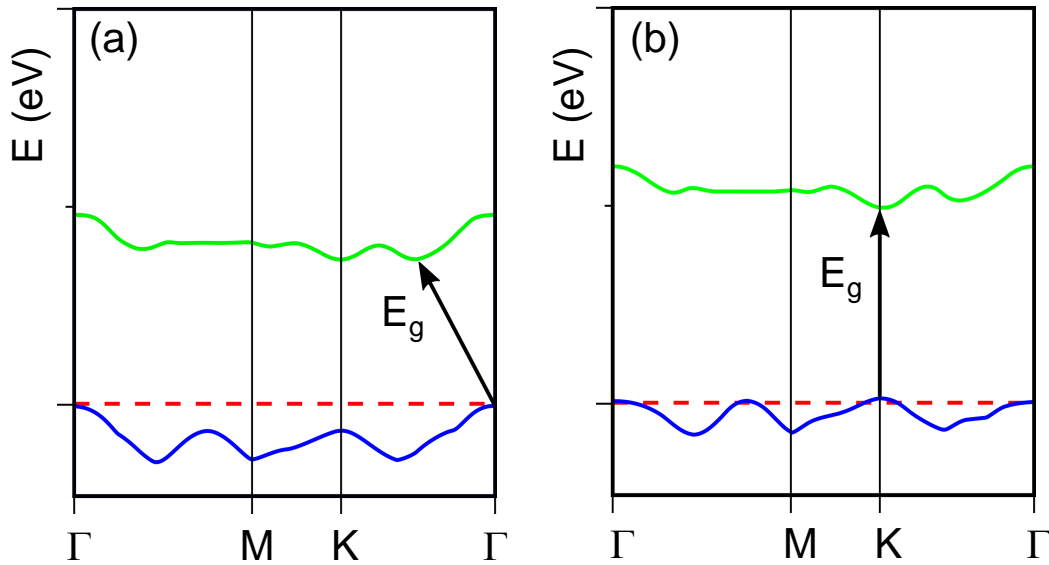


Figure 5.2: Bandstructure of  $\text{WS}_2$  showing (a) indirect bandgap at  $\Gamma$  point in the Brillouin zone in bulk and (b) direct bandgap at K point in the Brillouin zone in monolayer. Graphics taken from [Wang12]

$\text{WS}_2$  bulk, when peeled down to a monolayer, shows transitions at the direct bandgap (shown in Figure 5.2b) at K point in the Brillouin zone. This change in the bandstructure from indirect to direct bandgap, from bulk to monolayer is due to quantum confinement in the  $z$ -direction resulting in change in the hybridization between  $p_z$  orbitals on X atoms and  $d$  orbitals on M atoms. States near  $\Gamma$  point is due to the  $p_z$  orbitals on X atoms and  $d$  orbitals on M atoms and have a strong interlayer coupling, therefore, when the stacking is chopped down to one layer and as a result of quantum confinement, the valence band maximum and the conduction band minimum gets widened. States near the K point are relatively unchanged as they are mainly due to  $d$  orbitals of the M atom in the monolayer and have no interlayer coupling. [Wang12] In a monolayer, there is a new valence band maximum and conduction band minimum at the K point. Different TMDCs have different bandgap values at the K point, the system studied here is  $\text{WS}_2$  which shows a bandgap value of  $\approx 2$  eV ( $\approx 620$  nm). Only monolayers of  $\text{WS}_2$  have been studied in this chapter, more specifically, the mid-gap states due to the defects in the system were probed and studied via PL spectroscopy.

## 5.4 Results and discussion

Two batches of WS<sub>2</sub> monolayers were investigated. The synthetic protocol for the two batches was similar (see section 5.2).

### 5.4.1 WS<sub>2</sub> sample batch 1

Figure 5.3 shows the PL spectrum from an as-synthesized pristine WS<sub>2</sub> monolayer flake at room temperature (RT). PL at RT shows almost an asymmetric line peaked around 632 nm corresponding to neutral exciton recombination ( $X_0$ ) and trion ( $X^-$ ) emission. [Liu19, Wang15]

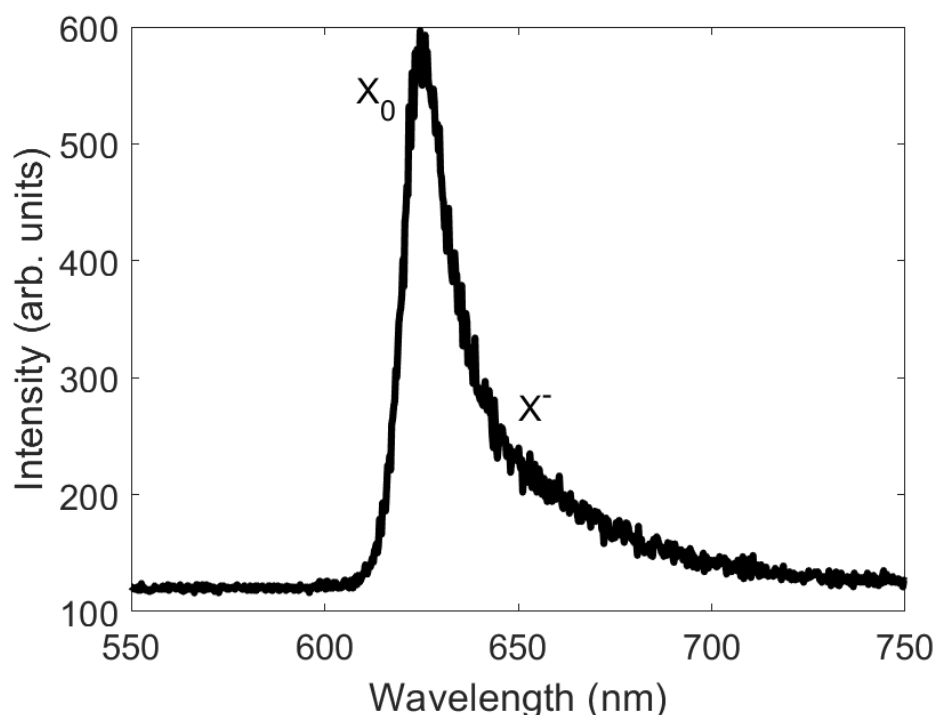


Figure 5.3: PL spectrum of monolayer WS<sub>2</sub> at RT

As mentioned in the motivation, the main objective of this chapter is to study the defects present in WS<sub>2</sub> monolayers through PL spectroscopy. RT PL does not show any optical emissions related to defects for our samples. Chow et al in their work was able to observe defect-bound exciton emission at RT by introducing defects via plasma exposure. [Chow15] Defect bound emission is expected to have slightly lower energy than the exciton emission. [He16b] The reason for the absence of such emission at RT, is either because the thermal energy at RT is enough for the charge carriers to escape from the defect trap, recombination could be non-radiative and/or this pristine flake is defect free.

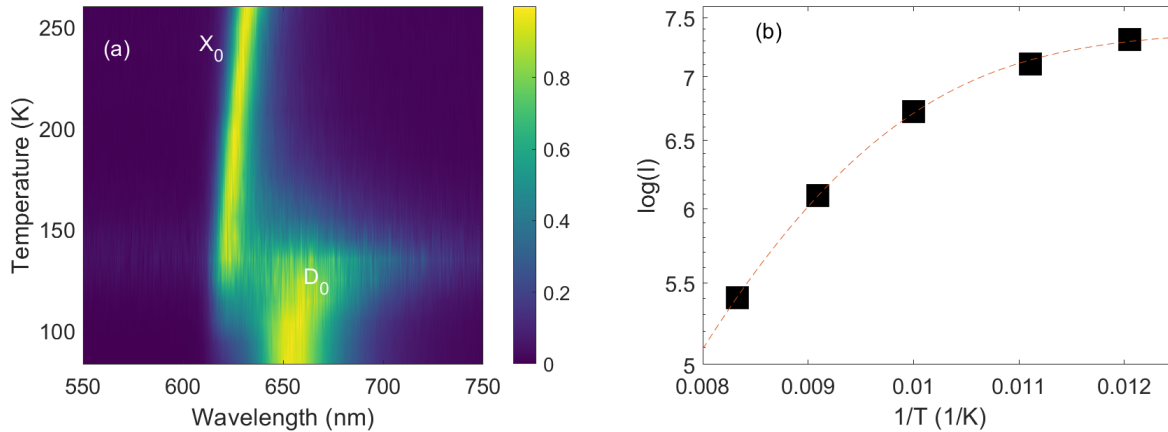


Figure 5.4: (a) PL spectrum of monolayer WS<sub>2</sub> at different temperatures at 1,5  $\mu$ W excitation power and (b) modified Arrhenius plot of the defect emission intensity over temperature.

Figure 5.4a is a contour plot of PL from a pristine monolayer of WS<sub>2</sub> at different temperatures starting from 260K at the top spectrum and cooled down to 83K at the bottom spectrum. Colorbar indicates normalized intensity. Temperature dependent PL spectra shows a blue shift in the X<sub>0</sub> emission because the bandgap widens as the temperature gets colder and this shift in the X<sub>0</sub> tends to follow the Varshni empirical formula. [Varshni67] With decreasing temperature, from 100 K and downwards, besides the X<sub>0</sub> band, an additional emission band starts to appear. This additional emission is attributed to defect-bound emission (D<sub>0</sub>). For pristine flakes, defect-bound emission (D<sub>0</sub>) is not expected, but, this particular batch of WS<sub>2</sub> monolayers possesses intrinsic defects and the emission D<sub>0</sub> at 660 nm can be observed.

$$I = \log\left(\frac{A}{1 + B \cdot e^{-\frac{E_a}{kT}}}\right) \quad (5.1)$$

Figure 5.4b is the plot of the log of intensity of D<sub>0</sub> against the inverse of temperature. This curve was then fitted with modified Arrhenius equation 5.1 (where A, B, and k are constants) shown as red dashed line. [Jiang88] From the fit, activation energy (E<sub>a</sub>) of 30 meV was obtained. This is close to the thermal energy at RT ( $\approx$  25 meV).

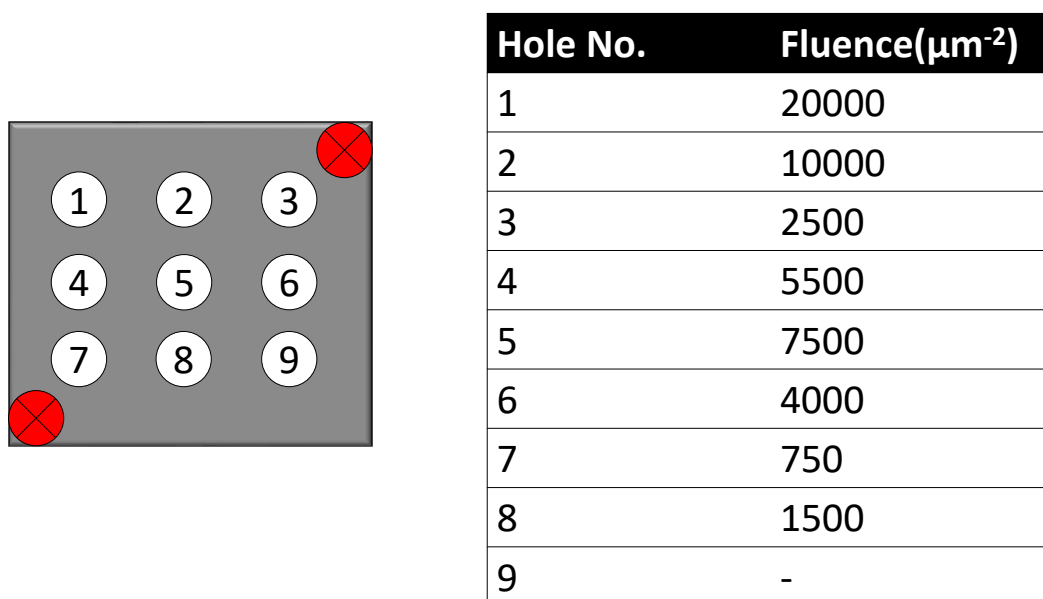


Figure 5.5: Mask showcasing nine numbered holes and a table displaying the  $\text{Xe}^{30+}$  ion irradiation fluences corresponding to the hole number.

To get an insight into this defect-bound luminescence, defects were intentionally created by irradiating the monolayers of  $\text{WS}_2$  with  $\text{Xe}^{30+}$  ions with different fluences. For this purpose, the sample was covered with a mask containing 9 distinguishable holes in it and each hole was irradiated with different fluences (shown in Figure 5.5) of  $\text{Xe}^{30+}$  ions with the potential energy of 15.4 keV and the kinetic energy of 180 keV under perpendicular incidence. The irradiation of  $\text{WS}_2$  monolayers with  $\text{Xe}^{30+}$  ions was done by Dr. Roland Kozubek in the group of Prof. Marika Schleberger at the University of Duisburg-Essen.

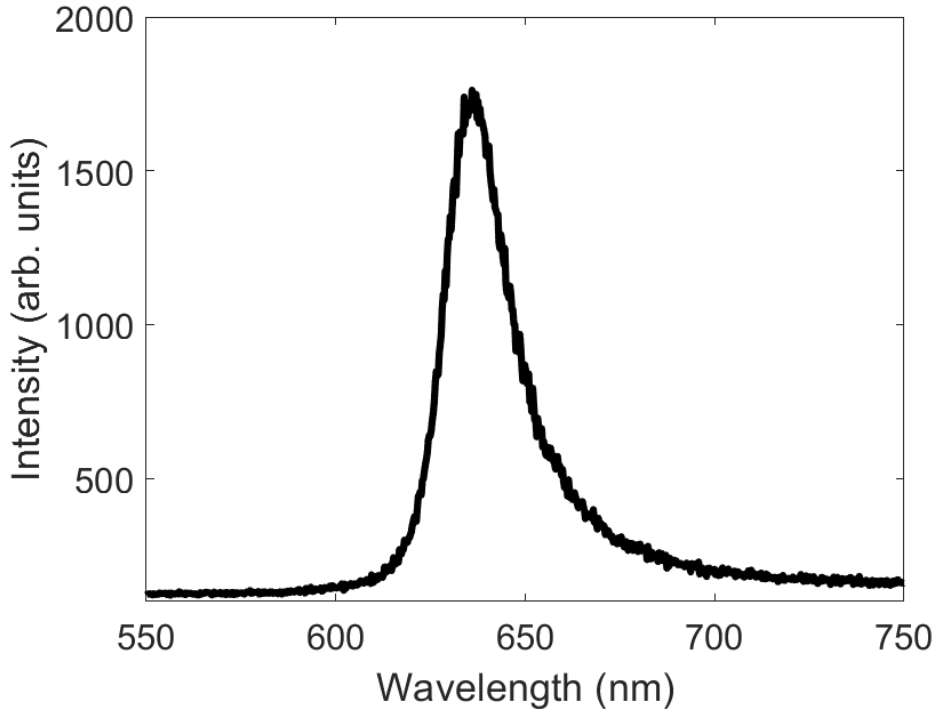


Figure 5.6: PL spectrum at 260K from WS<sub>2</sub> monolayer irradiated with 2500  $\mu\text{m}^{-2}$  fluence.

Irradiation with Xe<sup>30+</sup> ions on the monolayer flakes of WS<sub>2</sub> on Si/SiO<sub>2</sub> substrate is expected to create defects. The accurate physical processes of defect creation that might happen are still unknown. The known facts are when these ions bombard free standing 2D materials, they make pores with sizes ranging in tens of nanometers depending on the irradiation parameters. [Kozubek19] If that is the case for a monolayer on a substrate, intuitively, we should not expect defect-bound emissions from large pores. For larger fluences e.g. 6000  $\mu\text{m}^{-2}$ , ions should bombard every 12-15 nm and therefore the sample is expected to be destroyed. Figure 5.6 shows the PL spectrum from an irradiated WS<sub>2</sub> monolayer, with the irradiation fluence of 2500  $\mu\text{m}^{-2}$  at 260 K. The exciton-trion emission band is slightly broader than that of the pristine sample, but, no defect-bound emissions were observed at 260 K.

Temperature dependent PL spectra were collected whilst cooling down the irradiated sample from 260 K down to 83K as shown in Figure 5.7a for flakes irradiated with 2500  $\mu\text{m}^{-2}$  fluence of Xe<sup>30+</sup> ions. The irradiated sample showed defect-bound emission D<sub>0</sub> emission at 670 nm similar to that of the pristine sample with only a slight shift of 10 nm, that means, similar kind of optically active defects were formed due to the irradiation. The main differences in the temperature-dependent PL between the irradiated flake and the pristine flake are, D<sub>0</sub> emission was observed at higher temperature of 160 K compared to 100 K in case of the pristine flake. The intensity ratio of D<sub>0</sub> emission with respect to X<sub>0</sub> is larger for an irradiated flake than the pristine flake. Figure 5.7b is the log of intensity against the temperature plot of D<sub>0</sub> emission, a modified Arrhenius fit gives activation energy ( $E_a$ ) of 62 meV.

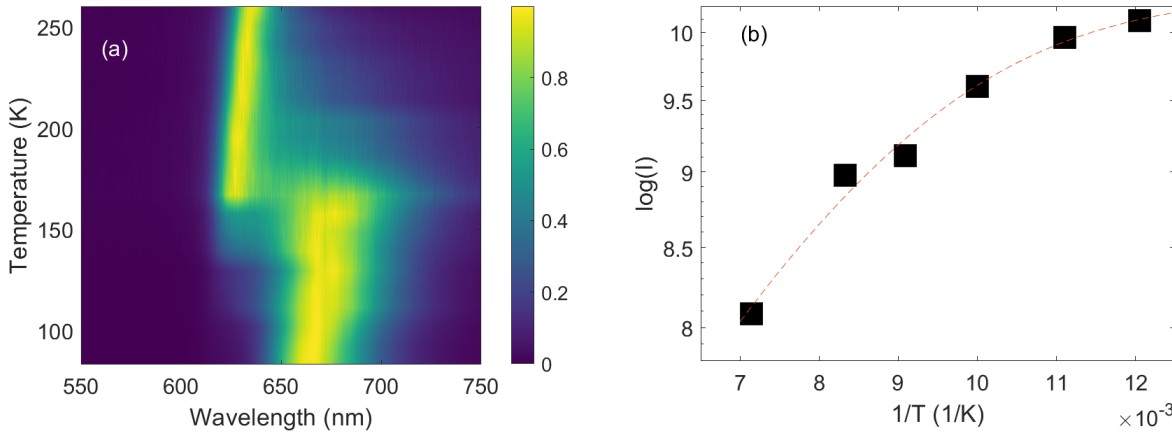
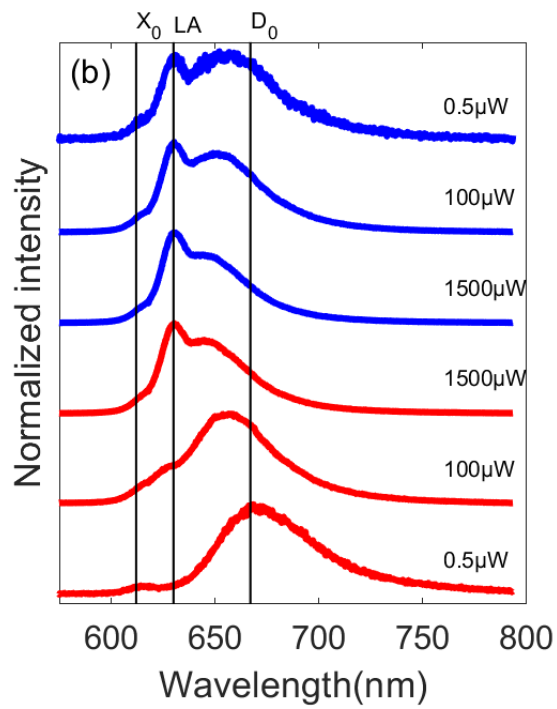
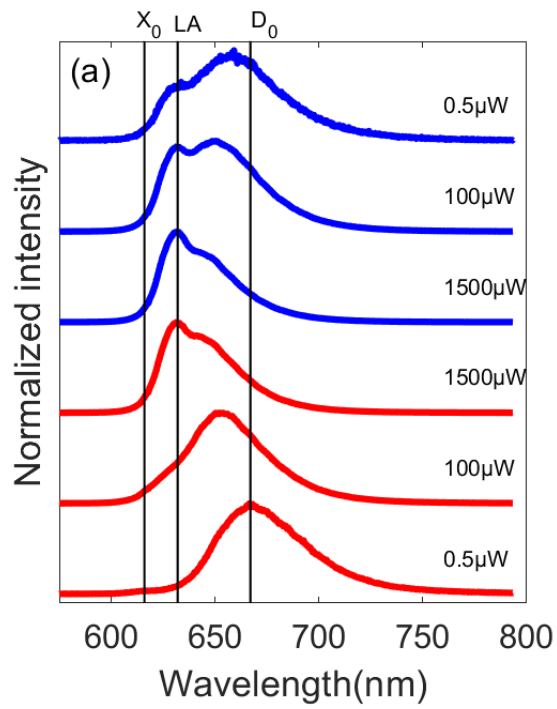


Figure 5.7: (a) PL spectrum of monolayer  $\text{WS}_2$  at different temperatures at  $1.5 \mu\text{W}$  excitation power with  $2500 \mu\text{m}^{-2}$  fluence (b) modified Arrhenius plot of the defect emission over temperature.

Figure 5.8a, 5.8b, and 5.8c shows LT-PL (at 83 K) spectra of sample 1 after irradiation with  $\text{Xe}^{30+}$ -ions with different fluxes of  $750 \mu\text{m}^{-2}$ ,  $4000 \mu\text{m}^{-2}$ , and  $5500 \mu\text{m}^{-2}$  at different excitation powers. With increasing power, the emission properties of the  $\text{D}_0$  band changes and shows different changes from samples irradiated with different fluences. This excitation power-dependent PL measurement is then called "laser processing or laser treatment". The laser processing procedure is the following: First the PL spectrum was collected from a single flake at a low excitation power of  $0.5 \mu\text{W}$  followed by the collection of PL spectra at  $10 \mu\text{W}$ ,  $50 \mu\text{W}$ ,  $100 \mu\text{W}$ ,  $300 \mu\text{W}$ ,  $700 \mu\text{W}$  and  $1500 \mu\text{W}$  to obtain the gradual changes that happen due to the increasing power. To check the persistence of the laser induced effects, PL spectra were collected with decreasing power, in the order:  $1500 \mu\text{W}$ ,  $700 \mu\text{W}$ ,  $300 \mu\text{W}$ ,  $100 \mu\text{W}$ ,  $50 \mu\text{W}$ ,  $10 \mu\text{W}$  and finally to  $0.5 \mu\text{W}$  where the laser induced change in the PL can be rather clearly observed. Initially, the PL spectra are dominated by a broadband at  $\approx 670\text{nm}$ . The excitonic emission is only barely visible in both pristine and irradiated samples at LT, if the region around  $610\text{nm}$  is magnified contrary to the situation at RT, where the PL emission only exhibits the excitonic contribution (see Figure 5.3) also for the irradiated flakes within sample 1 (see Figure 5.6). With increasing excitation power the emission band at  $670\text{nm}$  shifts towards lower wavelengths to  $\approx 648\text{nm}$ .

Additionally, a new laser activated peak (LA) starts to evolve at  $\approx 630\text{nm}$ . This peak persists also after reducing the excitation power to  $0.5 \mu\text{W}$  again. The emission band at larger wavelengths shifts back to  $\approx 655\text{nm}$  and increases in intensity compared to the LA peak as shown in Figure 5.8a for a flake irradiated with  $750 \mu\text{m}^{-2}$  fluence. Figure 5.8b and 5.8c show the similar power series for  $4000 \mu\text{m}^{-2}$  and  $5500 \mu\text{m}^{-2}$   $\text{Xe}^{30+}$ -ion fluxes irradiated  $\text{WS}_2$  monolayer flakes, respectively.



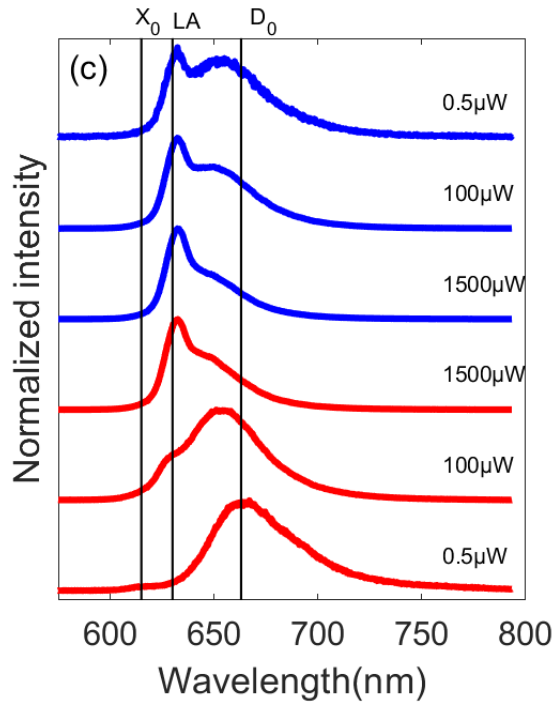


Figure 5.8: PL spectra of sample 1 at 83 K at different excitation power for flakes irradiated with (a)  $750 \mu\text{m}^{-2}$ , (b)  $4000 \mu\text{m}^{-2}$  and (c)  $5500 \mu\text{m}^{-2}$  of  $\text{Xe}^{30+}$  ions.

Similar behaviour was reported by He et al., who investigated pristine and aged  $\text{WS}_2$  monolayers. They observed the emergence of a new peak for aged  $\text{WS}_2$ -flakes at  $\approx 630\text{nm}$  after cryogenic laser processing. He et al., in their report, they assigned this peak to a degradation-related feature, which could be hidden by adsorbates covering the  $\text{WS}_2$ -sheet and leading to the emission band  $\text{D}_0$  (in their report named LS at  $\approx (645 \text{ to } 655) \text{ nm}$ ). [He16b] For our  $\text{Xe}^{30+}$ -ion irradiated sample we observed the appearance of a similar feature after laser processing. This observation leads to the conclusion, that the origin of the LA peak cannot exclusively be a hint for aged samples, but can also be related to defects which can be formed by aging and irradiation like extended and/or adsorbate decorated defect complexes. The observed shift of the  $\text{D}_0$  emission band could have different origins. We exclude the temperature or strain induced variation of the bandgap or shifting related to a change in the dielectric environment. This is due to the fact, that there is no shift visible either for the excitonic emission, which should respond strongest on the above-mentioned variations, nor for the new LA peak. One possibility could be the removal of physisorbed adsorbates leading to a change in the energetic position of the defect emission state within the bandgap. This situation is not so unlikely since it is known and reported that laser excitation could lead to evaporation of adsorbates from the surface. But there is still the fact, that the emission band shifts back after reducing the power again. Since we are still in a vacuum ( $5 \times 10^{-6} \text{ mbar}$ ) and at 83K, it is not so likely that adsorbates removed from the surface will return into their original configuration. Another possibility might be that the observed shift of the  $\text{D}_0$  band is not a real "shift" at all, but that there are more energetic states in between the  $\text{D}_0$  emission band and the new LA peak. This could lead to an unresolved strong increase in emission intensity of these intermediate states when increasing the laser power leading to the impression of a gradual shift of the  $\text{D}_0$  emission band to lower wavelengths. Increasing the power further leads to a stronger increase in the LA peak. This gradually changing behaviour might be due to different density of states of the emission. Upon

increasing the laser power, saturation of states higher in wavelength could be one reason for the observed shift of the  $D_0$  emission band. Another explanation could be that the adsorbate-defect complex can transform into an excited state with higher energy by increasing the laser power and therefore leading to the observed shift of the  $D_0$  band. Still, it has to be noted that a part of these states responsible for the  $D_0$  emission band undergoes a persistent transformation at low temperature. Because the LA peak, which is exclusively generated by the laser processing, is still visible after reducing the excitation power. This is also in accordance with the report of He et al., who observed a complete vanishing  $D_0$  emission band and a strong emission of the LA peak (named U peak in their publication) after reducing the excitation power. [He16b] They also reported that the LA peak completely vanishes after cycling the temperature to RT and back to LT again. These observations lead to a conclusion that, LA emission originates from undecorated defects, which is lost after a temperature cycle as the adsorbates gets reattached to the defects sites and alters the emission.

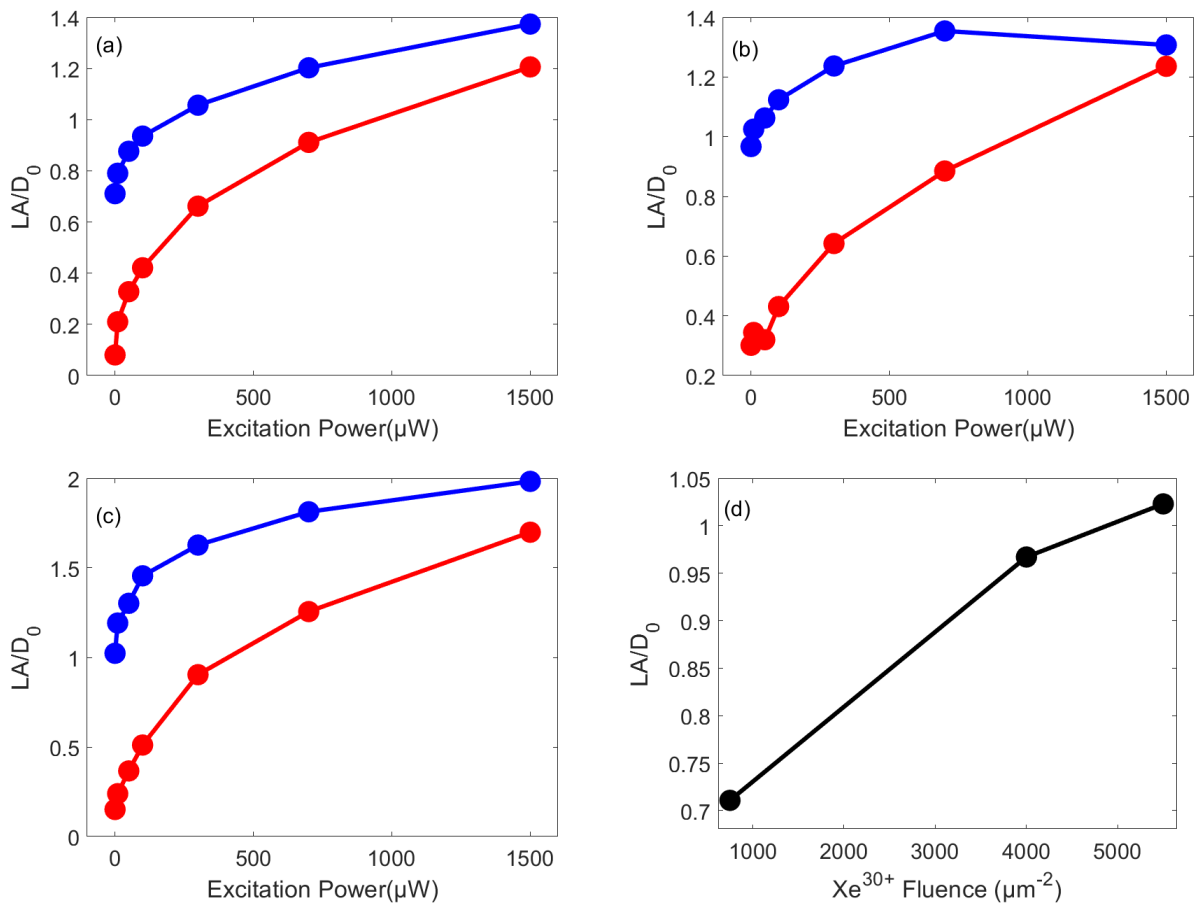


Figure 5.9: Evolution of LA to  $D_0$  ratio with respect to excitation power for sample 1 irradiated with (a)  $750 \mu\text{m}^{-2}$  (b)  $4000 \mu\text{m}^{-2}$ , (c)  $5500 \mu\text{m}^{-2}$  fluence of  $\text{Xe}^{30+}$  and (d) LA to  $D_0$  ratio at  $0.5 \mu\text{W}$  excitation power after laser processing against  $\text{Xe}^{30+}$  fluence.

The three differently irradiated flakes show a very similar behavior during laser processing. The difference is that for higher  $\text{Xe}^{30+}$ -ion fluxes, after the laser treatment, intensity ratio between the LA peak and the emission band  $D_0$  increases with increasing ion-flux. Figure 5.9a, 5.9b, and

5.9c shows the intensity ratio between the LA peak and D<sub>0</sub> band for the flake irradiated with 750  $\mu\text{m}^{-2}$ , 4000  $\mu\text{m}^{-2}$  and 5500  $\mu\text{m}^{-2}$  respectively. It is found, that the ratio starts to increase while increasing the power to the maximum value (red data points) and then decreasing again (blue data points). After reaching the lowest excitation power again, the ratio shows a significantly higher value compared to the starting point. Evaluating just the ratio at the end of our laser processes for all three differently irradiated flakes (see Figure 5.9d), it clearly exhibits the following trend, that is, with increasing irradiation flux the ratio increases starting at a ratio of 0.7 for 750  $\mu\text{m}^{-2}$  flux and increasing to 1.05 for 5500  $\mu\text{m}^{-2}$  Xe<sup>30+</sup>-ion flux. This indicates that defect densities play a more important role in laser processing to LA. He et al., observed that, for aged samples, laser processing to LA ("U" in their publication) is more pronounced, which is in good agreement with our results as more aging potentially results in more defects. The sample-space in this study is, still not enough to generalize this trend. Unfortunately, since the sample was destroyed, PL measurements (mainly excitation power-dependent measurement at LT and temperature cycles) on flakes irradiated with different fluences could not be performed.

## Conclusion

In conclusion, a monolayer WS<sub>2</sub> has a single asymmetric emission band around 630 nm near room temperature. Asymmetry is due to a contribution from trion emission slightly at lower energy along with neutral exciton emission. Low temperature PL from a pristine WS<sub>2</sub> monolayer shows, besides a blue shifted exciton emission (615 nm) an additional emission band D<sub>0</sub> at 660 nm related to an intrinsic defect-bound emission band. Xe<sup>30+</sup> ions with different fluences were irradiated on the WS<sub>2</sub> monolayers to intentionally create defects. Irradiated flakes show a slightly shifted D<sub>0</sub> emission at 670 nm. Defect bound emission from irradiated samples undergo low temperature laser processing, resulting in a new emission band (LA) which is reversible with temperature cycles. Also, we find a correlation between the density of defects (Xe<sup>30+</sup> ions fluences) and the amplitude of LA emission with respect to the D<sub>0</sub> emission and quantified the laser processing effect with LA/D<sub>0</sub> ratio.

### 5.4.2 WS<sub>2</sub> sample batch 2

Low temperature PL studies of WS<sub>2</sub> monolayers revealed defect-bound emission properties from flakes of batch 1. As mentioned in the previous section, further measurements could not be performed. For further studies, we obtained another sample nominally grown with the same parameters. WS<sub>2</sub> monolayers from batch 2 were synthesized in a similar way as batch 1 and the emission properties were expected to be similar.

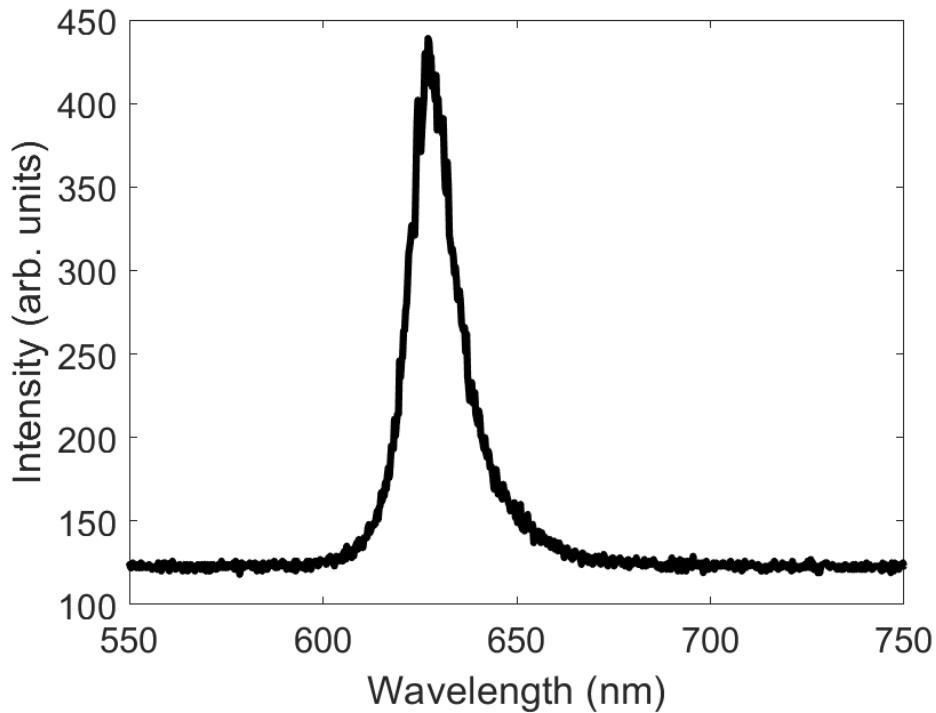


Figure 5.10: PL spectrum of monolayer WS<sub>2</sub> at RT.

Figure 5.10 shows the PL spectrum at RT from an as-synthesized pristine WS<sub>2</sub> monolayer flake from batch 2. PL spectrum at room temperature shows only one asymmetric emission band at 628 nm with contributions from the recombination of excitons and trions. As observed for the flakes from batch 1, no defect-bound emissions were observed in the RT PL spectrum. Figure 5.11 is a 2D plot consisting of PL spectra at different temperatures and colorbar shows the normalized intensity. The bottom line in the 2D plot corresponds to the spectrum at 83K and the top to 260K. In this temperature-dependent PL spectroscopy, only one asymmetric emission band at 610 nm due to the exciton and trion recombination was observed at LT, contrary to the observation from the pristine flakes from batch 1, where defect-bound emission at 660 nm was observed due to intrinsic defects present in as-synthesized monolayer flakes. A blue shift in the exciton and trion emission energy was also observed with decreasing temperature.

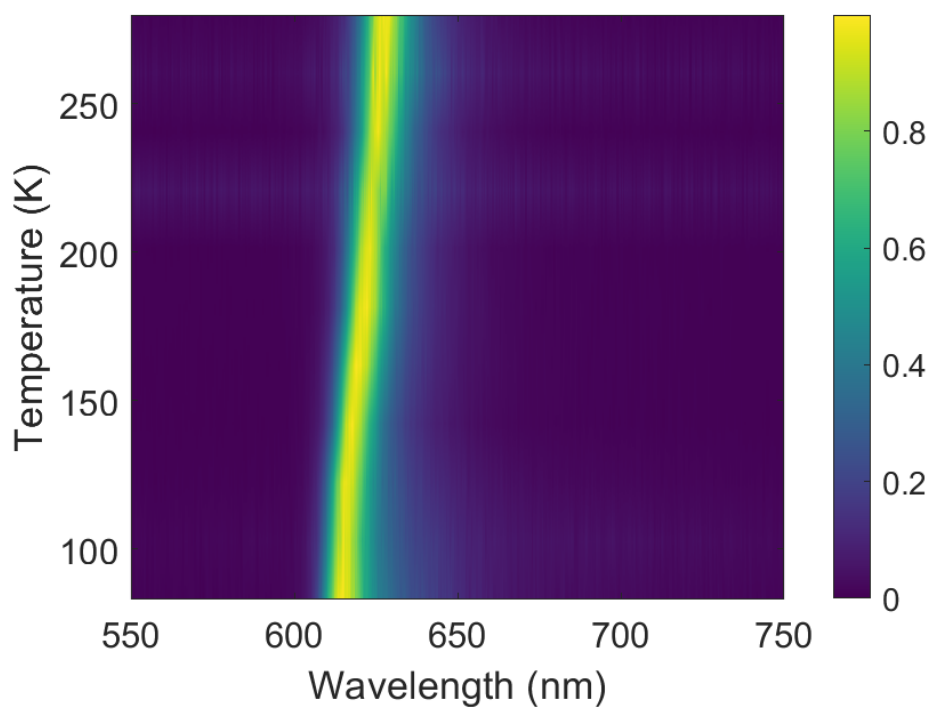


Figure 5.11: PL spectrum of monolayer WS<sub>2</sub> at different temperatures at 1.5  $\mu$ W excitation power.

No defect-bound emission from WS<sub>2</sub> monolayer flakes from batch 2 indicates that there is no optically active defect present in them. This indicates the higher quality of the samples from batch 2 compared to batch 1. A sample without optically active defects is well suited and desirable for further experiments where defects were created intentionally with Xe<sup>30+</sup> ions.

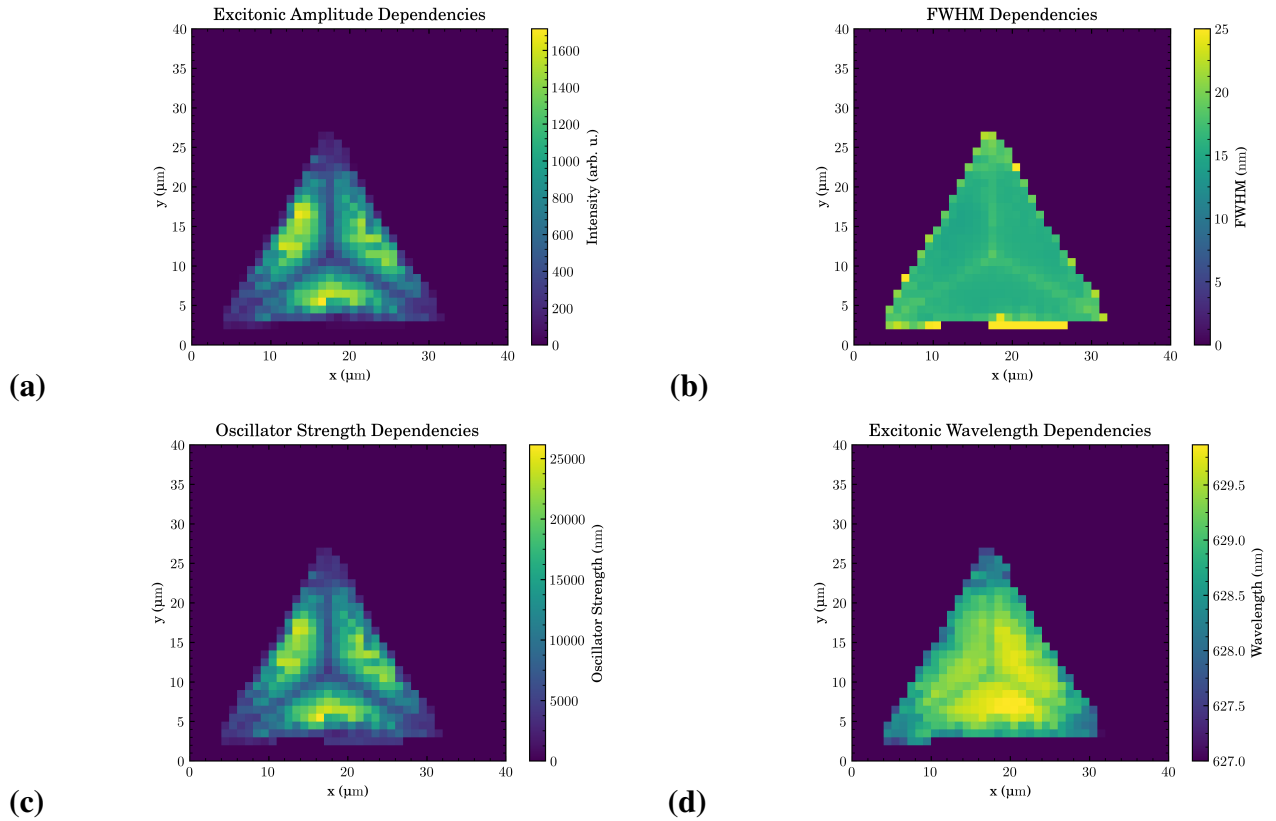


Figure 5.12: Spatial PL map of WS<sub>2</sub> monolayer showing (a) Excitonic amplitude dependency, (b) Full width half maxima (FWHM) dependency, (c) oscillator strength dependency and (d) peak excitonic wavelength dependency.

To further check the quality of the pristine flakes, a room temperature PL mapping was performed and the important details are summarized in Figure 5.12. Figure 5.12a shows the excitonic amplitude distribution across the flake. We see that the excitonic amplitude along with the oscillator strength (Figure 5.12c) are not homogeneously distributed across the flake. The main reason behind the inhomogeneity is the growth mechanism. The three lines emerging from the centre of the flake and going all the way to the corner of the triangle shows less PL intensity. This behaviour can be attributed to the presence of grain boundaries along these lines, which is also the case for the PL intensity drop observed in the edges. Figure 5.12b shows FWHM dependencies across the flake, FWHM value of 15 nm was observed homogeneously within the flake which is (2-4) nm broader on the grain boundaries. Last, but not least, the excitonic emission wavelength (peak wavelength at 628 nm) is homogeneous across the flake with shift  $\Delta\lambda$  of less than 1 nm was observed (see Figure 5.12d). This homogeneity in the emission wavelength indicates no variation in strain across the flake. [He16a] High quality of the sample with no optically active defects makes it suitable for the upcoming study.

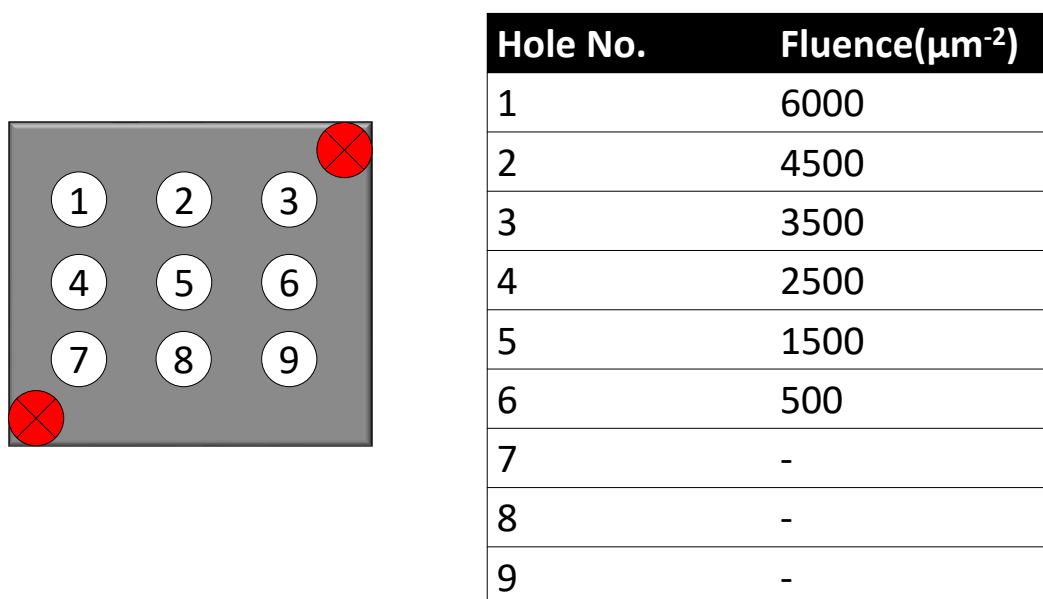


Figure 5.13: Mask showcasing nine numbered holes and a table displaying the  $\text{Xe}^{30+}$  ion irradiation fluences corresponding to the hole number.

Figure 5.13 shows a similar mask that was used for the flakes from batch 1 (Figure 5.5), except that, we did not use fluences beyond  $6000 \mu\text{m}^{-2}$  as higher fluences such as  $10000 \mu\text{m}^{-2}$  and above destroyed the complete PL of those monolayers. For the flakes from batch 2, the lowest fluence of  $\text{Xe}^{30+}$  ions used was  $500 \mu\text{m}^{-2}$  in hole number 6 and was increased to  $6000 \mu\text{m}^{-2}$  in the following steps:  $500 \mu\text{m}^{-2}$ ,  $1500 \mu\text{m}^{-2}$ ,  $2500 \mu\text{m}^{-2}$ ,  $3500 \mu\text{m}^{-2}$ ,  $4500 \mu\text{m}^{-2}$  and  $6000 \mu\text{m}^{-2}$  from hole 6 to hole 1 respectively. Flakes in hole number 7-9 were left un-irradiated for reference and for studying the defect-bound emission properties that arise due to aging.

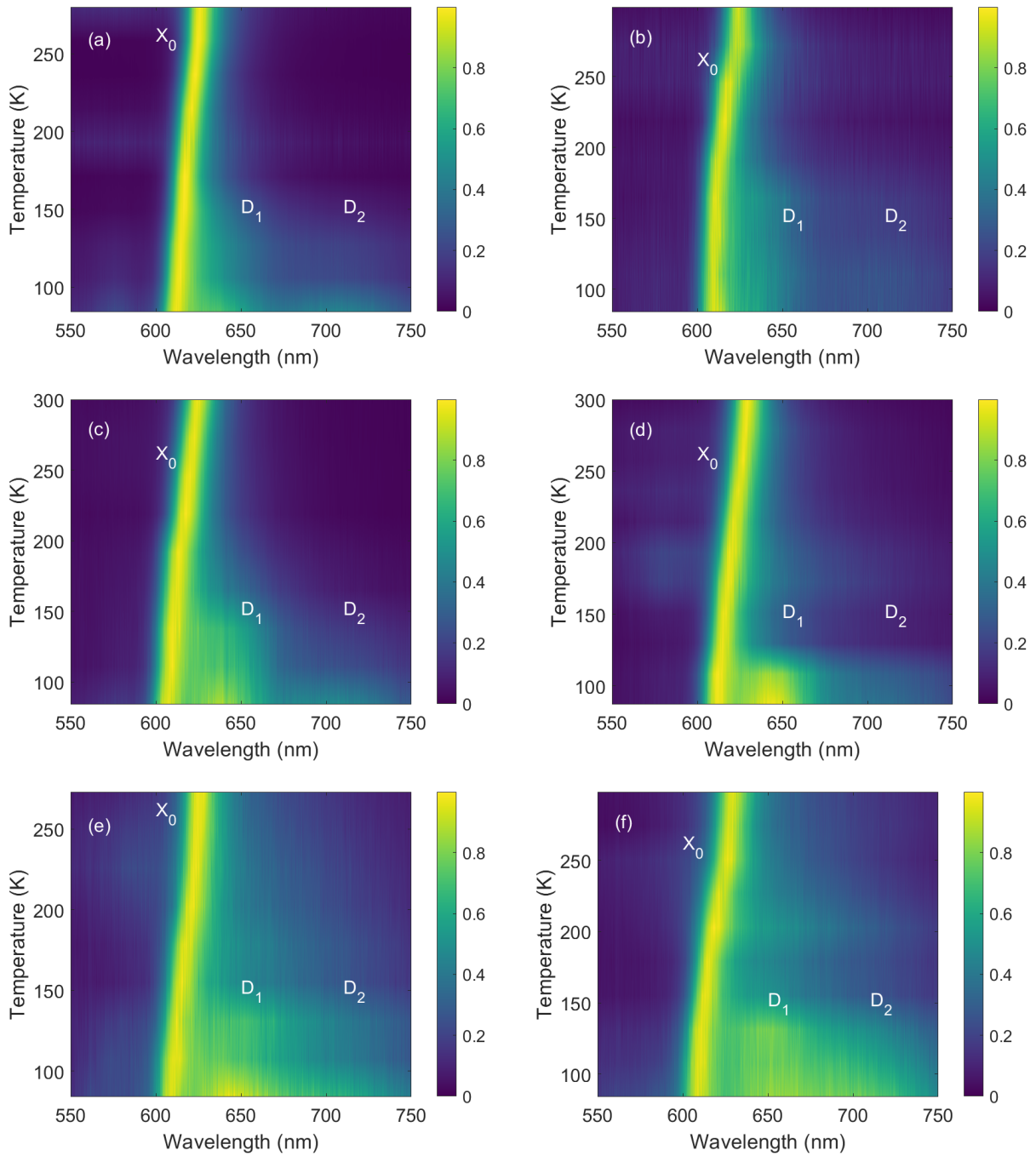


Figure 5.14: PL spectrum at different temperatures at  $1.5 \mu\text{W}$  excitation power of monolayer  $\text{WS}_2$  irradiated with the  $\text{Xe}^{30+}$  fluences of (a)  $500 \mu\text{m}^{-2}$ , (b)  $1500 \mu\text{m}^{-2}$ , (c)  $2500 \mu\text{m}^{-2}$ , (d)  $3500 \mu\text{m}^{-2}$ , (e)  $4500 \mu\text{m}^{-2}$  and (f)  $6000 \mu\text{m}^{-2}$ .

Figure 5.14a-f are the 2D plots displaying temperature-dependent PL spectra of  $\text{Xe}^{30+}$  ion irradiated flakes with the irradiation fluences of  $500 \mu\text{m}^{-2}$ ,  $1500 \mu\text{m}^{-2}$ ,  $2500 \mu\text{m}^{-2}$ ,  $3500 \mu\text{m}^{-2}$ ,  $4500 \mu\text{m}^{-2}$  and  $6000 \mu\text{m}^{-2}$  respectively. Figure 5.14a shows the temperature-dependent PL from  $\text{WS}_2$  monolayer irradiated with  $500 \mu\text{m}^{-2}$  fluence. For the temperatures below 100K, two additional defect-bound emission bands arise, besides the exciton emission band. Presence of two defect-bound emission bands is different from the PL behaviour from flakes of batch 1, where only  $D_0$  is present. With increasing fluence, the temperature at which the defect-bound emissions are visible, increases. For example, for  $500 \mu\text{m}^{-2}$ , it is observable below 100 K and for  $6000 \mu\text{m}^{-2}$ , defect-bound emissions are observable below 160 K. Increasing fluences result in increase in defect density and thereby defect-bound emissions are observed even at higher temperatures.

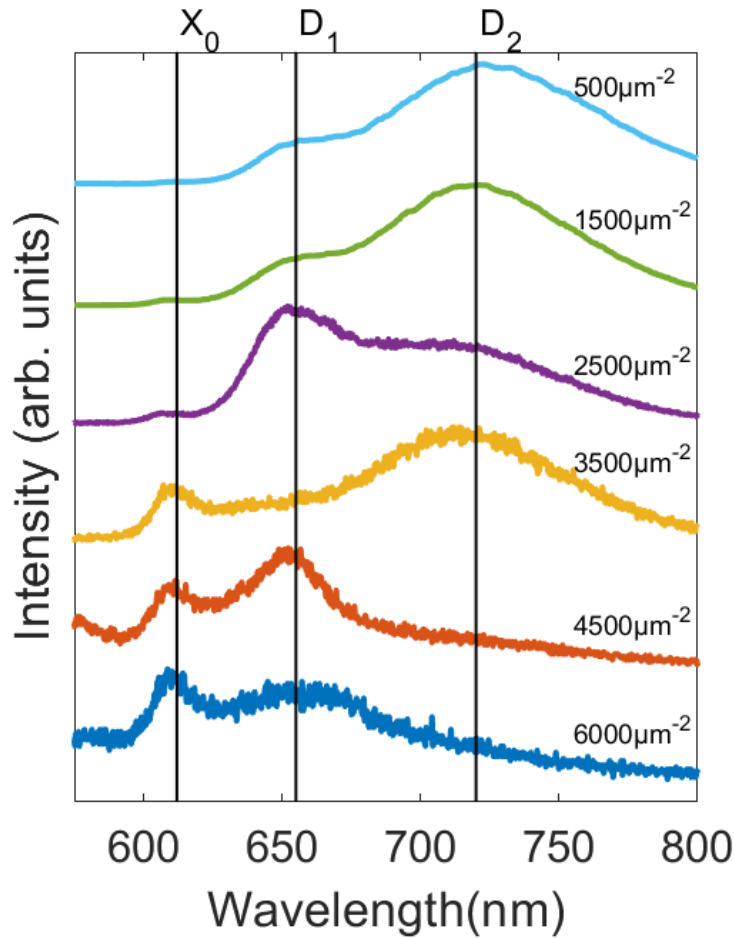


Figure 5.15: Low temperature normalized PL spectra of  $\text{WS}_2$  monolayers irradiated with different fluences of  $\text{Xe}^{30+}$  ions. The two bands  $D_1$  and  $D_2$  related to defects are always observable in different intensities besides the excitonic contribution.

For comparison, when we look at the spectra at 83K for all fluences and plot them in a stack plot, as shown in Figure 5.15, we observe that the overall PL intensity drops down with increasing fluences. As mentioned before, there are two additional emission bands, besides the exciton emission band and these additional bands are attributed to defect-bound emissions  $D_1$  and  $D_2$  at 650 nm and 720 nm respectively. For flakes irradiated with fluences from  $500 \mu\text{m}^{-2}$  up to  $3500 \mu\text{m}^{-2}$ , defect-bound emissions dominate the PL spectra and for fluences of  $4500 \mu\text{m}^{-2}$  and  $6000 \mu\text{m}^{-2}$  it

is rather an excitonic emission that dominates. This is puzzling, as larger fluences should constitute larger defect densities and hence larger defect-bound emissions compared to the respective exciton emission is expected. The reason for this behaviour is, when the defect densities become larger, it is highly probable that those defects (mainly point defects) would rearrange itself to form energetically favourable defect complexes (e.g. nano-pores) which can potentially be non-radiative. Nevertheless, as mentioned in the previous section, for a fluence of  $6000 \mu\text{m}^{-2}$   $\text{Xe}^{30+}$  ion should have an impact at the flake for every 12 nm and for a free-standing TMDC monolayers, these ions creates nano-pores. [Kozubek19] Exciton emission from such flakes is still seen albeit with low intensities. Loss in the intensity is attributed to material loss due to the larger defect formation. The intensities from  $D_1$  and  $D_2$  emission tends to show a trend with the fluence.  $D_2$  emission dominates the spectra for lower fluences and  $D_1$  for higher fluences. PL spectrum from the flake irradiated with  $2500 \mu\text{m}^{-2}$  fluence deviates from the trend, this might be due to a shadowing effect during the irradiation process. Domination of  $D_2$  emission for flakes irradiated with lower fluences tells us that,  $D_2$  is most likely due to simple defects such as sulphur vacancies decorated with physisorbed adsorbates. Carozo et al, in their report, mentioned that the emission around 710 nm is due to the sulphur vacancy defects. [Carozo17] And for  $D_1$  emission, the origin of this is still unknown, but, from the results we observe, we could attribute this to defect complexes along with adsorbates that make them radiative. [Tongay13]

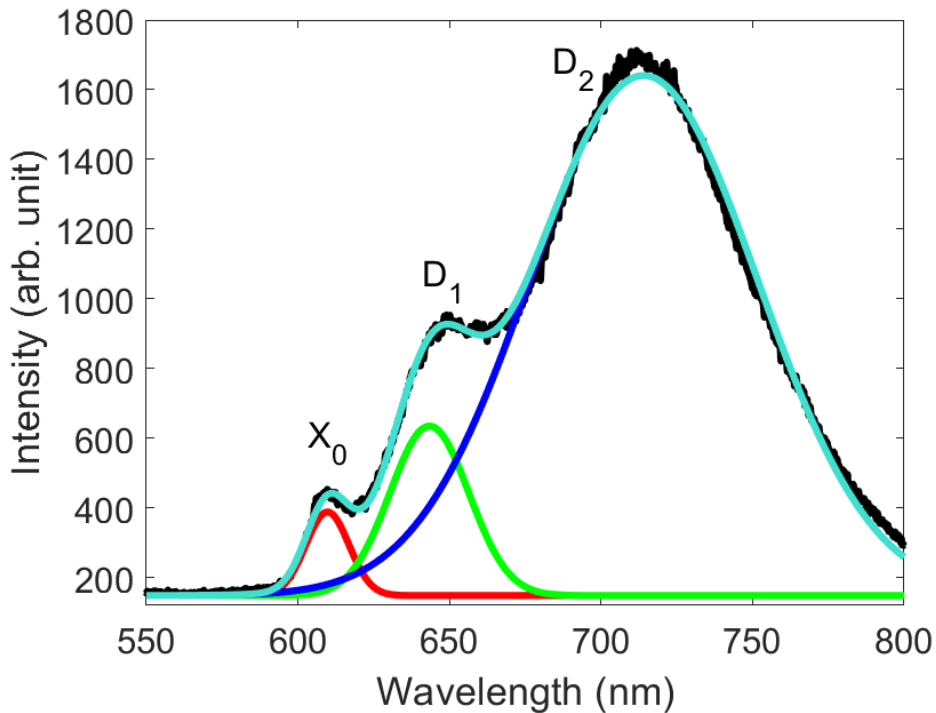


Figure 5.16: PL spectrum at 83K of monolayer  $\text{WS}_2$  irradiated with  $\text{Xe}^{30+}$  ion fluence of  $1500 \mu\text{m}^{-2}$  showing three emissions  $X_0$ ,  $D_1$  and  $D_2$  fitted with three Gaussian curves.

Focusing only on flakes irradiated with  $1500 \mu\text{m}^{-2}$  fluence, Figure 5.16 shows the spectrum at 83K, with  $10 \mu\text{W}$  excitation power. The spectrum can be fitted almost perfectly with three Gaussian curves. The same is true for all the fluences at low excitation power.

For  $\text{WS}_2$  monolayers from batch 1, at low temperature, the  $D_0$  emission can be laser processed

to a new defect-bound emission peak LA, which increases in intensity as the defect density was increased (with  $\text{Xe}^{30+}$  ion irradiation). To check how the defect-bound emissions from  $\text{WS}_2$  monolayers from batch 2 behave, we adapted the same laser processing experiment procedure. To repeat, PL from the flakes at 83K were recorded at increasing laser excitation power starting from  $0.5 \mu\text{W}$  up to  $1500 \mu\text{W}$  in the sequence:  $0.5 \mu\text{W}$ ,  $10 \mu\text{W}$ ,  $50 \mu\text{W}$ ,  $100 \mu\text{W}$ ,  $300 \mu\text{W}$ ,  $700 \mu\text{W}$  and  $1500 \mu\text{W}$ . Flakes were then subjected to a decreasing power from  $1500 \mu\text{W}$  down to  $0.5 \mu\text{W}$ , to observe the effect of the laser exposure. An argument to support the scheme of this experiment rather than, exposure to high power for a certain time, like He et al., reported in their article [He16b] was that, we could see the evolution of the changes in the defect-bound emission.

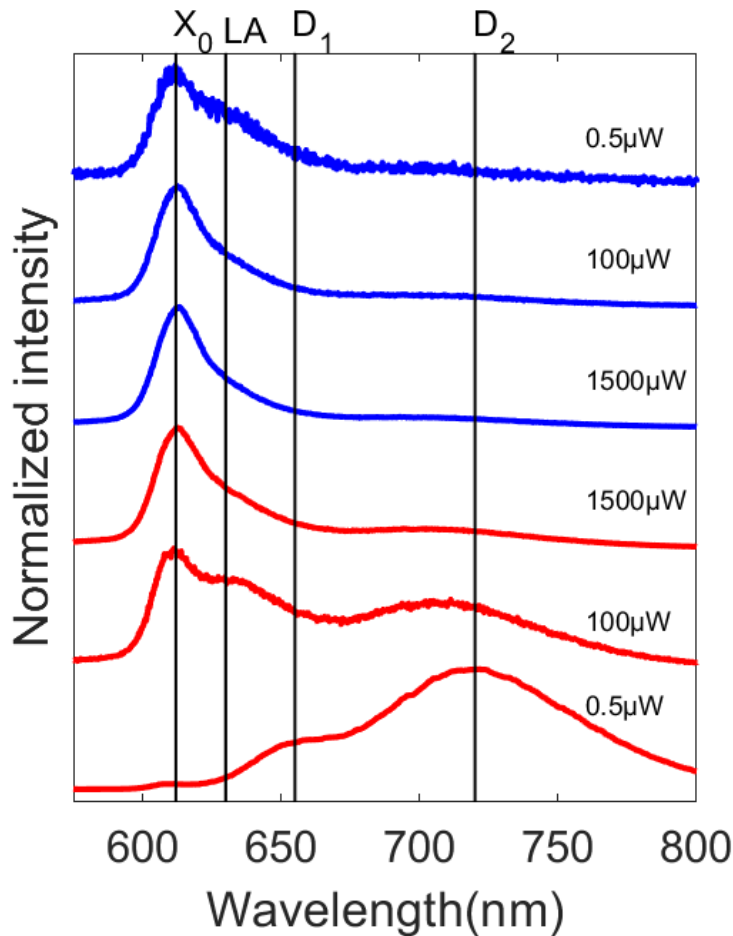


Figure 5.17: PL spectra of  $\text{WS}_2$  monolayer at 83K at different excitation power for flakes irradiated with  $1500 \mu\text{m}^{-2}$  fluence of  $\text{Xe}^{30+}$  ions.

For further studies, we first take a look at the excitation power-dependent PL spectra of a  $\text{WS}_2$  monolayer flake irradiated with  $1500 \mu\text{m}^{-2}$  fluence of  $\text{Xe}^{30+}$  ions. Figure 5.17 shows the stack plot containing PL spectra recorded at increasing excitation power ( $0.5 \mu\text{W}$ ,  $100 \mu\text{W}$ , and  $1500 \mu\text{W}$ ) shown in red lines and subsequently with decreasing excitation power in blue lines. Initially, at low excitation power, PL was dominated by  $D_2$ . With increasing excitation power free exciton emission increases more than the  $D_1$  and  $D_2$ . At the highest excitation power, the spectra are dominated by  $X_0$  emission. Whilst decreasing the excitation power, unlike the  $\text{WS}_2$  monolayers from batch 1, where,  $D_0$  emission band was always persistent. Here,  $D_2$  emission band vanishes

almost completely and  $D_1$  emission band probably evolves into a different defect-bound emission (LA) at 630 nm after laser processing, like the flakes from batch 1. Interestingly, no gain in the exciton emission was observed, even after such a decrease in the defect-bound emissions as shown in Figure 5.18. Similar results were observed for flakes irradiated with other fluences as well (see Figure A.6, A.7, A.8, A.9 and A.10).

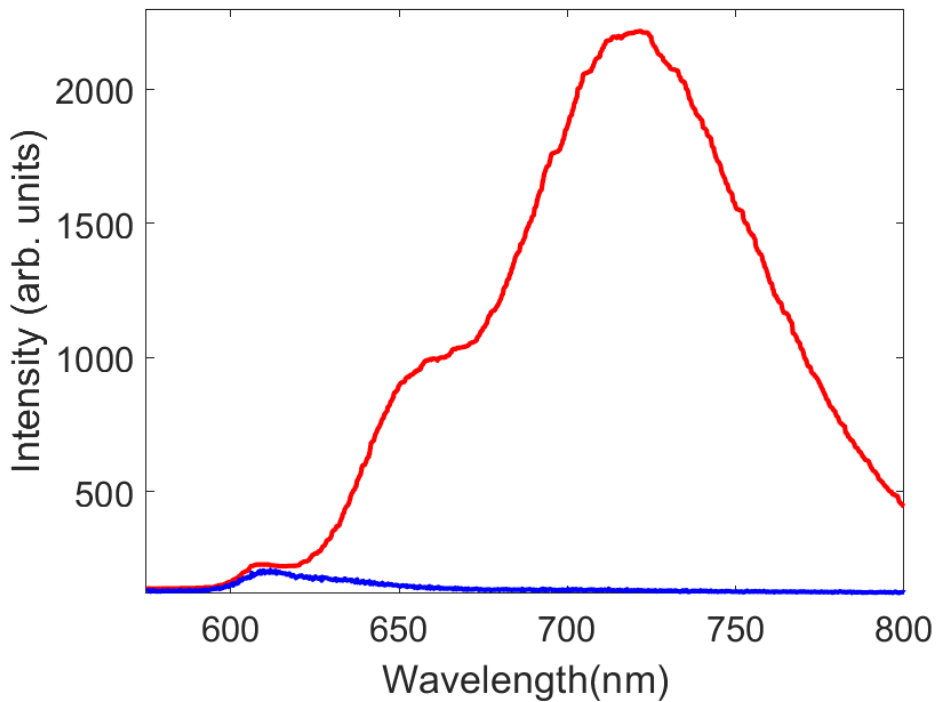


Figure 5.18: PL spectrum of monolayer  $WS_2$  at 83K before (red) and after (blue) laser processing.

Figure 5.19a and 5.19b show the intensity and wavelength dependence of exciton recombination (red),  $D_1$  emission (green) and  $D_2$  emissions (blue) with changing excitation power. In Figure 5.19a, a clear linear dependence of emission due to exciton recombination was observed, whereas,  $D_1$  and  $D_2$  show a sub-linear dependence. Sub-linear dependence in  $D_1$  is attributed to the limitation in the number of defect site responsible, as the total number is rather expected to be finitely limited compared to free exciton and hence the sub-linearity. In case of  $D_2$ , we also observed a complete absence of  $D_2$  intensities after  $700 \mu W$ , that means, besides the limited number of such defects, there is also annealing of those defects that reduces the number further down.

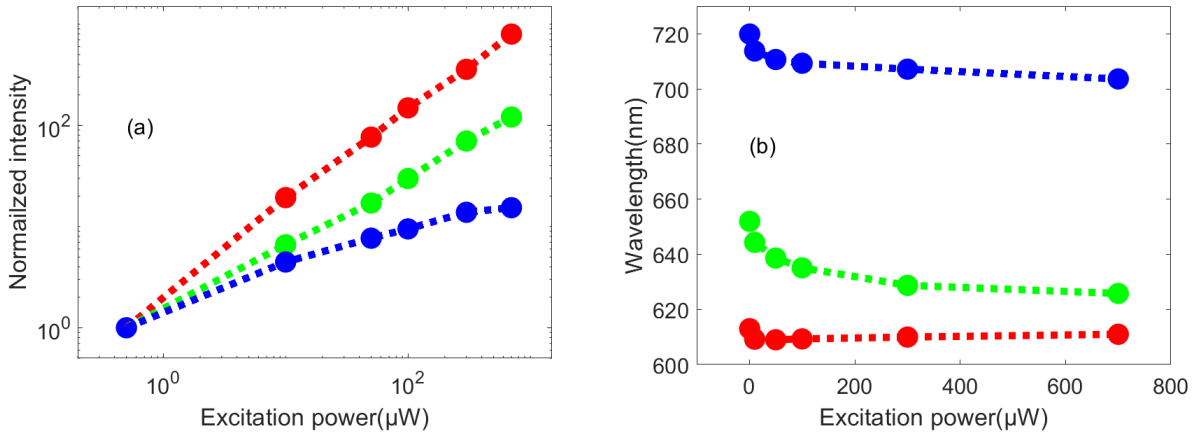


Figure 5.19: (a) Double logarithmic plot of intensity against excitation power and (b) peak emission wavelength against excitation power for X<sub>0</sub> (red), D<sub>1</sub> (green) and D<sub>2</sub> (blue).

Besides the lowering of intensities in D<sub>1</sub> and D<sub>2</sub> emissions, we observed a blue shift in the emission maxima of D<sub>1</sub> and D<sub>2</sub> emissions as shown in Figure 5.19b. D<sub>2</sub> emission maximum shows a shift from 720 nm to 700 nm until the excitation power of 700  $\mu\text{W}$  whilst increasing power, after which D<sub>2</sub> emission almost vanishes even when the excitation power was decreased to 0.5  $\mu\text{W}$  (see Figure 5.17). D<sub>1</sub> emission band blue shifts in a similar fashion as D<sub>2</sub>, it shifts from 650 nm at 0.5  $\mu\text{W}$  to 630 nm at 700  $\mu\text{W}$ , which is probably the LA peak. The reason for this shift in emission maxima in D<sub>1</sub> and D<sub>2</sub> cannot be due to strain, changes in temperature or the dielectric environment as these would also influence the X<sub>0</sub> emission, which does not show such changes. D<sub>1</sub> emission peak after laser processing or annealing, is approximately 60 meV below the free exciton emission. We attribute this as a new laser activated defect peak, because, trion is about 30 meV below neutral exciton energy level for these materials. Kastl et al., reported that, this neutral exciton and trion separation can be increased up to 60 meV if the free carrier concentration is large enough, [Kastl19] but, we observe this new peak for all flakes, independent of the fluence of Xe<sup>30+</sup> ion irradiation and thereby defect density and most probably free carrier concentration. Also, we observe this new emission at low excitation power after the laser exposure. These results lead us to conclude that, D<sub>1</sub> emission most likely transforms into LA or D<sub>1</sub> is annealed at higher laser excitation power and LA gets activated due to high laser excitation power as reported by He et al. [He16b] Thus far, we were able to observe and laser process the D<sub>1</sub> and D<sub>2</sub> emission, with D<sub>1</sub> emission laser processed to LA emission and D<sub>2</sub> emission transformed to non-radiative defect channels.

Now, the question arises, if these transformations of defect-bound emission properties are persistent. If not, what are the factors that affect these properties?

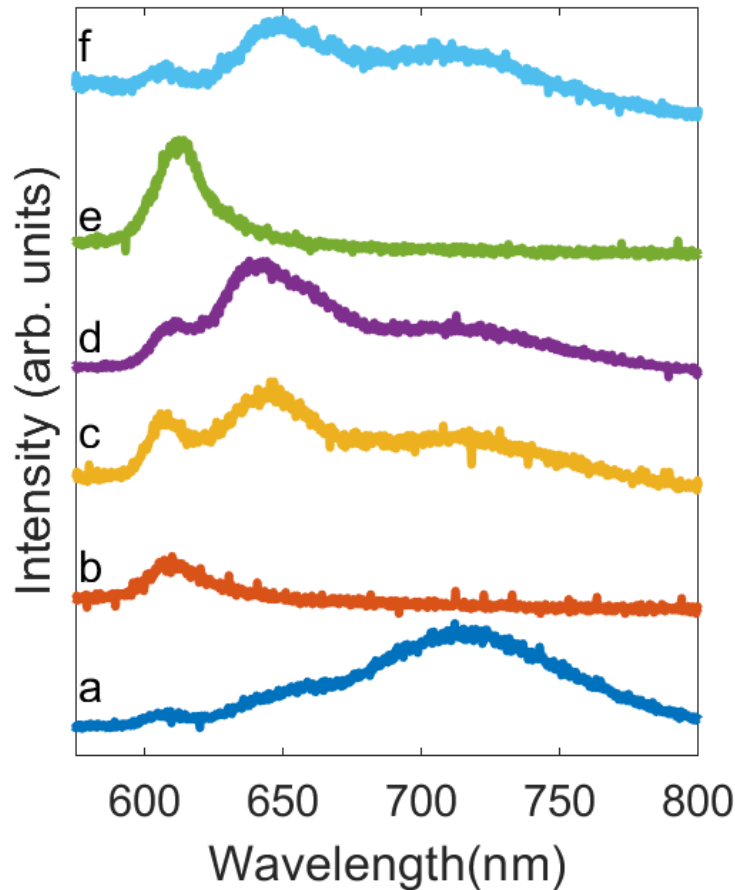


Figure 5.20: PL spectra at 83K with  $0.5\mu\text{W}$  excitation power of sample 2 irradiated with  $1500\mu\text{m}^{-2}$  fluence of  $\text{Xe}^{30+}$  ions at different cycles: a: before laser treatment, b: after laser treatment, c: after one temperature cycle (83K to 295K to 83K still under vacuum), d: after second temperature cycle, e: after second laser treatment, f: after another temperature cycle along with purging of air at room temperature.

Figure 5.20 shows different temperature cycles for one flake irradiated with  $1500\mu\text{m}^{-2}$   $\text{Xe}^{30+}$  ion flux. Starting with the as irradiated sample (curve a), we accomplished a first laser excitation process. The spectrum changes as already described above with only the excitonic contribution together with the "LA"-peak observable (curve b). After this process, the sample was heated up to RT and cooled down afterwards again. Then the third spectrum was recorded (curve c), which showed that  $D_1$  and  $D_2$  are recovering. But the intensity of  $D_1$  is stronger than  $D_2$ . After a second temperature cycle,  $D_1$  and  $D_2$  still increase in intensity, favoring  $D_1$  (curve d). After that second temperature cycle, we performed another laser excitation process, to find out if the laser induced engineering of the luminescence properties is still working. The spectrum after this process (curve e) looked very similar compared to the spectrum after the first excitation process (curve b). At the end, the temperature was raised to RT again and the cryostat was opened, to allow air to come in contact with the sample. Afterwards, the sample was cooled to 83K again and the last spectrum

was recorded (curve f), which showed almost the same features as after the first temperature cycle conducted under vacuum (curve c).

These different temperature cycles lead to the following observations. First, the laser processing is in principal reversible, as it was reported from He et al. for the LA peak. The difference is that the relative strength of  $D_1$  and  $D_2$  is different after the laser processing. Second, bringing the temperature up to RT has a larger influence on the recovery of the PL spectrum, than bringing the sample in contact with air. This leads to the conclusion that for this monolayer flake the laser processing might lead to desorption of physisorbed molecules that most probably bind to defects created via the irradiation of the sample with  $Xe^{30+}$ -ions. By the increase of the temperature up to RT, molecules physisorbed at the surface of the  $WS_2$ -monolayers are getting mobile again and bind to the bare defects, which are still there, because of an energetically favored configuration compared to the bare defects. Keep in mind that the area, which we annealed is only in the order of the focused laser spot. The lower intensity of  $D_2$  compared to  $D_1$  after laser processing and temperature cycle might have its reason in a partial transformation of defects under laser excitation, which was observed e.g. for sulphur vacancies mobilized by electron beam irradiation. These isolated vacancies formed line defects during the e-beam irradiation. For isolated sulphur vacancies an energy barrier of  $\approx 2.3$  eV was calculated for  $MoS_2$  monolayers, which is drastically lowered for neighbouring vacancies to about 0.8 eV. [Komsa13] This hopping barrier might also be overcome by the laser irradiation, leading to a rearrangement of sulfur vacancies assuming that the hopping barrier is of similar energy and the behaviour for  $WS_2$  monolayers.

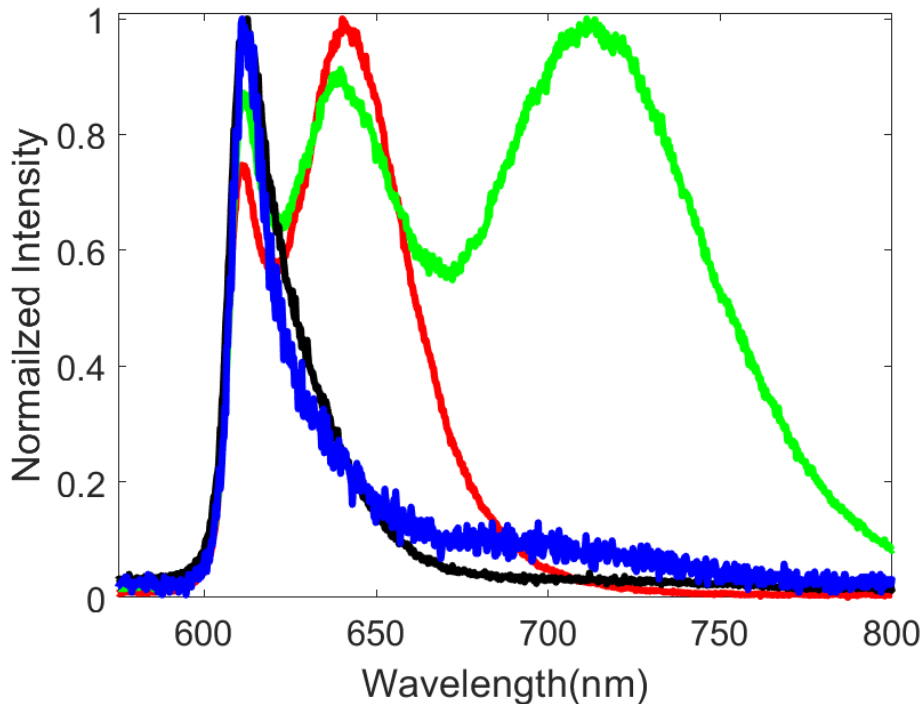


Figure 5.21: PL spectrum at 83K of monolayer  $WS_2$ : pristine as-synthesized (black), pristine aged (green), after low temperature laser processing (blue) and after room temperature laser processing (red).

As mentioned earlier in this section, we also wanted to study the defect-bound emissions re-

lated to aging of the unirradiated WS<sub>2</sub> monolayer. In Figure 5.21, the black curve is the PL at 83K from pristine WS<sub>2</sub> monolayer flake showing none to little defect-bound emission bands, the green curve, however, is the PL at 83K from an aged ( $\approx 8months$ ) unirradiated WS<sub>2</sub> monolayer. Aged unirradiated WS<sub>2</sub> monolayers (aged flake) show similar defect-bound emission bands compared to the flakes irradiated with low fluences of Xe<sup>30+</sup> ions. PL from aged flakes at low temperature (83K) has two emission bands D<sub>1</sub> and D<sub>2</sub>, with D<sub>2</sub> dominating the spectrum at low excitation power. The aged sample could also be laser processed at low temperature, the blue curve is the low temperature laser processed spectrum and it looks very similar to the PL from pristine flake (black curve), with slightly increased emission in the lower energy side, which could be due to LA emission band. Aging of irradiated flakes resulted in a significant reduction in the PL emission properties. Arguments from the temperature cycle, He et al., and Kastl et al., we speculated that D<sub>1</sub> emission band is due to defect complexes and associated adsorbates and D<sub>2</sub> is due to isolated single vacancies such as sulphur vacancy and associated adsorbates. [He16b, Kastl19] To strengthen this argument, we performed room temperature laser annealing. As a result, we should not expect a significant change in the D<sub>1</sub> emission and should expect to see changes in D<sub>2</sub> emission (compared to unexposed flakes) as laser processing might transform the single defects into defect complexes. [Komsa13] The red curve in Figure 5.21 is the spectrum at 83K after the sample was subjected to high power of laser excitation at RT and D<sub>2</sub> emission band is almost absent in this case. Observations from Figure 5.21 strengthens our argument for the origin of both D<sub>1</sub> and D<sub>2</sub> that, D<sub>1</sub> is due to decorated defect complexes and D<sub>2</sub> is due to simpler decorated vacancy defects. Lu et al, in their report, said that, upon irradiation of the WSe<sub>2</sub> flakes with high power 532 nm laser light, chalcogen vacancies get substituted by the atmospheric oxygen. [Lu15] Also, Komsa et al, couldn't distinguish between unoccupied vacancy defects and oxygen substitution in MoS<sub>2</sub>. [Komsa13] From these observations and the literature reports, we think that the origin of D<sub>2</sub> emission bands could also possibly be from oxygen substituted vacancy defects decorated with adsorbates.

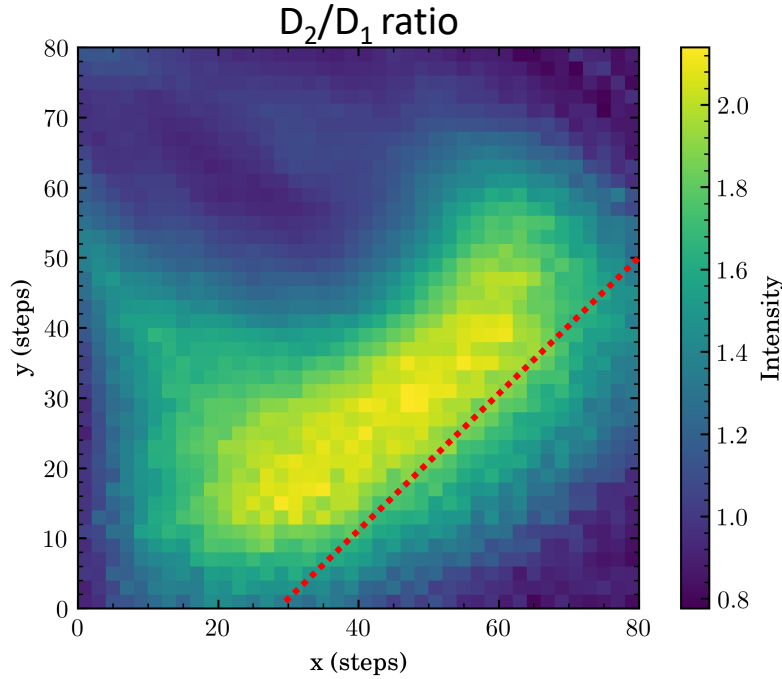


Figure 5.22: PL map of aged pristine monolayer  $\text{WS}_2$  at 83K showing  $D_2/D_1$  ratio across the flake. Dashed red line indicates an approximate edge of the flake.

Kastl et al., reported that single sulphur defects are found more near the edges of the flake. [Kastl19] Low temperature PL map (Figure 5.22) reveals that the  $D_2/D_1$  ratio is much higher closer to the edge than from the middle of the flake for the aged sample. This further supports the argument for the origin of  $D_2$  emission band, that, it is due to decorated single vacancy defects.

## Conclusion

In conclusion, we observe that  $\text{WS}_2$  monolayers grown via CVD process as described in section 5.2 from batch 2 has emission from exciton recombination around 630 nm at room temperature and shifts to higher energy at low temperature. Low temperature spectra of pristine flakes show little to none defect-bound emission.  $\text{Xe}^{30+}$  ions were irradiated onto the sample with different fluences. Flakes irradiated with lower fluences ( $500 \mu\text{m}^{-2}$ ,  $1500 \mu\text{m}^{-2}$  and aged unirradiated flakes) show two defect-bound emission bands ( $D_1$  and  $D_2$ ), with  $D_2$  dominating the low temperature spectrum. Flakes irradiated with higher fluences ( $6000 \mu\text{m}^{-2}$  and  $4500 \mu\text{m}^{-2}$ ) show  $D_1$  dominating the spectrum at low temperature. PL intensity decreases with an increase in  $\text{Xe}^{30+}$  ion fluences as the defect density increases. Both  $D_1$  and  $D_2$  emission bands from  $\text{WS}_2$  monolayers were laser processed at low temperature, with  $D_2$  vanishing completely and  $D_1$  probably transformed to LA emission. These laser processing is reversible, the temperature cycle (LT-RT-LT) results in defect-bound emissions recovery with  $D_1$  recovering faster. These results, along with the published reports from different groups, we conclude that  $D_1$  emission is due to defect complexes with associated adsorbates and  $D_2$  is due to isolated single defects with adsorbates, where, these isolated single defects can be transformed to defect complexes with high power laser irradiation.

## 5.5 Comparison between batch 1 and 2

In this concluding section, differences in the PL emission behaviour between WS<sub>2</sub> monolayer from batch 1 and batch 2 have been discussed. Starting with the similarities, both sets of batches of flakes were synthesized using the same technique described in section 5.2. Both show a narrow exciton emission band around 630 nm and do not show any defect-bound emission bands at room temperature. PL emission maxima shifts to the lower wavelength when the temperature was lowered ( $\approx 610$  nm at 83K). Pristine flakes from batch 1 showed one defect-bound emission (D<sub>0</sub>) at 660 nm, whereas, pristine flakes from batch 2 showed no defect-bound emission peaks albeit, they were both grown via the same synthetic technique. Upon creation of defects via Xe<sup>30+</sup> ion irradiation at different fluences on flakes from both batch 1 and batch 2, flakes from batch 1 still had the similar defect-bound emission D<sub>0</sub>, regardless of the fluence. Flakes from batch 2 showed two defect-bound emissions (D<sub>1</sub> and D<sub>2</sub>) at 650 nm and 720 nm respectively for lower fluences and predominant D<sub>1</sub> at higher fluences. Defect bound emissions from the flakes from both batches were able to be laser processed at low temperatures. D<sub>0</sub> emission band of WS<sub>2</sub> monolayers have been laser processed to LA from batch 1, D<sub>1</sub> emission band to LA from batch 2, but, D<sub>0</sub> recovered when the laser power was lowered again, which is not the case for D<sub>1</sub>. There was no D<sub>2</sub> for flakes from batch 1, D<sub>2</sub> from batch 2 has vanished completely after laser processing. From these results, along with the temperature cycle measurements and the literature, we were able to identify the origin of D<sub>2</sub>. We attribute the origin of D<sub>2</sub> emission band to single vacancies decorated with adsorbates and oxygen-related substitutions (along with adsorbates). The origin of D<sub>0</sub> and D<sub>1</sub> emission bands are tentatively attributed to defect complexes along with adsorbates, but the exact origin is still unsolved. The main conclusion that we want to emphasise in this section is, even though both batches of flakes were produced via the same technique, the nature of defects responsible for the defect-bound emissions is somehow "encoded" during the synthesis. Slight differences that are unable for us to observe during the synthesis has a profound influence on the kind of defects it will possess. Therefore, it is still necessary to optimize the synthesis in order to achieve the potential this class of material promises. The defect-bound emissions from samples from both batches can be altered/engineered via exposure to higher laser power and also reversibly with temperature cycles.

## **Part IV**

# **Crystalline BODIPY semiconductor rods**

# Chapter 6

## Spectroscopic characterisation of BODIPY crystalline rods

This chapter is mostly based on the work done by us that had been published in the Journal Of Physical Chemistry C with the inclusion of data from extended work. [Asaithambi19]

### 6.1 Motivation

BODIPY dyes are a class of optically active organic compounds, based on a 4,4-difluoro-4-bora-3a,4a-diaza-s-indacene (or boron-dipyrrromethene) core. [Burghart99, Okada16] Because of their high fluorescence quantum yield and tunable emission wavelength, they have found a wide range of applications, e.g. as fluorescent labels, chemical sensing, or laser dyes. [Ehrenschwender11, Mon-sma89, Shah90] They exhibit long-term stability and are compatible with polymer technologies, which makes them attractive for use in solar cell concentrators and organic light-emitting devices. [Altan Bozdemir11, Tang87] Variations to their structure make it possible to tune their optical properties and solubility. [Xiao07] For technical applications, the solid form of BODIPY is more desirable than its solution. [Altan Bozdemir11] In the solid form, however, interaction among the molecules, such as J or H aggregation (amorphous aggregation of molecules), may lead to blue- or red-shifted emission. Aggregation can even lead to a complete quench of the fluorescence. [Kim17] One strategy to overcome this problem is the introduction of a suitable group at the meso position to prevent aggregation through steric hindrance. [Ozdemir09] In this chapter, we investigate the optical properties of micro-crystals of the BODIPY derivative shown in Figure 6.1a.

### 6.2 Sample synthesis and fabrication

The synthesis of the samples had been carried out by our collaborators Prof. Yamamoto's group in Tsukuba University, Japan. The synthesis is described briefly in the following: A 5 mM solution of BODIPY in tetrahydrofuran (THF) is injected into water with Cetrimonium bromide (CTAB) as a surfactant, and the mixture is sonicated for 5 min. Allowing the solution to settle overnight leads to the formation of micrometer-size rods with crystalline habit (see Figure 6.1b). Note that the presence of the surfactant improves crystal growth, however, it does not affect the optical

properties of the resulting micro-rods, discussed below. Also, THF can be replaced by acetone or ethanol without changing the results. [Asaithambi19] All these rods are stable in water and were drop cast on either quartz or Si/SiO<sub>2</sub> substrate for further optical studies.

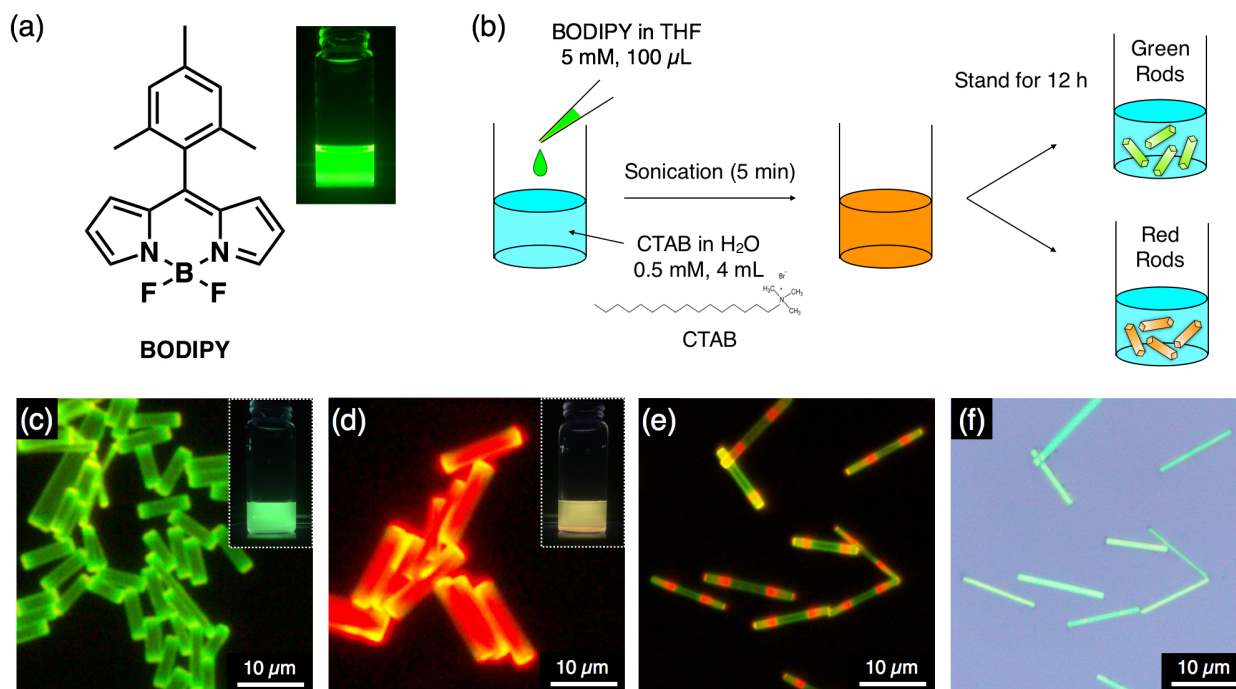


Figure 6.1: (a) Molecular structure of BODIPY and its fluorescence in THF solution (excitation wavelength  $\lambda_{ex} = 365$  nm) [Kee05]. (b) Schematic representation of the preparation procedures of green and red rods of BODIPY. (c, d) Fluorescence microscope images of green (c) and red (d) BODIPY rods,  $\lambda_{ex} = 400 - 450$  nm. The bright spots at the end of the rods indicate light guidance by total internal reflection and demonstrate the high optical quality of the micro-crystals. The insets in (c) and (d) show the appearance of the micro-crystals in solution under UV illumination. (e, f) Fluorescence (e) and optical (f) microscope images of BODIPY rods with optical heterostructure,  $\lambda_{ex} = 400 - 450$  nm. All the images were taken in Prof. Yamamoto's group in Japan.

## 6.3 Results and discussion

Figure 6.1c and 6.1d show fluorescence microscopy images of typical micro-rods, fabricated as described in the previous section. Under near-ultraviolet illumination (400 – 450 nm wavelength), most rods exhibit bright green emission similar to the monomer solution in THF shown in the inset of Figure 6.1a. Besides the green emitting rods, rods with emission ranging from green all the way to red (see Figure 6.1d) have also been found. Using the described fabrication method, the resulting color of the rods is not well defined; we observe micro-crystals with different emission in different batches (see Figure 6.1c and 6.1d) and even single rods with discrete, differently colored sections, see Figure 6.1e. The PL quantum yields of green and red emitting rods were determined to be 0.12 and 0.10 respectively.

Spies et al. have found similar observations on different BODIPY derivative. They were able to obtain different crystal habits depending on the details of the crystallization process. They found that different crystal habits exhibit different emission colours. Interestingly, all the crystal habits showed the same short range order in the crystalline structure and concluded that long range order is crucial in determining the emission properties of the crystals. [Spies13] We propose that the difference in the emission properties of crystals grown with our BODIPY derivative have a similar origin. Though this study is focused on a specific compound, the results are more general.

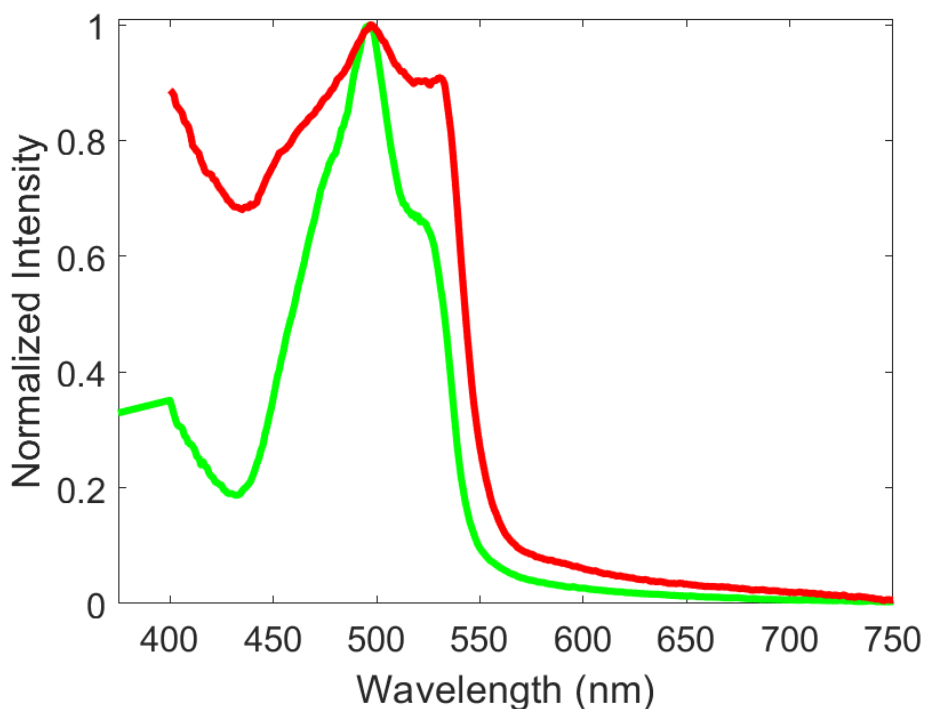


Figure 6.2: Diffuse reflectance spectra (DRS) from single green emitting BODIPY rod (in green) and red emitting BODIPY rod (in red).

Green, red and striped rods, independent of their fluorescence emission, the rods appear green in color under an optical microscope, illuminated with white LED (see Figure 6.1f). Diffuse reflectance spectrum from a single rod gives out an approximate absorbance curve. Figure 6.2 shows the diffuse reflectance spectra from a green rod (in green) and red rod (in red), this experiment concludes that there is little to no difference in the absorption between green and red rod.

To better understand the emission properties of these rods, we performed micro photoluminescence ( $\mu$ -PL) spectroscopy on single rods. PL spectra under 405 nm laser light excitation for “green” and “red” rods are shown in Figure 6.3a and 6.3b, respectively. The “green” rod exhibits a strong emission band around 550 nm, while the “red” rod has emission band above 650 nm. Note, however, that both rods show light emission over the entire spectral range between 525 nm and 800 nm. The distinct, short wavelength cut-off at 525 nm in both spectra (referred as "Max E") agrees well with the absorption edge of the BODIPY monomer in solution, shown in the inset of Figure 6.3a.

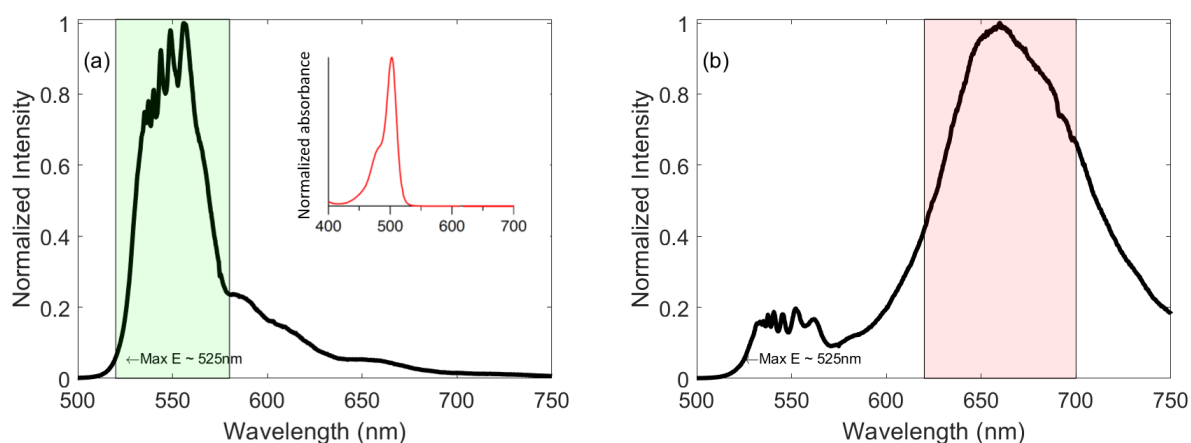


Figure 6.3: PL spectrum of (a) green emitting and (b) red emitting BODIPY rods at 296 K. The inset in (a) shows the absorption spectrum of the BODIPY monomer in solution.

The presence of multiple emission bands indicate that there are different species present in the rods, which emit in different spectral regions (green, orange, or red mainly). The colors that appear in the fluorescence microscopy images are the result of different amounts of the respective species in each rod. Even rods that do not have as well-separated phases as the ones in Figure 6.1e but seem macroscopically homogeneous are composed of domains with different emission properties.

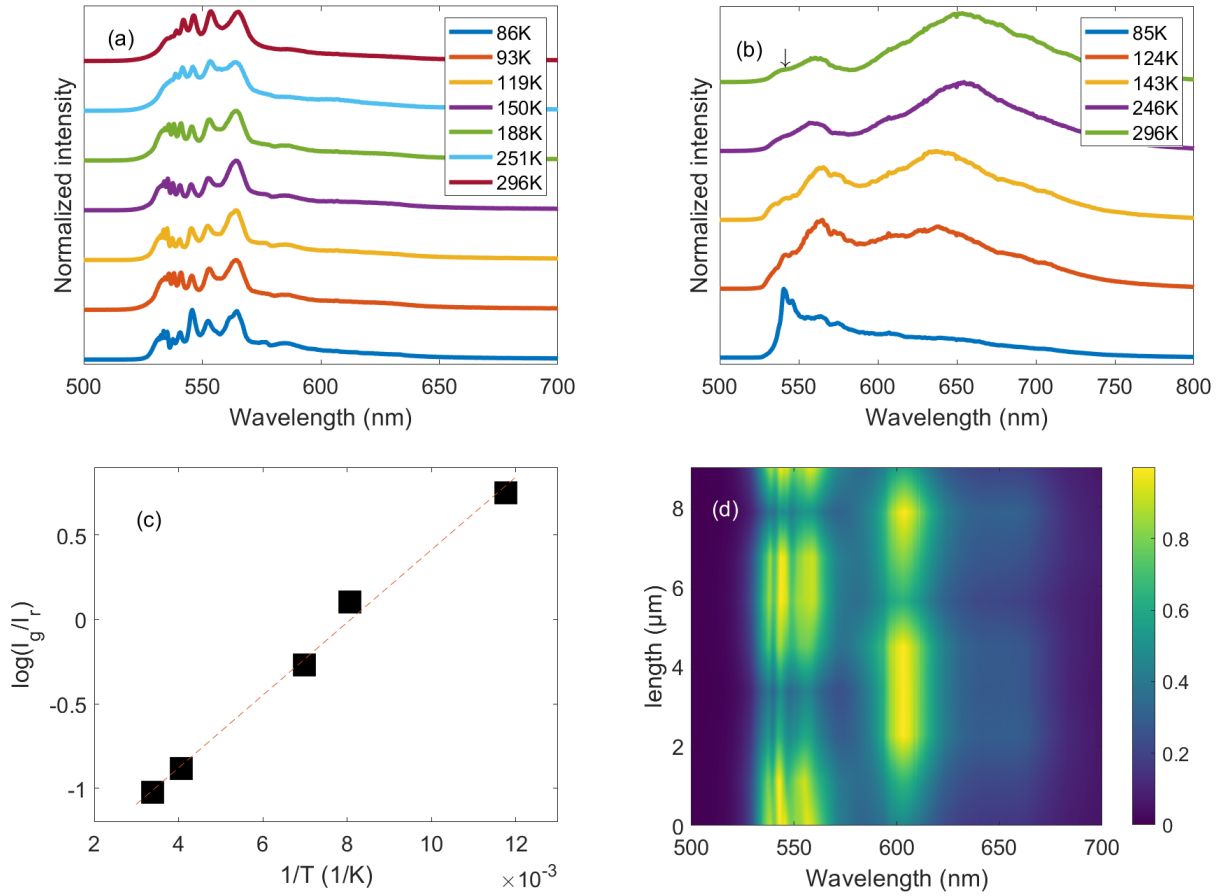


Figure 6.4: (a) PL spectra of green emitting BODIPY rod at different temperatures (b) PL spectra of a red-emitting BODIPY rod at different temperatures. (c) Arrhenius plot of the ratio between green and red intensities at different temperatures. (d) Room temperature line scan along a single, striped BODIPY rod.

This assumption is supported by temperature-dependent PL spectroscopy on a single rod. Figure 6.4b shows how the PL of a “red” rod evolves, as the temperature ( $T$ ) is lowered from 296 K to 85 K. With decreasing  $T$ , the emission in the red (around 650 nm) decreases, while at the same time, the green part of the spectrum increases in intensity. Note that the individual peaks in the spectrum do not shift but rather change their relative intensities. As an example, the dominant peak in the low-temperature spectrum is indicated by an arrow in the high-temperature data. PL measurements of “green” rods, on the other hand, do not show such a pronounced temperature-dependent change in the spectral weights, see Figure 6.4a. Furthermore, at low-temperatures, the PL spectra of “green” and “red” rods become quite similar. Figure 6.4c quantifies the thermally induced diffusion by an Arrhenius-plot of the ratio of the green (560 nm) and red (650 nm) emission intensities. The fit (red line) using equation 6.1, where  $I_g$  and  $I_r$  are the intensities of green (560 nm) and red (650 nm) contribution,  $I_0$  is the initial intensity and  $k$  is the Boltzman constant, gives an activation energy  $E_a$  of 18 meV.

$$\log\left(\frac{I_g}{I_r}\right) = \log(I_0) - \frac{E_a}{kT} \quad (6.1)$$

We explain these experimental observations using a simple model (see Figure 6.5), based on the fact that the solid form of BODIPY can exist in different crystal modifications. Such polymorphism in BODIPY was first reported by G.-G. Luo et al. [Luo13] In their report, for 4-Methoxycarbonylphenyl-substituted BODIPY, they found several different crystalline polymorphs, which exhibit characteristically different emission properties. In our case, we assume that at least two crystalline polymorphs can be present in a single rod. One of them (labelled BODIPY(g) in the following) has a large HOMO-LUMO separation, characterized by PL emission in the range of 530–580 nm, similar to that of the BODIPY monomer, but somewhat red-shifted because of its crystalline order. The other modification, BODIPY(r) exhibits a reduced HOMO-LUMO energy difference, hence, emission in the red spectral range, possibly caused by the coupling of molecular orbitals among neighboring molecules. Figure 6.5 schematically depicts the resulting energy landscape, when a small amount of BODIPY(r) is embedded in BODIPY(g).

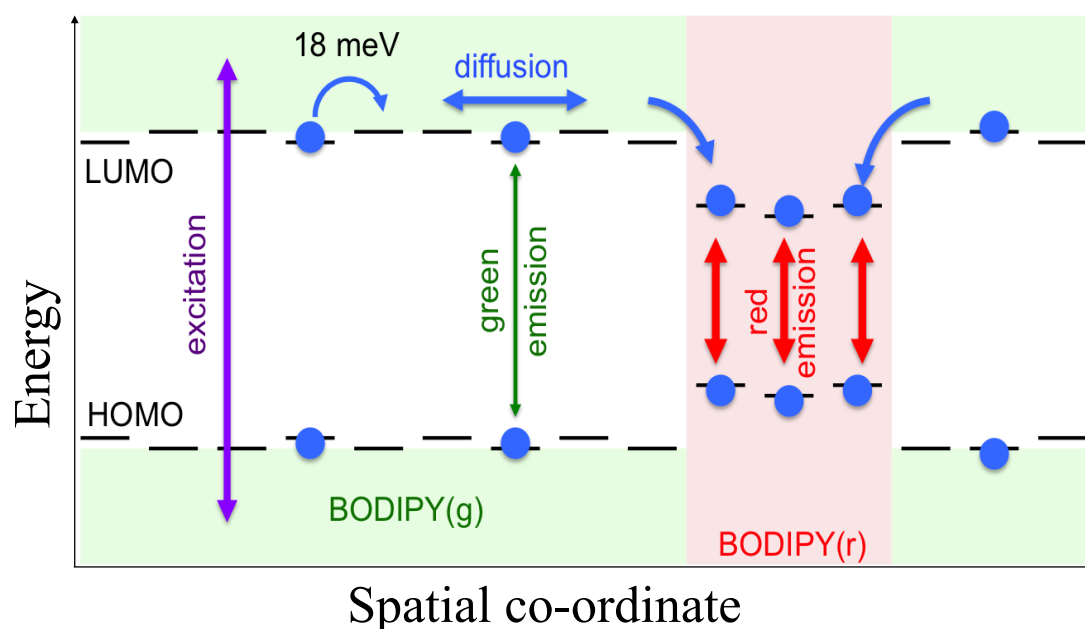


Figure 6.5: Model showing the energy landscape in real space of a single rod that describes the hopping and recombination of excited charge carriers in different regions (BODIPY(g) and BODIPY(r)).

At room temperature, electron-hole pairs that are optically excited in BODIPY(g) can diffuse to the regions with BODIPY(r), where they recombine by the emission of red light. Therefore, even in rods that predominantly consist of BODIPY(g), the PL emission will appear as red. This somewhat resembles the processes in inorganic semiconductor heterostructures, such as GaAs/AlGaAs quantum wells, where also the PL emission will be dominated by recombination in the low-bandgap region (GaAs), even when the material is excited in the high-bandgap environment (AlGaAs). [Fox17] Note that, comparing Figure 6.1e and 6.1f, the optical microscopy images do not show a clear stripe pattern, indicating that photoabsorption is almost the same for both BODIPY(g) and BODIPY(r), which supports the model shown in Figure 6.5 and is supported by the diffuse reflectance spectra shown in Figure 6.2.

With decreasing temperature, diffusion of the optically generated carriers will be reduced, and fewer of them will be able to reach the low-energy regions of BODIPY(r) due to the hopping barrier. Therefore, the red emission will decrease in intensity while the green emission will increase (see Figure 6.4b).

Depending on the amount of regions composed of BODIPY(r) the intensity ratio between the green and the red emission band will vary along a single well-shaped rod, if the ratio between BODIPY(g) and BODIPY(r) is changing. This was indeed observed for line scans of the emission at RT along single, striped rods (see Figure 6.4d). That corroborates the model given above that small regions (presumably below 1  $\mu\text{m}$ ) of BODIPY(r) are incorporated in BODIPY(g).

Following experiment was performed by Dr. Saeki in Japan to understand the conductivity of these BODIPY rods. Flash-photolysis time-resolved microwave conductivity (FP-TRMC) experiments clearly show the difference of photogenerated charge carrier half-life ( $\tau_{1/2}$ ) and  $\phi\Sigma\mu$  (the product of the photon-to-carrier conversion efficiency and the sum of charge carrier mobilities) between BODIPY(g) and BODIPY(r) (Figure 6.6a). [Saeki11] The  $\tau_{1/2}$  values of BODIPY(g) is  $7.7 \times 10^{-5}$  s, which is roughly 2 orders of magnitude longer than that of BODIPY(r) ( $8.9 \times 10^{-7}$  s, (Figure 6.6b). Furthermore,  $\phi\Sigma\mu$  of BODIPY(g) ( $2.8 \times 10^{-4} \text{ cm}^2 \text{ V}^{-1} \text{ s}^{-1}$ ) is 5-fold greater than that of BODIPY(r) ( $5.5 \times 10^{-5} \text{ cm}^2 \text{ V}^{-1} \text{ s}^{-1}$ , Figure 6.6c). These results supports the assumption that micro-crystals of BODIPY(r) have many narrow bandgap sites, which trap photocarriers efficiently after the laser flash, leading to shorter  $\tau_{1/2}$  and smaller  $\phi\Sigma\mu$  in comparison with almost trap-free BODIPY(g) micro-rods. Taking  $\phi\Sigma\mu \approx 3 \times 10^{-4} \text{ cm}^2 \text{ V}^{-1} \text{ s}^{-1}$  as a lower limit for the carrier mobility and using the Einstein-relation, [Islam04] we can estimate the diffusion constant in the green rods,  $D \approx 8 \times 10^{-10} \text{ m}^2 \text{ s}^{-1}$ . Together with the measured carrier lifetime  $\tau_{1/2} \approx 10^{-4}$  s this gives a rough estimate of around 1  $\mu\text{m}$  for the diffusion length. Therefore, diffusion of photoexcited carriers can cover large areas inside the rods until they encounter a recombination site, as depicted in Figure 6.5.

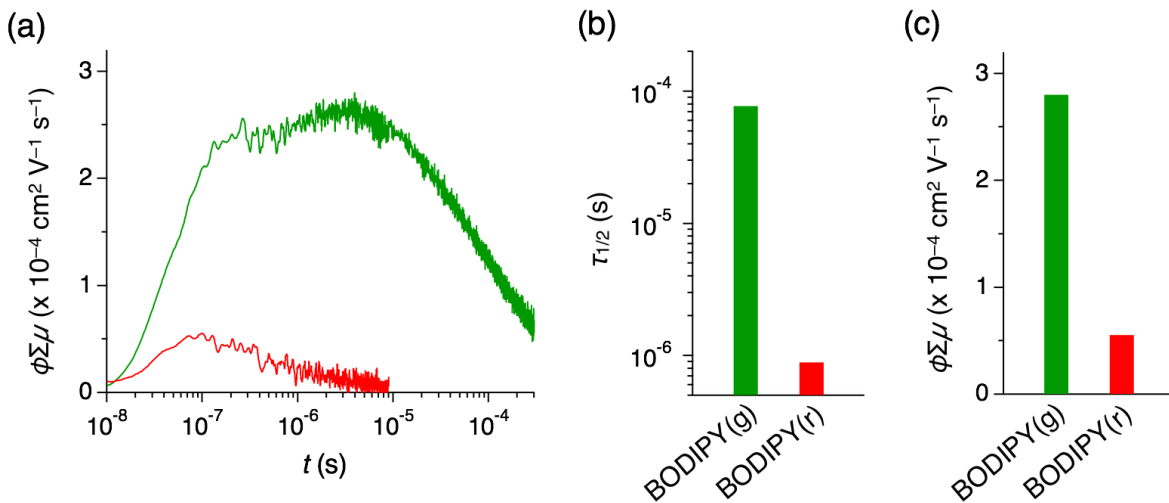


Figure 6.6: (a) TRMC profiles at 25 °C of cast films of BODIPY(g) (green) and BODIPY(r) (red) upon laser flash at 355 nm. (b, c) Bar graphs of  $\tau_{1/2}$  (b) and  $\phi\Sigma\mu$ (c) for BODIPY(g) (green) and BODIPY(r) (red).

X-ray diffraction measurements had been performed by our collaborators (Prof. Yamamoto's

group) in Japan. We were able to obtain a single crystal of BODIPY(r) with a dimension of  $0.41 \times 0.058 \times 0.013 \text{ mm}^3$ , which is large enough for single crystal X-ray diffraction (XRD) studies. According to the XRD data, BODIPY(r) forms orthorhombic crystals with space group *Pbca* (see appendix Figure A.11 and Figure A.12). Importantly, the crystal structure hardly changes upon cooling from at 298 K (red PL) to 93 K (green PL) with only less than 1.5% shrinking of the lattice parameter. These results indicate that the change of the PL color upon lowering *T* does not result from the structural phase transition but from the change of the diffusion length of photogenerated charge carriers. The crystal packing of the BODIPY molecules (Figure A.11) is incompatible with J or H aggregation, so that the green and orange emission energies cannot be explained by aggregation-induced, bathochromic or hypsochromic shifts with respect to the monomer. Unfortunately, single crystal of BODIPY(g), large enough for XRD, has not been obtained. However, the powder XRD pattern of BODIPY(g) is almost identical to that of BODIPY(r) (Figure A.13). Small differences in the relative intensities of the peaks and additional structure at low scattering angles ( $<10^\circ$ ) may indicate, however, different long-range order in BODIPY(g) and BODIPY(r).

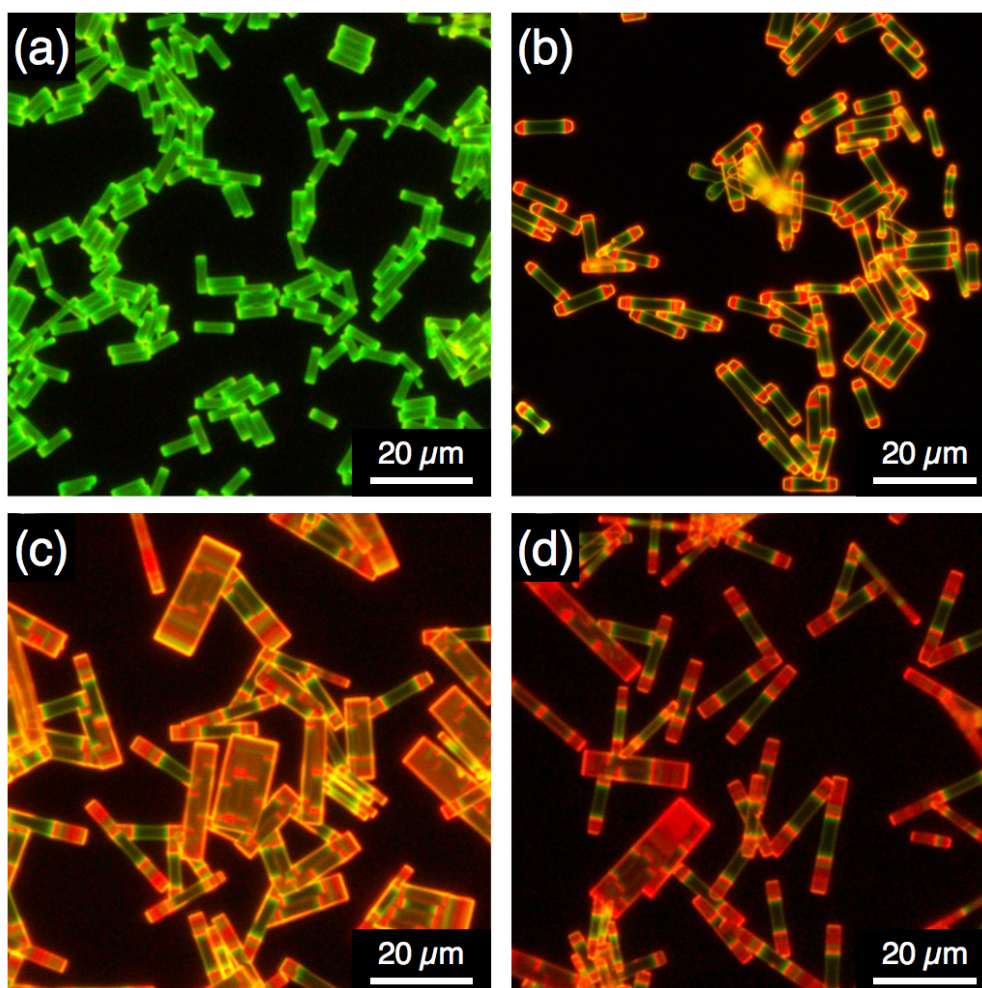


Figure 6.7: Fluorescence micrograph of initially green BODIPY rods, before (a) and after exposure to EtOH vapor for 12 (b), 24 (c) and 36 hours (d).

The co-existence of two crystal phases with different optical properties has recently also been observed in the solution-mediated growth of GaAs nanowires. [Spirkoska09] While GaAs will generally crystallize in the zincblende structure, the high liquid supersaturation present in the growth of gold-catalyzed GaAs nanowires can lead to the formation of wurtzite GaAs. [Spirkoska09, Glas07, Joyce10] This follows the Ostwald step rule, [Santen84] which states that rapid crystallization from a solution takes place so that a thermo-dynamically unstable phase occurs first, which then, in a second step, will recrystallize into a more stable phase. We believe that a similar mechanism is at work in the present compound, with BODIPY(g) being the less stable modification and BODIPY(r) the more stable one. Indeed, we find that rapid growth will preferentially result in green emitting rods, while slow growth will lead to more red emitting crystals. Also, green emitting rods that are exposed to ethanol vapor for extended periods (12–36h of solvent annealing) [Sinturel13] will slowly convert to red-emitting ones (Figure 6.7a-d).

While this demonstrates some degree of control over the emission properties of the rods, (BODIPY(g) vs. BODIPY(r)), it would be highly desirable to find growth conditions, which enable a precise control over the stepwise variation in the HOMO-LUMO gap (similar to the serendipitously created, striped crystals in Figure 1e and f). This would open up the possibility to tailor the energy landscape in a similar fashion as the “bandstructure engineering” in inorganic binary and ternary semiconductor compounds. [Fox17]

## 6.4 Conclusion

In summary, micrometer-sized crystalline rods of BODIPY were grown from solution. Fluorescence microscopy images and photoluminescence spectra show different forms of BODIPY, emitting in the green, orange, and red spectral region. From temperature-dependent photoluminescence, it is concluded that BODIPY crystals can exhibit different HOMO-LUMO gaps, and optically excited carriers can diffuse from the wide-gap to the narrow-gap region with a typical hopping barrier of  $\approx 18$  meV. This model is supported by PL line scans along striped rods and by FP-TRMC. Different growth rates and solvent annealing suggest that the orange-red-emitting crystal structure is the thermodynamically more stable form of BODIPY. These findings may lead to optically active BODIPY heterostructures, similar to those used in inorganic semiconductor technology.

# Chapter 7

## Rydberg like states in BODIPY rods

### 7.1 Motivation

This chapter is an extension of the work from the previous chapter. Semiconducting organic solids have always produced intriguing new physics different from inorganic semiconductors. In the previous chapter, spectroscopic characterization of the BODIPY micro-rod crystals were explained and we concluded that there is a coexistence of multiple crystalline phases within a single rod with interesting photo-physical properties. We observed another intriguing emission characteristic from these BODIPY rods (green rods specifically). On top of a broad luminescence (see Figure 6.3a and 6.3b), we observed a set of peaks with interesting energy spacing between them, detailed analysis of those sets of peaks are reported in this chapter.

### 7.2 Results and discussion

PL spectra of most as-synthesised green BODIPY rods (Figure 6.3a) and some red BODIPY rods (Figure 6.3b), show, besides a broad luminescence, a set of peaks superimposed on that broad luminescence in the green spectral range. Figure 7.1 is a typical example of such a spectrum. Most of these BODIPY rods are tens of micrometers in length, 2-5 micrometers in width and height around one micrometer. One of the idea was that these sets of peaks are due to etalon effect i.e. the formation of standing waves across the length, width or height of the rod resulting in a set of peaks in the spectrum. Unequal spacing of the peaks as a function of the energy rules out this effect.

The solution to 1-D potential well results in equation 7.1 shown below where "n" is the energy level, " $\hbar$ " is the Planck's constant, "m" is the mass of the particle and "a" is the size of the particle. Formation of quantum well like structure within the rod might result in the peaks following equation 7.1, except, the energy scale is in the opposite and hence confinement effect is ruled out.

$$E_n = \frac{n^2 \pi^2 \hbar^2}{2ma^2} \quad (7.1)$$

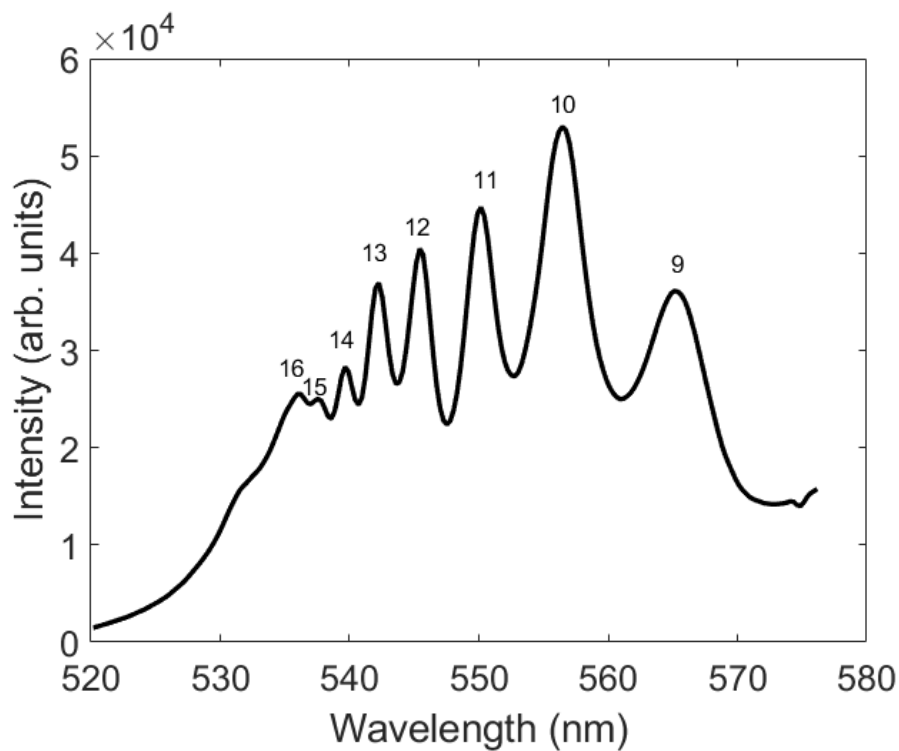


Figure 7.1: PL spectrum of green emitting BODIPY rod at RT with a set of peaks corresponding to principal quantum number  $n$  ranging from 9-16.

Surprisingly, these sets of peaks with their respective energies, follow a  $1/n^2$  rule. In Figure 7.1, each of the peaks is marked with a natural number  $n$ , from 9 to 16. Inverse square of these numbers with the energies of those peaks satisfies the equation 7.2, known as Wannier-Mott exciton equation, where  $E_n$  is the energy corresponding to the level,  $E_g$  is the bandgap and  $E_0$  is an effective Rydberg energy.

$$E_n = E_g - \frac{E_0}{n^2} \quad (7.2)$$

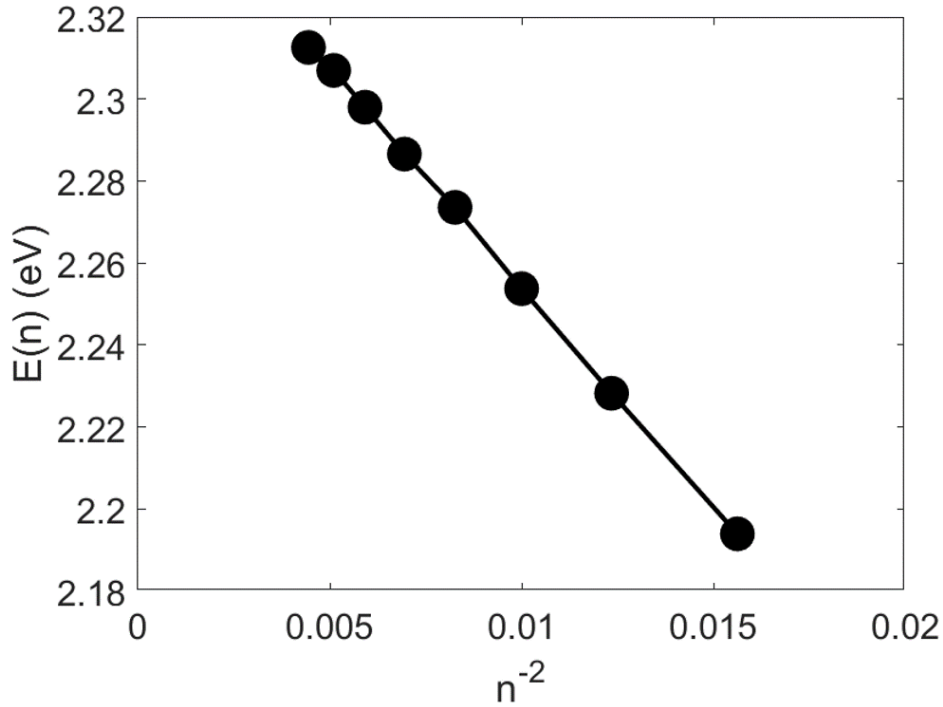


Figure 7.2: Linear fit of peak energy  $E(n)$  against  $n^{-2}$ .

Figure 7.2 shows the evaluation of the sets of peaks against the inverse square of the natural number shown in the Figure 7.1. We observe a near perfect linear fit in this curve. Such behaviour is known from Rydberg atoms such as hydrogen, and Wannier excitons. Note that, the principal quantum number in our case is as large as 16, making it a giant exciton. In fact, Kazimierczuk et al., observed such giant Rydberg excitation, where they were able to probe  $n$  up to 25 via transmission spectroscopy in cuprous oxide. [Kazimierczuk14]

Evaluation of the peak positions within the Wannier exciton model returns  $E_g$  and  $E_0$ .  $E_g$  and  $E_0$  from Figure 7.2 are around 2.35 eV and 20 eV respectively. This is puzzling because, the Rydberg energy from a hydrogen atom is 13.6 eV, which is 7 eV less than what we observe.  $E_g$ , on the other hand, matches well with the absorption edge of these rods. Evaluating the ground state  $n = 1$  in this case, suggests that, the first level is buried deep in the valence band or even below.

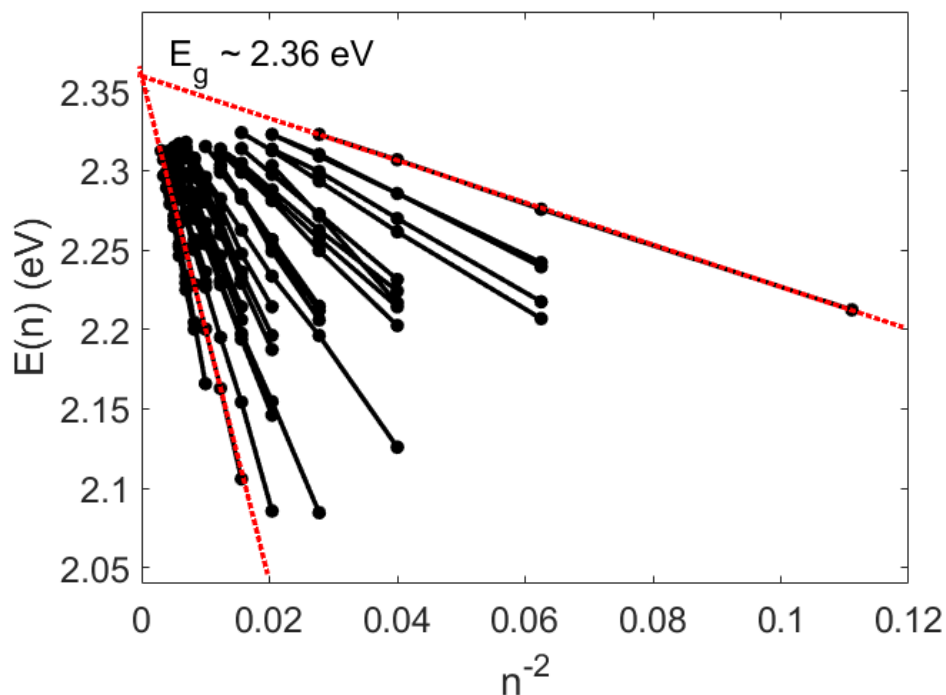


Figure 7.3: Linear fit of peak energy  $E(n)$  against  $n^{-2}$  from 32 different BODIPY rods.

To verify if the effective Rydberg model can be applied to the spectra of other BODIPY rods, we looked at 32 different BODIPY rods which show such emission characteristics and evaluated those peaks by fitting them with equation 7.2 (shown in Figure 7.3). The most consistent part from the fit is the y-intercept, which is  $E_g$  from equation 7.2. Curves from the 32 different BODIPY rods can be extrapolated to almost a single point on the y-axis, which corresponds to the value of  $\approx 2.36$  eV which is the bandgap of the material (see absorption and emission edges in Figure 6.3). But, we observe different slopes ( $E_0$  or effective Rydberg energy) for different rods.

Figure 7.4 shows the different  $E_0$  or effective Rydberg energy values from each BODIPY rod, sorted in ascending order.  $E_0$  ranges from less than 1 eV up to 23 eV. An effective Rydberg energy of a hydrogen-like system follows the equation 7.3, to understand this change in the  $E_0$  value, we investigate the various parameters that could potentially result in this observed change in the  $E_0$  value.

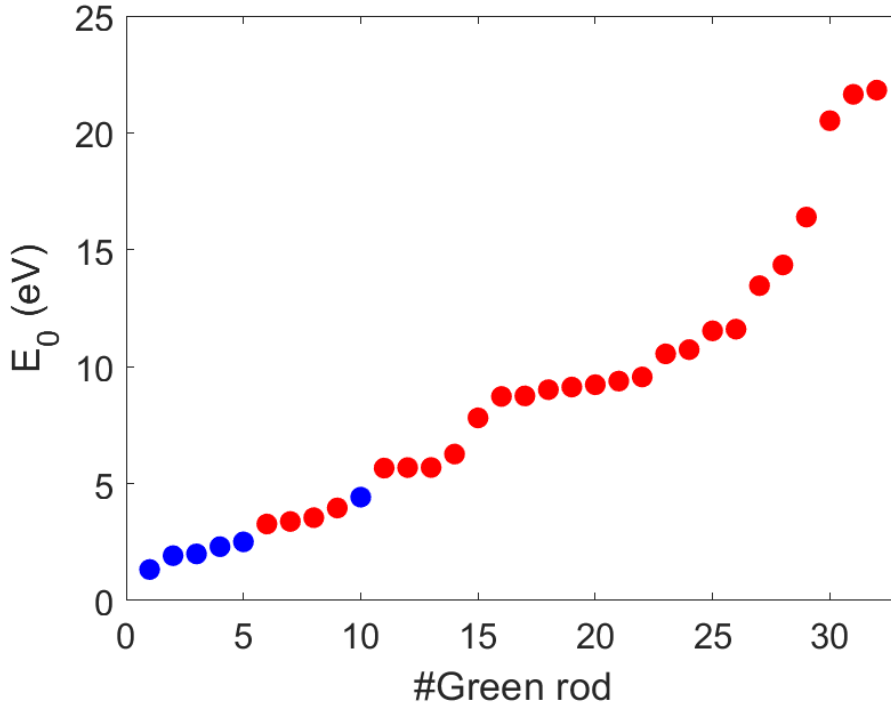


Figure 7.4: Range of  $E_0$  (effective Rydberg energy) from 32 different BODIPY rods. Blue circles correspond to the  $E_0$  values obtained from BODIPY rods grown without the surfactant. Red circles indicate  $E_0$  values from BODIPY rods where the information about growth with or without the surfactant was not documented.

$$E_0 = \frac{m_{eff}Z^2e^4}{8\epsilon_{eff}^2\hbar^2} \quad (7.3)$$

As equation 7.3 shows,  $E_0$  depends on the effective mass of the charge carriers ( $m_{eff}$ ), square of the number of charge ( $Z$ ), fourth power of the elementary charge ( $e$ ) and inverse square of the effective dielectric constant ( $\epsilon_{eff}$ ). We do not have any information about the  $m_{eff}$  and  $\epsilon_{eff}$  of the material and assuming that these are indeed constant. We should observe clusters of  $E_0$  values or steps in Figure 7.4. None of these parameters seem to have any correlation.

There is one interesting observation though, in the previous chapter 6, it is mentioned that green rods can be grown with and without the use of a surfactant (CTAB in this case). Presence of the surfactant seems to affect the optical properties of the grown rods. Blue dots in Figure 7.4 corresponds to the  $E_0$  from BODIPY rods grown without CTAB and it can clearly be seen that, rods grown without CTAB (blue circles in Figure 7.4) show lower  $E_0$  values. Now, this is clear evidence for the influence of the surfactant on such Rydberg like emissions, but how, is still unknown.

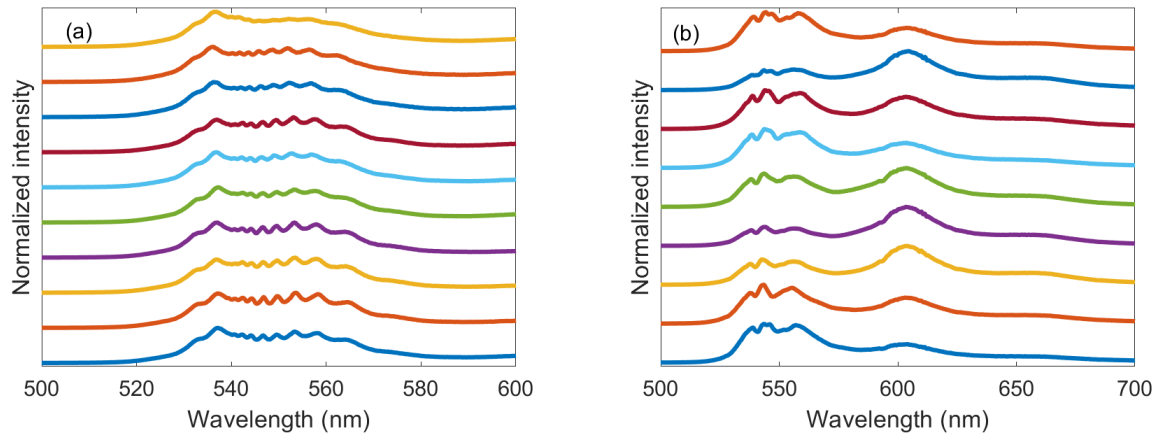


Figure 7.5: PL line scan along a single (a) green emitting BODIPY rod and (b) striped BODIPY rod.

With  $E_0$  being different for each rod, we wanted to know if the same is true for within a single rod, because, they show polymorphism and are poly-crystalline in nature. Figure 7.5a and 7.5b show a PL line scan from a green rod and a striped rod that show this Rydberg like emissions respectively. In both cases, the peak positions regarding the Rydberg like emissions remain the same within a single rod with only the relative amplitudes differing.

With the limited experiments that we have, we propose a possible model that, every rod that shows this property have this Rydberg recombination center embedded within a single rod and this recombination center is different for each rod. We explain these results and the possible origin for such recombination centers using Wannier exciton model. The states have been probed in the PL excitation spectroscopy of  $\text{MoS}_2$ ,  $\text{WS}_2$  [Hill15] and giant Rydberg states in  $\text{Cu}_2\text{O}$  via transmission spectroscopy. [Kazimierczuk14] Given the unusually large Rydberg energies or  $E_0$  values, it could be a deep center in the material due to charges residing in the vicinity.

## 7.3 Conclusion

BODIPY rods, in particular, the green rods, show besides a broad luminescence, a set of peaks with energies that follow a  $1/n^2$  rule and such behaviour is known from Rydberg atoms and Wannier excitons. Emissions from these principal quantum levels can be as large as 16 and as low as 3. Levels with principal quantum numbers 1 and 2 were never observed.  $E$  vs  $n^{-2}$  evaluation with equation 7.2 returns consistent  $E_g$  value of  $\approx 2.36$  eV which corresponds to the bandgap of the material, but, different  $E_0$  for each rod and similar  $E_0$  value within a single rod. Thus, the Rydberg model seems to be appropriate to phenomenologically explain the resonance peaks found in many BODIPY rods.

However, many important questions are left unanswered in this chapter; some of which are listed below:

1. What is the origin of these Rydberg-like states?
2. Why do we observe emission from Rydberg-like states with such high principal quantum numbers (up to  $n = 16$ )?
3. Why is there only one kind of Rydberg-like states in a single rod?
4. Why do we observe different  $E_0$  for different rods?

**Part V**  
**Summary and Outlook**

# Chapter 8

## Summary and Outlook

The summary of this thesis can be broadly divided into three parts based on the material under study, which are silicon nano-particles, WS<sub>2</sub> monolayers, and semiconducting crystalline BOD-IPY micro-rods.  $\mu$ -Photoluminescence spectroscopy was the main technique used for studying the optical properties of these systems. The theory and technique are discussed in part I which includes chapters 1 and 2.

In part II, which includes chapters 3 and 4, spectroscopic studies on silicon nano-particles were discussed. These silicon nano-particles (SiNPs) were synthesised via a large scale gas phase plasma assisted technique and were capped with fluorine forming a shell around the nano-particle in the group of Prof. Kortshagen, USA. Silicon nano-particles studied in this thesis have sizes around 3 nm which corresponds to a bandgap of 1.8 eV. Due to the indirect bandgap nature, PL lifetime in these nano-particles is relatively longer ( $\approx 100 \mu\text{s}$ ) compared to CdSe ( $\approx 10 \text{ ns}$ ). In chapter 3 of this thesis, the interaction of metals such as gold and silver with the silicon nano-particles had been discussed via both spectral and temporal PL spectroscopy studies. The objective for the use of such metal surfaces was to try to influence the radiative rate of the silicon nano-particles and consequently reduce the PL lifetime. Influence of these metal films is highly distance dependent i.e. distance between the metal film and the silicon nano-particles could either enhance the radiative rate (optimum), enhance the non-radiative rate (at very short distances, luminescence quenching occurs) or have no effect at all (longer distance). Also if the metal surface is rough or smooth affects the PL properties of the fluorophore. An ensemble of silicon nano-particles on a Si/SiO<sub>2</sub> substrate has a PL spectrum with its peak around 660 nm, the same is the case for when they were placed on Ag and a slightly blue shifted peak was observed on Au. PL decay from large agglomerates (fitted with stretched exponential decay function), revealed that particles on Si/SiO<sub>2</sub>, Au and Ag showed PL lifetime value of 122  $\mu\text{s}$ , 117  $\mu\text{s}$  and 114  $\mu\text{s}$  respectively. Only a slight decrease in the PL lifetime was observed since the metal influence is minimum for a large agglomerate. PL decay from small agglomerates, PL lifetime of 54  $\mu\text{s}$  (on Si/SiO<sub>2</sub>), 37  $\mu\text{s}$  (on Au) and 30  $\mu\text{s}$  (on Ag) were obtained. Here, at least 40 % reduction in the PL lifetime was obtained from silicon nano-particles deposited on an Ag surface. Although, a significant reduction in the PL lifetime was observed from Au surface as well, enhancement in the emission rate was not observed (qualitatively). Therefore interaction of the nanoparticles with an Ag surface is optimal (lowest PL lifetime of the nanoparticles on Ag) for enhancing the PL of silicon nano-particles, this paves the way for performing efficient single particle studies.

Single particle spectroscopy studies of silicon nano-particle on Ag surface have been presented

---

in chapter 4 as an extension of the work from chapter 3. The Si/SiO<sub>2</sub> substrate was coated with nano-porous Au and subsequently Ag was evaporated on top of it to provide the required rough Ag surface. A solution of silicon nano-particles was diluted in a mixture of PMMA and CHCl<sub>3</sub> and spin coated on Ag substrate, as dilution and spin coat is important to achieve highly dispersed nanoparticles. Using these elaborately prepared substrates and the diluted NP solution, it was possible to achieve single particle spectroscopy of SiNPs with fluorinated shell. Single particle phenomena such as PL intermittency or PL blinking and spectral jittering at room temperature were observed for single silicon nano-particle. PL intermittency showed longer "off" times and shorter "on" times. Blinking statistics followed a power law behaviour, indicating multiple trap sites and therefore multiple auger recombination rates. The larger surface area of the nanoparticles with more dangling bonds can provide such trap sites. Spectral jittering due to quantum-confined Stark effect was observed at RT. As an outlook, it is important to have better control of the distance between the metal surface and silicon nano-particle. Also with the PMMA matrix, it is hard to achieve homogeneous height across the substrate. To counter these issues, the use of plasma to oxidize Ag in a controlled manner to provide a defined thickness of the oxide layer would provide more control over this experiment. Also, the same experiments have to be repeated with lower integration time and longer time traces to have better statistics for the PL intermittency and the same is true for spectral jittering studies and to study a possible anti-correlation behaviour between energy at emission maxima and full width at half maximum. All these results should then be compared with direct bandgap semiconductors to find the differences.

In part III chapter 5, optical spectroscopy of defect-bound emissions from WS<sub>2</sub> monolayers were studied. WS<sub>2</sub> monolayers were grown via a CVD technique in the group of Dr. Mattevi, UK. WS<sub>2</sub> monolayers are three atoms thin layers and have a direct bandgap (1.9 eV to 2.1 eV depending on the growth) at K point in the momentum space. This makes it very interesting in the field of optoelectronics. Overall, chapter 5 includes PL spectroscopy results from two batches of WS<sub>2</sub> monolayers grown via the same technique. Defect bound emissions from these batches were studied individually and compared with each other.

WS<sub>2</sub> monolayers from batch 1 exhibit a single asymmetric emission band around 630 nm at room temperature. Asymmetry is due to a small contribution from trion emission slightly at lower energy along with neutral exciton emission. Low temperature PL from a pristine WS<sub>2</sub> monolayer shows, besides a blue shifted exciton emission (615 nm), an additional emission band (D<sub>0</sub>) at 660 nm related to intrinsic defects. Xe<sup>30+</sup> ions with different fluences were irradiated (by Dr. Kozubek in the group of Prof. Schleberger) on the WS<sub>2</sub> monolayers to intentionally create and study the influence of defects on the optical properties. The irradiated flakes show a slightly shifted D<sub>0</sub> emission at 670 nm. The defect-bound emission can be changed by laser exposure with higher powers up to 1500 μW. During this laser processing of the monolayers, a new emission band (LA) appears in the spectra. We found a correlation between the density of defects (Xe<sup>30+</sup> ions fluences) and the amplitude of LA emission with respect to the D<sub>0</sub> emission and quantified the laser processing effect with the ratio LA/D<sub>0</sub> as the quantifiable parameter depending on the defect density.

WS<sub>2</sub> monolayers from batch 2 show an emission due to exciton recombination around 630 nm at room temperature and shifts to higher energy at low temperatures. Low temperature spectra of pristine flakes show little to none defect-bound emission. Xe<sup>30+</sup> ions were irradiated on to the sample with different fluences. Flakes irradiated with lower fluences (500 μm<sup>-2</sup>, 1500 μm<sup>-2</sup> and aged unirradiated flakes) show two defect-bound emission bands (D<sub>1</sub> and D<sub>2</sub>), with D<sub>2</sub> dominating

---

the low temperature spectrum. Flakes irradiated with higher fluences ( $6000 \mu\text{m}^{-2}$  and  $4500 \mu\text{m}^{-2}$ ) show  $D_1$  dominating the spectra at low temperature. PL intensity decreases with increasing  $\text{Xe}^{30+}$  ion fluences as the defect density increase with it. The  $\text{WS}_2$  monolayers were also exposed to higher laser powers at LT and both  $D_1$  and  $D_2$  were laser processed at low temperatures. During the laser processing  $D_2$  vanishes completely and  $D_1$  was laser processed to LA emission. This laser processing is reversible. Temperature cycle (LT-RT-LT) results in defect-bound emissions recovery of  $D_1$  and  $D_2$  with  $D_1$  recovering stronger. From these results, along with published reports in the literature, we conclude that,  $D_1$  emission is due to defect complexes with associated adsorbates and  $D_2$  is due to isolated single vacancy defects (which could also be substituted with oxygen) with adsorbates, where, these isolated single defects might be transformed to defect complexes during the high power laser exposure.

The differences and similarities in the PL emission behaviour between  $\text{WS}_2$  monolayer from batch 1 and batch 2 were discussed. Starting with the similarities, both sets or batches of flakes were synthesised using the same technique described in section 5.2. Both show a narrow exciton emission band around 630 nm and do not show any defect-bound emission bands at room temperature. PL emission maxima shifts to the lower wavelength when the temperature was decreased and shifts to  $\approx 610$  nm at 83 K. Pristine flakes from batch 1 showed one defect-bound emission ( $D_0$ ) at 660 nm, whereas, pristine flakes from batch 2 showed no defect-bound emission peaks albeit, they were both grown via the same synthetic technique. Upon creation of defects via  $\text{Xe}^{30+}$  ion irradiation at different fluences on flakes from both batch 1 and batch 2, flakes from batch 1 still had the similar defect-bound emission  $D_0$ , regardless of the fluence, with increased intensity from it at 83K. But, flakes from batch 2 showed two defect-bound emissions ( $D_1$  and  $D_2$ ) at 650 nm and 720 nm respectively for lower fluences and predominant  $D_1$  at higher fluences. Defect bound emissions from the flakes from both the batches were able to be laser processed at low temperatures.  $D_0$  was laser processed to LA from batch 1,  $D_1$  to LA from batch 2, but,  $D_0$  recovered when the laser power was lowered again, which is not the case for  $D_1$ . There was no  $D_2$  for flakes from batch 1,  $D_2$  from batch 2 vanished completely after laser processing. From these results, we were able to identify the origin of  $D_2$ , but, the suggested origin of  $D_0$  and  $D_1$  still lacks clear evidence. The main conclusion that we want to emphasis in this section is, even though both batches of flakes were produced via the same technique, the nature of defects responsible for the defect-bound emissions is somehow "encoded" during the synthesis. Slight differences that are unable for us to observe during the synthesis has a profound influence on the kind of defects it will possess. Therefore, it is necessary still to optimize the synthesis in order to achieve the potential this class of material promises.

As an outlook, the master student, Mr. Marcel Ney in a further collaboration with Prof. Marika Schleberger from the same university has already started doing the experiments to understand the interaction between  $\text{Xe}^{30+}$  ions and the monolayer flakes. The set of experiments are the following: Firstly, characterization of pristine flakes and its defect-bound emissions, followed by irradiation with  $\text{Xe}^{30+}$  ions, again the characterization via temperature and excitation power-dependent PL measurements, etching of the substrate to obtain a free standing flake (irradiated), PL measurements and finally looking at the flakes under transmission electron microscope. This would give us an idea about the interaction of  $\text{Xe}^{30+}$  ions with the flakes.

Part IV of this thesis consists of spectroscopic characterization of organic semiconductor rods in chapter 6 and unexpected emission characteristics in green BODIPY rods in chapter 7.

In chapter 6, micrometer-sized crystalline rods of BODIPY were grown from solution (in col-

---

laboration with Prof. Yamamoto's Group). Fluorescence microscopy images and photoluminescence spectra show different forms of BODIPY, emitting in the green, orange, and red spectral region. From temperature-dependent photoluminescence, it is concluded that BODIPY crystals can exhibit different HOMO-LUMO gaps, and optically excited carriers can diffuse from the wide-gap to the narrow-gap region with a typical hopping barrier of  $\approx 18$  meV. All these findings were explained within a proposed model that, BODIPY rods show polymorphism leading to different optical properties. This model is supported by PL line scans along striped rods and by flash-photolysis time resolved microwave conductivity (FP-TRMC) measurements. Different growth rates and solvent annealing suggest that the orange-red-emitting crystal structure is the thermodynamically more stable form of BODIPY. These findings may lead to optically active BODIPY heterostructures, similar to those used in inorganic semiconductor technology. Chapter 7 is an extension of chapter 6, where, BODIPY rods emitting in the green spectral range, displayed on top of the broad luminescence, a set of peaks, where the energetic peak position followed a  $1/n^2$  rule known from hydrogen atom model or Wannier exciton model. These emission peaks correspond to  $n$  to be as large as 16 and as low as 3. Applying Wannier exciton model (see equation 7.2), returns a common  $E_g$  value of  $\approx 2.36$  eV for all the rods studied, which corresponds to the bandgap (or HOMO-LUMO gap) of the semiconducting BODIPY rods.  $E_0$  or effective Rydberg energy, however, show a wide range of values starting from 1 eV and rises up to 23 eV, which is significantly higher than the Rydberg energy of 13.6 eV from a hydrogen atom. Up to now, there are several questions unanswered, e.g. what is the origin of these peak series. As an outlook, we think, time resolved PL spectroscopy using a streak camera would provide more information in understanding the behaviour. It is known from Rydberg like optical behaviour from He clusters that, these emissions are longer lived.

# Bibliography

- [Alonso18] E. T. Alonso, D. P. Rodrigues, M. Khetani, D.-W. Shin, A. D. Sanctis, H. Joulie, I. de Schrijver, A. Baldycheva, H. Alves, A. I. S. Neves, S. Russo and M. F. Craciun, *Graphene electronic fibres with touch-sensing and light-emitting functionalities for smart textiles*, npj Flexible Electronics **2** (2018).
- [Altan Bozdemir11] O. Altan Bozdemir, S. Erbas-Cakmak, O. O. Ekiz, A. Dana and E. U. Akkaya, *Towards Unimolecular Luminescent Solar Concentrators: Bodipy-Based Dendritic Energy-Transfer Cascade with Panchromatic Absorption and Monochromatized Emission*, Angewandte Chemie International Edition **50**, 10907 (2011).
- [Anderson99] M. L. Anderson, C. A. Morris, R. M. Stroud, C. I. Merzbacher and D. R. Rolison, *Colloidal Gold Aerogels: Preparation, Properties, and Characterization*, Langmuir **15**, 674 (1999).
- [Asaithambi19] A. Asaithambi, D. Okada, G. Prinz, H. Sato, A. Saeki, T. Nakamura, T. Nabeshima, Y. Yamamoto and A. Lorke, *Polychromatic Photoluminescence of Polymorph Boron Dipyrromethene Crystals and Heterostructures*, The Journal of Physical Chemistry C **123**, 5061 (2019).
- [Benami12] A. Benami, A. Lopez-Suarez, L. Rodriguez-Fernandez, A. Crespo-Sosa, J. C. Cheang-Wong, J. A. Reyes-Esqueda and A. Oliver, *Enhancement and quenching of photoluminescence from silicon quantum dots by silver nanoparticles in a totally integrated configuration*, A **2** (2012).
- [Bennett00] C. H. Bennett and D. P. DiVincenzo, *Quantum information and computation*, Nature **404**, 247 (2000).
- [Biteen05] J. S. Biteen, D. Pacifici, N. S. Lewis and H. A. Atwater, *Enhanced Radiative Emission Rate and Quantum Efficiency in Coupled Silicon Nanocrystal-Nanostructured Gold Emitters*, Nano Letters **5**, 1768 (2005).
- [Biteen06] J. S. Biteen, N. S. Lewis, H. A. Atwater, H. Mertens and A. Polman, *Spectral tuning of plasmon-enhanced silicon quantum dot luminescence*, A **88**, 1 (2006).
- [BOND74] G. C. BOND, *Homogeneous and Heterogeneous Catalysis by Noble Metals*, in *Advances in Chemistry*, 25–34, AMERICAN CHEMICAL SOCIETY (1974).

## BIBLIOGRAPHY

---

- [Braam13] D. Braam, A. Mölleken, G. M. Prinz, C. Notthoff, M. Geller and A. Lorke, *Role of the ligand layer for photoluminescence spectral diffusion of CdSe/ZnS nanoparticles*, Physical Review B - Condensed Matter and Materials Physics **88**, 1 (2013).
- [Braam16] D. Braam, *optische eigenschaften photolumineszierender mikro-und nanostrukturen*, Dissertation, Universität Duisburg-Essen (2016).
- [Brus84] L. E. Brus, *Electron-electron and electron-hole interactions in small semiconductor crystallites: The size dependence of the lowest excited electronic state*, The Journal of Chemical Physics **80**, 4403 (1984).
- [Burghart99] A. Burghart, H. Kim, M. B. Welch, L. H. Thoresen, J. Reibenspies, K. Burgess, F. Bergström and L. B.-Å. Johansson, *3,5-Diaryl-4,4-difluoro-4-bora-3a,4a-diaza-s-indacene (BODIPY) Dyes: Synthesis, Spectroscopic, Electrochemical, and Structural Properties*, The Journal of Organic Chemistry **64**, 7813 (1999).
- [Cardona66] M. Cardona and F. H. Pollak, *Energy-Band Structure of Germanium and Silicon: The k·p Method*, Phys. Rev. **142**, 530 (1966).
- [Carozo17] V. Carozo, Y. Wang, K. Fujisawa, B. R. Carvalho, A. McCreary, S. Feng, Z. Lin, C. Zhou, N. Perea-López, A. L. Elías, B. Kabius, V. H. Crespi and M. Terrones, *Optical identification of sulfur vacancies: Bound excitons at the edges of monolayer tungsten disulfide*, Science Advances **3**, e1602813 (2017).
- [Chow15] P. K. Chow, R. B. Jacobs-Gedrim, J. Gao, T.-M. Lu, B. Yu, H. Terrones and N. Koratkar, *Defect-Induced Photoluminescence in Monolayer Semiconducting Transition Metal Dichalcogenides*, ACS Nano **9**, 1520 (2015).
- [Delerue93] C. Delerue, G. Allan and M. Lannoo, *Theoretical aspects of the luminescence of porous silicon*, Physical Review B **48**, 11024 (1993).
- [Efros97] A. L. Efros and M. Rosen, *Random telegraph signal in the photoluminescence intensity of a single quantum dot*, Physical Review Letters **78**, 1110 (1997).
- [Efros16] A. L. Efros and D. J. Nesbitt, *Origin and control of blinking in quantum dots*, Nature Nanotechnology **11**, 661 (2016).
- [Ehenschwender11] T. Ehenschwender and H.-A. Wagenknecht, *4,4-Difluoro-4-bora-3a,4a-diaza-s-indacene as a Bright Fluorescent Label for DNA*, The Journal of Organic Chemistry **76**, 2301 (2011).
- [Erlebacher02] J. Erlebacher, A. Karma, N. Dimitrov, K. Sieradzki and M. J. Aziz, *Evolution of nanoporosity in dealloying*, Nature **410**, 450 (2002).

- [Eyre08] R. J. Eyre, J. P. Goss and P. R. Briddon, *Effect of progressive oxidation on the optical properties of small silicon quantum dots: A computational study*, *A* **77**, 1 (2008).
- [Fort07] E. Fort and S. Grésillon, *Surface enhanced fluorescence*, *Journal of Physics D: Applied Physics* **41**, 013001 (2007).
- [Fox02] M. Fox and G. F. Bertsch, *Optical Properties of Solids*, *American Journal of Physics* **70**, 1269 (2002).
- [Fox17] M. Fox and R. Ispasoiu, *Quantum Wells, Superlattices, and Band-Gap Engineering*, in *Springer Handbook of Electronic and Photonic Materials*, 1–1, Springer International Publishing (2017).
- [Frank07] I. W. Frank, D. M. Tanenbaum, A. M. van der Zande and P. L. McEuen, *Mechanical properties of suspended graphene sheets*, *Journal of Vacuum Science & Technology B: Microelectronics and Nanometer Structures* **25**, 2558 (2007).
- [Frantsuzov08] P. Frantsuzov, M. Kuno, B. Jankó and R. A. Marcus, *Universal emission intermittency in quantum dots, nanorods and nanowires*, *Nature Physics* **4**, 519 (2008).
- [Galland11] C. Galland, Y. Ghosh, A. Steinbrück, M. Sykora, J. A. Hollingsworth, V. I. Klimov and H. Htoon, *Two types of luminescence blinking revealed by spectroelectrochemistry of single quantum dots*, *Nature* **479**, 203 (2011).
- [Glas07] F. Glas, J.-C. Harmand and G. Patriarche, *Why Does Wurtzite Form in Nanowires of III-V Zinc Blende Semiconductors?*, *Physical Review Letters* **99** (2007).
- [Godt06] J. Godt, F. Scheidig, C. Grosse-Siestrup, V. Esche, P. Brandenburg, A. Reich and D. A. Groneberg, *Journal of Occupational Medicine and Toxicology* **1**, 22 (2006).
- [Grover97] L. K. Grover, *Quantum mechanics helps in searching for a needle in a haystack*, *Physical Review Letters* **79**, 325 (1997).
- [Hartsfield16] T. Hartsfield, M. Gegg, P. H. Su, M. R. Buck, J. A. Hollingsworth, C. K. Shih, M. Richter, H. Htoon and X. Li, *Semiconductor Quantum Dot Lifetime Near an Atomically Smooth Ag Film Exhibits a Narrow Distribution*, *ACS Photonics* **3**, 1085 (2016).
- [He15] Y.-M. He, G. Clark, J. R. Schaibley, Y. He, M.-C. Chen, Y.-J. Wei, X. Ding, Q. Zhang, W. Yao, X. Xu, C.-Y. Lu and J.-W. Pan, *Single quantum emitters in monolayer semiconductors*, *Nature Nanotechnology* **10**, 497 (2015).
- [He16a] X. He, H. Li, Z. Zhu, Z. Dai, Y. Yang, P. Yang, Q. Zhang, P. Li, U. Schwingenschlogl and X. Zhang, *Strain engineering in monolayer WS<sub>2</sub>, MoS<sub>2</sub>, and the WS<sub>2</sub>/MoS<sub>2</sub> heterostructure*, *Applied Physics Letters* **109**, 173105 (2016).

## BIBLIOGRAPHY

---

- [He16b] Z. He, X. Wang, W. Xu, Y. Zhou, Y. Sheng, Y. Rong, J. M. Smith and J. H. Warner, *Revealing Defect-State Photoluminescence in Monolayer WS<sub>2</sub> by Cryogenic Laser Processing*, ACS Nano **10**, 5847 (2016).
- [Hill15] H. M. Hill, A. F. Rigosi, C. Roquelet, A. Chernikov, T. C. Berkelbach, D. R. Reichman, M. S. Hybertsen, L. E. Brus and T. F. Heinz, *Observation of Excitonic Rydberg States in Monolayer MoS<sub>2</sub> and WS<sub>2</sub> by Photoluminescence Excitation Spectroscopy*, Nano Letters **15**, 2992 (2015).
- [Islam04] M. A. Islam, *Einstein–Smoluchowski Diffusion Equation: A Discussion*, Physica Scripta **70**, 120 (2004).
- [Ji15] B. Ji, E. Giovanelli, B. Habert, P. Spinicelli, M. Nasilowski, X. Xu, N. Lequeux, J. P. Hugonin, F. Marquier, J. J. Greffet and B. Dubertret, *Non-blinking quantum dot with a plasmonic nanoshell resonator*, Nature Nanotechnology **10**, 170 (2015).
- [Jiang88] D. S. Jiang, H. Jung and K. Ploog, *Temperature dependence of photoluminescence from GaAs single and multiple quantum-well heterostructures grown by molecular-beam epitaxy*, Journal of Applied Physics **64**, 1371 (1988).
- [Joyce10] H. J. Joyce, J. Wong-Leung, Q. Gao, H. H. Tan and C. Jagadish, *Phase Perfection in Zinc Blende and Wurtzite III-V Nanowires Using Basic Growth Parameters*, Nano Letters **10**, 908 (2010).
- [Kastl19] C. Kastl, R. J. Koch, C. T. Chen, J. Eichhorn, S. Ulstrup, A. Bostwick, C. Jozwiak, T. R. Kuykendall, N. J. Borys, F. M. Toma, S. Aloni, A. Weber-Bargioni, E. Rotenberg and A. M. Schwartzberg, *Effects of Defects on Band Structure and Excitons in WS<sub>2</sub> Revealed by Nanoscale Photoemission Spectroscopy*, ACS Nano (2019).
- [Kazimierczuk14] T. Kazimierczuk, D. Fröhlich, S. Scheel, H. Stolz and M. Bayer, *Giant Rydberg excitons in the copper oxide Cu<sub>2</sub>O*, Nature **514**, 343 (2014).
- [Kee05] H. L. Kee, C. Kirmaier, L. Yu, P. Thamyongkit, W. J. Youngblood, M. E. Calder, L. Ramos, B. C. Noll, D. F. Bocian, W. R. Scheidt, R. R. Birge, J. S. Lindsey and D. Holten, *Structural Control of the Photodynamics of Boron-Dipyrroin Complexes*, The Journal of Physical Chemistry B **109**, 20433 (2005).
- [Kim17] H. S. Kim, S.-R. Park and M. C. Suh, *Concentration Quenching Behavior of Thermally Activated Delayed Fluorescence in a Solid Film*, The Journal of Physical Chemistry C **121**, 13986 (2017).
- [Klimov10] V. Klimov (Hg.), *Nanocrystal Quantum Dots, Second Edition*, CRC Press (2010).
- [Komsa13] H.-P. Komsa, S. Kurasch, O. Lehtinen, U. Kaiser and A. V. Krasheninnikov, *From point to extended defects in two-dimensional MoS<sub>2</sub>: Evolution of atomic structure under electron irradiation*, Physical Review B **88** (2013).

- [Kozubek19] R. Kozubek, M. Tripathi, M. Ghorbani-Asl, S. Kretschmer, L. Madauß, E. Pollmann, M. O'Brien, N. McEvoy, U. Ludacka, T. Susi, G. S. Duesberg, R. A. Wilhelm, A. V. Krasheninnikov, J. Kotakoski and M. Schleberger, *Perforating Freestanding Molybdenum Disulfide Monolayers with Highly Charged Ions*, The Journal of Physical Chemistry Letters **10**, 904 (2019).
- [Ledoux00] G. Ledoux, O. Guillois, D. Porterat, C. Reynaud, F. Huisken, B. Kohn and V. Paillard, *Photoluminescence properties of silicon nanocrystals as a function of their size*, Physical Review B **62**, 15942 (2000).
- [Ledoux01] G. Ledoux, J. Gong and F. Huisken, *Effect of passivation and aging on the photoluminescence of silicon nanocrystals*, A **79**, 4028 (2001).
- [Lent97] C. Lent and P. Tougaw, *A device architecture for computing with quantum dots*, Proceedings of the IEEE **85**, 541 (1997).
- [Liptak08] R. W. Liptak, B. Devetter, J. H. T. III, U. Kortshagen and S. A. Campbell, *SF<sub>6</sub> plasma etching of silicon nanocrystals*, Nanotechnology **20**, 035603 (2008).
- [Liptak12] R. W. Liptak, J. Yang, N. J. Kramer, U. Kortshagen and S. A. Campbell, *Environmental photostability of SF<sub>6</sub>-etched silicon nanocrystals*, Nanotechnology **23**, 395205 (2012).
- [Liu19] H. Liu, C. Wang, D. Liu and J. Luo, *Neutral and defect-induced exciton annihilation in defective monolayer WS<sub>2</sub>*, Nanoscale **11**, 7913 (2019).
- [Lu15] J. Lu, A. Carvalho, X. K. Chan, H. Liu, B. Liu, E. S. Tok, K. P. Loh, A. H. C. Neto and C. H. Sow, *Atomic Healing of Defects in Transition Metal Dichalcogenides*, Nano Letters **15**, 3524 (2015).
- [Luo13] G.-G. Luo, J.-X. Xia, K. Fang, Q.-H. Zhao, J.-H. Wu and J.-C. Dai, *Discovery of polymorphism-dependent emission for crystalline boron-dipyrrromethene dye*, Dalton Transactions **42**, 16268 (2013).
- [Lüttjohann07] S. Lüttjohann, C. Meier, M. Offer, A. Lorke and H. Wiggers, *Temperature-induced crossover between bright and dark exciton emission in silicon nanoparticles*, Epl **79** (2007).
- [Mahler08] B. Mahler, P. Spinicelli, S. Buil, X. Quelin, J. P. Hermier and B. Dubertret, *Towards non-blinking colloidal quantum dots*, Nature Materials **7**, 659 (2008).
- [Manders15] J. R. Manders, L. Qian, A. Titov, J. Hyvonen, J. Tokarz-Scott, J. Xue and P. H. Holloway, *8.3: Distinguished Paper : Next-Generation Display Technology: Quantum-Dot LEDs*, SID Symposium Digest of Technical Papers **46**, 73 (2015).

## BIBLIOGRAPHY

---

- [Mangolini05] L. Mangolini, E. Thimsen and U. Kortshagen, *High-Yield Plasma Synthesis of Luminescent Silicon Nanocrystals*, Nano Letters **5**, 655 (2005).
- [Meier03] F. Meier, J. Levy and D. Loss, *Quantum Computing with Spin Cluster Qubits*, Physical Review Letters **90**, 4 (2003).
- [Min96] K. Min, K. Min, K. Shcheglov, K. Shcheglov, C. Yang, C. Yang, H. Atwater and H. Atwater, *Defect-related versus excitonic visible light emission from ion beam synthesized Si nanocrystals in SiO<sub>2</sub>*, Applied Physics Letters **69**, 2033 (1996).
- [Momma11] K. Momma and F. Izumi, *VESTA 3for three-dimensional visualization of crystal, volumetric and morphology data*, Journal of Applied Crystallography **44**, 1272 (2011).
- [Monsma89] F. J. Monsma, A. C. Barton, H. C. Kang, D. L. Brassard, R. P. Haugland and D. R. Sibley, *Characterization of Novel Fluorescent Ligands with High Affinity for D1 and D2 Dopaminergic Receptors*, Journal of Neurochemistry **52**, 1641 (1989).
- [Murata11] K. Murata, Y. Yasutake, K. I. Nittoh, S. Fukatsu and K. Miki, *High-density G-centers, light-emitting point defects in silicon crystal*, AIP Advances **1** (2011).
- [Neto09] A. H. C. Neto, F. Guinea, N. M. R. Peres, K. S. Novoselov and A. K. Geim, *The electronic properties of graphene*, Reviews of Modern Physics **81**, 109 (2009).
- [Neuhauser00] R. G. Neuhauser, K. T. Shimizu, W. K. Woo, S. A. Empedocles and M. G. Bawendi, *Correlation between Fluorescence Intermittency and Spectral Diffusion*, Physical Review Letters 3301–3304 (2000).
- [Nirmal96] M. Nirmal, B. O. Dabbousi, M. G. Bawendi, J. J. Macklin, J. K. Trautman, T. D. Harris and L. E. Brus, *Fluorescence intermittency in single cadmium selenide nanocrystals*, Nature **383**, 802 (1996).
- [Okada16] D. Okada, T. Nakamura, D. Braam, T. D. Dao, S. Ishii, T. Nagao, A. Lorke, T. Nabeshima and Y. Yamamoto, *Color-Tunable Resonant Photoluminescence and Cavity-Mediated Multistep Energy Transfer Cascade*, ACS Nano **10**, 7058 (2016).
- [Ozdemir09] T. Ozdemir, S. Atilgan, I. Kutuk, L. T. Yildirim, A. Tulek, M. Bayindir and E. U. Akkaya, *Solid-State Emissive BODIPY Dyes with Bulky Substituents As Spacers*, Organic Letters **11**, 2105 (2009).
- [Pei19] W. Pei, Y. Liu, J. Deng, K. Zhang, Z. Hou, X. Zhao and H. Dai, *Partially embedding Pt nanoparticles in the skeleton of 3DOM Mn<sub>2</sub>O<sub>3</sub>: An effective strategy for enhancing catalytic stability in toluene combustion*, Applied Catalysis B: Environmental **256**, 117814 (2019).

- [Pellegrini95] V. Pellegrini, F. Fuso, G. Lorenzi, M. Allegrini, A. Diligenti, A. Nannini and G. Pennelli, *Improved optical emission of porous silicon with different postanodization processes*, Applied Physics Letters **67**, 1084 (1995).
- [Richard04] S. Richard, F. Aniel and G. Fishman, *Energy-band structure of Ge, Si, and GaAs: A thirty-band k-p method*, Physical Review B **70** (2004).
- [Royo17] M. Royo, M. D. Luca and R. Rurali, *Probing silicon quantum dots by single-dot techniques*, A **28**, 072002 (2017).
- [Saeki11] A. Saeki, Y. Yamamoto, Y. Koizumi, T. Fukushima, T. Aida and S. Seki, *Photoconductivity of Self-Assembled Hexabenzocoronene Nanotube: Insight into the Charge Carrier Mobilities on Local and Long-Range Scales*, The Journal of Physical Chemistry Letters **2**, 2549 (2011).
- [Santen84] R. A. V. Santen, *The Ostwald step rule*, The Journal of Physical Chemistry **88**, 5768 (1984).
- [Schlamp97] M. C. Schlamp, X. Peng and A. P. Alivisatos, *Improved efficiencies in light emitting diodes made with CdSe(CdS) core/shell type nanocrystals and a semiconducting polymer*, Journal of Applied Physics **82**, 5837 (1997).
- [SCOTT79] D. W. SCOTT, *On optimal and data-based histograms*, Biometrika **66**, 605 (1979).
- [Shah90] M. Shah, K. Thangaraj, M.-L. Soong, L. T. Wolford, J. H. Boyer, I. R. Politzer and T. G. Pavlopoulos, *Pyromethene-BF<sub>2</sub> complexes as laser dyes: I.*, Heteroatom Chemistry **1**, 389 (1990).
- [Shimizu02] K. T. Shimizu, W. K. Woo, B. R. Fisher, H. J. Eisler and M. G. Bawendi, *Surface-Enhanced Emission from Single Semiconductor Nanocrystals*, Physical Review Letters **89**, 9 (2002).
- [Sinturel13] C. Sinturel, M. Vayer, M. Morris and M. A. Hillmyer, *Solvent Vapor Annealing of Block Polymer Thin Films*, Macromolecules **46**, 5399 (2013).
- [Spies13] C. Spies, A.-M. Huynh, V. Huch and G. Jung, *Correlation between Crystal Habit and Luminescence Properties of 4,4-Difluoro-1,3-dimethyl-4-bora-3a,4a-diaza-s-indacene, An Asymmetric BODIPY Dye*, The Journal of Physical Chemistry C **117**, 18163 (2013).
- [Spirkoska09] D. Spirkoska, J. Arbiol, A. Gustafsson, S. Conesa-Boj, F. Glas, I. Zardo, M. Heigoldt, M. H. Gass, A. L. Bleloch, S. Estrade, M. Kaniber, J. Rossler, F. Peiro, J. R. Morante, G. Abstreiter, L. Samuelson and A. F. i Morral, *Structural and optical properties of high quality zinc-blende/wurtzite GaAs nanowire heterostructures*, Physical Review B **80** (2009).
- [Splendiani10] A. Splendiani, L. Sun, Y. Zhang, T. Li, J. Kim, C.-Y. Chim, G. Galli and F. Wang, *Emerging Photoluminescence in Monolayer MoS<sub>2</sub>*, Nano Letters **10**, 1271 (2010).

## BIBLIOGRAPHY

---

- [Suemoto94] T. Suemoto, K. Tanaka and A. Nakajima, *Interpretation of the temperature dependence of the luminescence intensity, lifetime, and decay profiles in porous Si*, *A* **49**, 11005 (1994).
- [Sychugov17] I. Sychugov, J. Valenta and J. Linnros, *Probing silicon quantum dots by single-dot techniques*, *Nanotechnology* **28**, 072002 (2017).
- [Tang87] C. W. Tang and S. A. VanSlyke, *Organic electroluminescent diodes*, *Applied Physics Letters* **51**, 913 (1987).
- [Tongay13] S. Tongay, J. Suh, C. Ataca, W. Fan, A. Luce, J. S. Kang, J. Liu, C. Ko, R. Raghunathanan, J. Zhou, F. Ogletree, J. Li, J. C. Grossman and J. Wu, *Defects activated photoluminescence in two-dimensional semiconductors: interplay between bound, charged and free excitons*, *Scientific Reports* **3** (2013).
- [vanSark01] W. G. J. H. M. van Sark, P. L. T. M. Frederix, D. J. V. den Heuvel, H. C. Gerritsen, A. A. Bol, J. N. J. van Lingen, C. de Mello Donegá and A. Meijerink, *Photooxidation and Photobleaching of Single CdSe/ZnS Quantum Dots Probed by Room-Temperature Time-Resolved Spectroscopy*, *The Journal of Physical Chemistry B* **105**, 8281 (2001).
- [vanSark02] W. G. J. H. M. van Sark, P. L. T. M. Frederix, A. A. Bol, H. C. Gerritsen and A. Meijerink, *Blueing, Bleaching, and Blinking of Single CdSe/ZnS Quantum Dots*, *ChemPhysChem* **3**, 871 (2002).
- [Varshni67] Y. Varshni, *Temperature dependence of the energy gap in semiconductors*, *Physica* **34**, 149 (1967).
- [Wang12] Q. H. Wang, K. Kalantar-Zadeh, A. Kis, J. N. Coleman and M. S. Strano, *Electronics and optoelectronics of two-dimensional transition metal dichalcogenides*, *Nature Nanotechnology* **7**, 699 (2012).
- [Wang15] Y. Wang, C. Cong, W. Yang, J. Shang, N. Peimyoo, Y. Chen, J. Kang, J. Wang, W. Huang and T. Yu, *Strain-induced direct–indirect bandgap transition and phonon modulation in monolayer WS<sub>2</sub>*, *Nano Research* **8**, 2562 (2015).
- [Weißbon12] J. Weißbon, *Magnetotransporteigenschaften von Magnetotransporteigenschaften von nanoporösen Goldfilmen*, Master thesis, Universität Duisburg-Essen (2012).
- [Withers15] F. Withers, O. D. Pozo-Zamudio, A. Mishchenko, A. P. Rooney, A. Gholinia, K. Watanabe, T. Taniguchi, S. J. Haigh, A. K. Geim, A. I. Tartakovskii and K. S. Novoselov, *Light-emitting diodes by band-structure engineering in van der Waals heterostructures*, *Nature Materials* **14**, 301 (2015).
- [Wolkin98] M. V. Wolkin, J. Jorne and P. M. Fauchet, *Wolk+99Prl*, *A* 1–4 (1998).

- [Xiao07] S. Xiao, Y. Zou, J. Wu, Y. Zhou, T. Yi, F. Li and C. Huang, *Hydrogen bonding assisted switchable fluorescence in self-assembled complexes containing diarylethene: controllable fluorescent emission in the solid state*, Journal of Materials Chemistry **17**, 2483 (2007).
- [Xiao12] D. Xiao, G.-B. Liu, W. Feng, X. Xu and W. Yao, *Coupled Spin and Valley Physics in Monolayers of MoS<sub>2</sub> and Other Group-VI Dichalcogenides*, Physical Review Letters **108** (2012).
- [Xu15] Y. Xu, L. Chen, X. Wang, W. Yao and Q. Zhang, *Recent advances in noble metal based composite nanocatalysts: colloidal synthesis, properties, and catalytic applications*, Nanoscale **7**, 10559 (2015).
- [Yao15] L. Yao, T. Yu, L. Ba, H. Meng, X. Fang, Y. Wang, L. Li, X. Rong, S. Wang, X. Wang, G. Ran, X. Pi and G. Qin, *Efficient silicon quantum dots light emitting diodes with an inverted device structure*, Journal of Materials Chemistry C **4**, 673 (2015).
- [Ye11] M. Ye and P. C. Searson, *Blinking in quantum dots: The origin of the grey state and power law statistics*, Physical Review B - Condensed Matter and Materials Physics **84**, 1 (2011).
- [Yu10] P. Y. Yu and M. Cardona, *Fundamentals of Semiconductors*, Springer Berlin Heidelberg (2010).
- [Yuan15] L. Yuan and L. Huang, *Exciton dynamics and annihilation in WS<sub>2</sub> 2D semiconductors*, Nanoscale **7**, 7402 (2015).
- [Zatryb11] G. Zatryb, A. Podhorodecki, J. Misiewicz, J. Cardin and F. Gourbilleau, *On the nature of the stretched exponential photoluminescence decay for silicon nanocrystals*, Nanoscale Research Letters **6**, 106 (2011).
- [Zheng19] K. Zheng, Z. Zhang, X. Wang, R. Zhan, H. Chen, S. Deng, N. Xu and J. Chen, *Mechanism of photoluminescence quenching in visible and ultraviolet emissions of ZnO nanowires decorated with gold nanoparticles*, Japanese Journal of Applied Physics **58**, 051005 (2019).
- [Zhou12] L. Zhou, F. Ding, H. Chen, W. Ding, W. Zhang and S. Y. Chou, *Enhancement of Immunoassay's Fluorescence and Detection Sensitivity Using Three-Dimensional Plasmonic Nano-Antenna-Dots Array*, Analytical Chemistry **84**, 4489 (2012).

# Appendix A

## Appendix

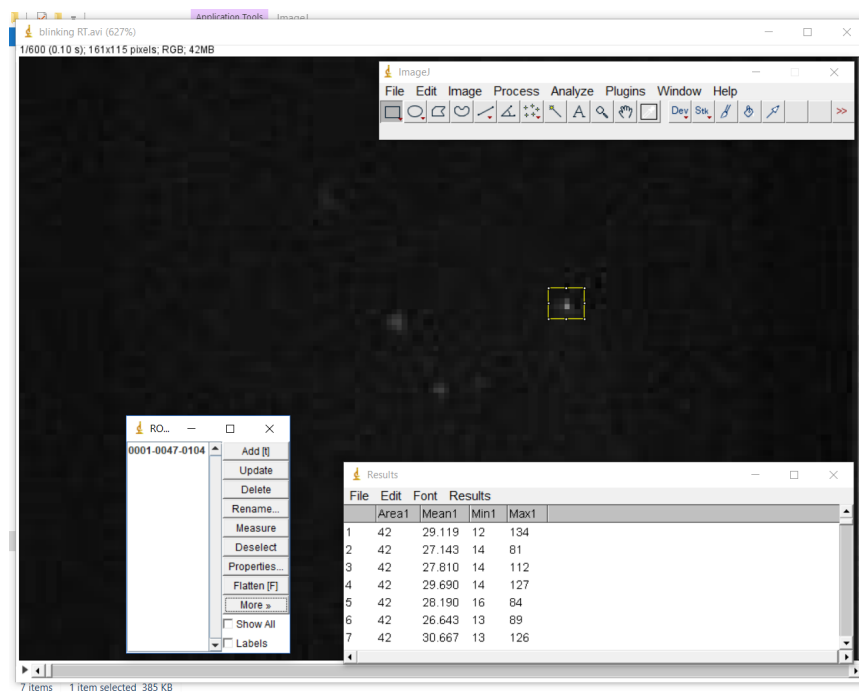


Figure A.1: (a) An example of how single particle blinking were collected using imagej software.

Multiple frames of images containing the single particle blinking was opened in imagej software. In the imagej, there is an option of analysing a region of interest (ROI manager). This analysis by imagej gives out the intensities from that particular region across the frames, like in the Figure A.1. This data was then analysed further to study the statistics discussed in chapter 4.

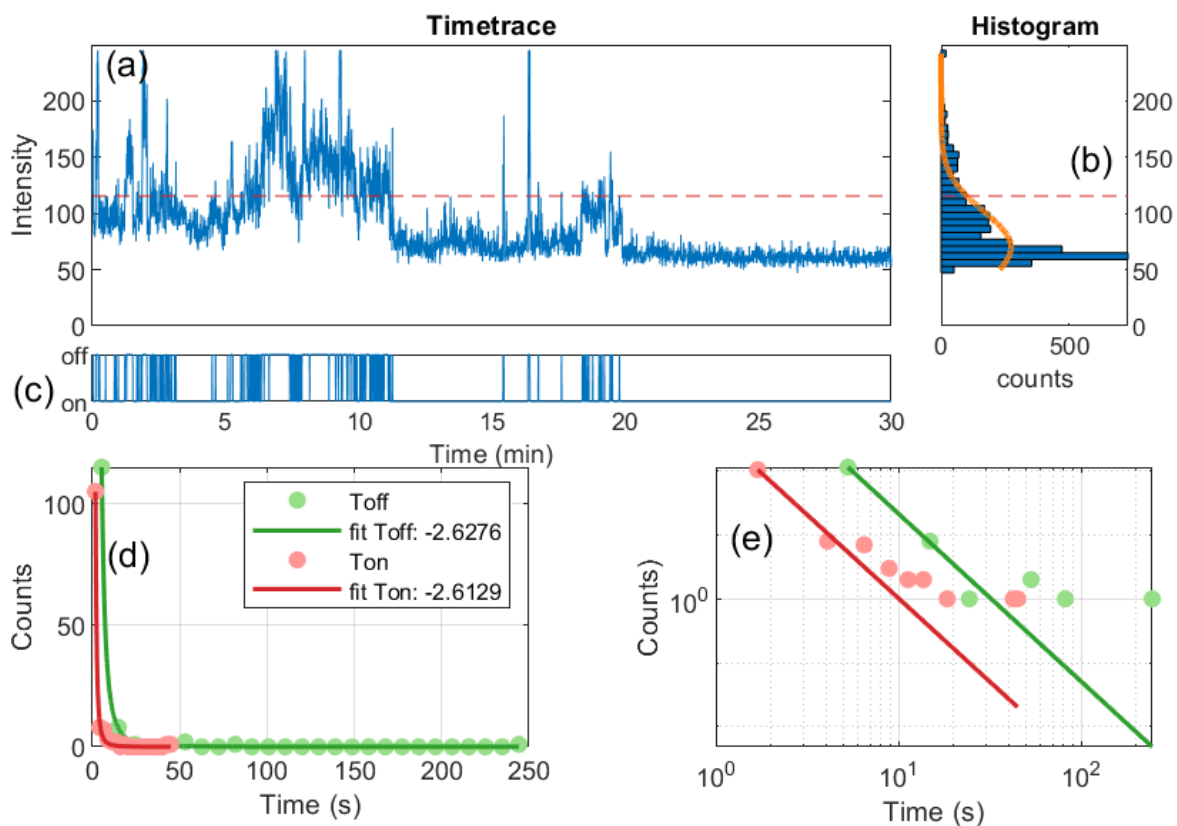


Figure A.2: (a) time trace of photon counts from one SiNP, (b) bin of intensities to identify the threshold, (c) plot showing binary on-off in the time trace, (e) power law statistics of "on" and "off" times from a single SiNP and (e) logarithmic plot of (d).

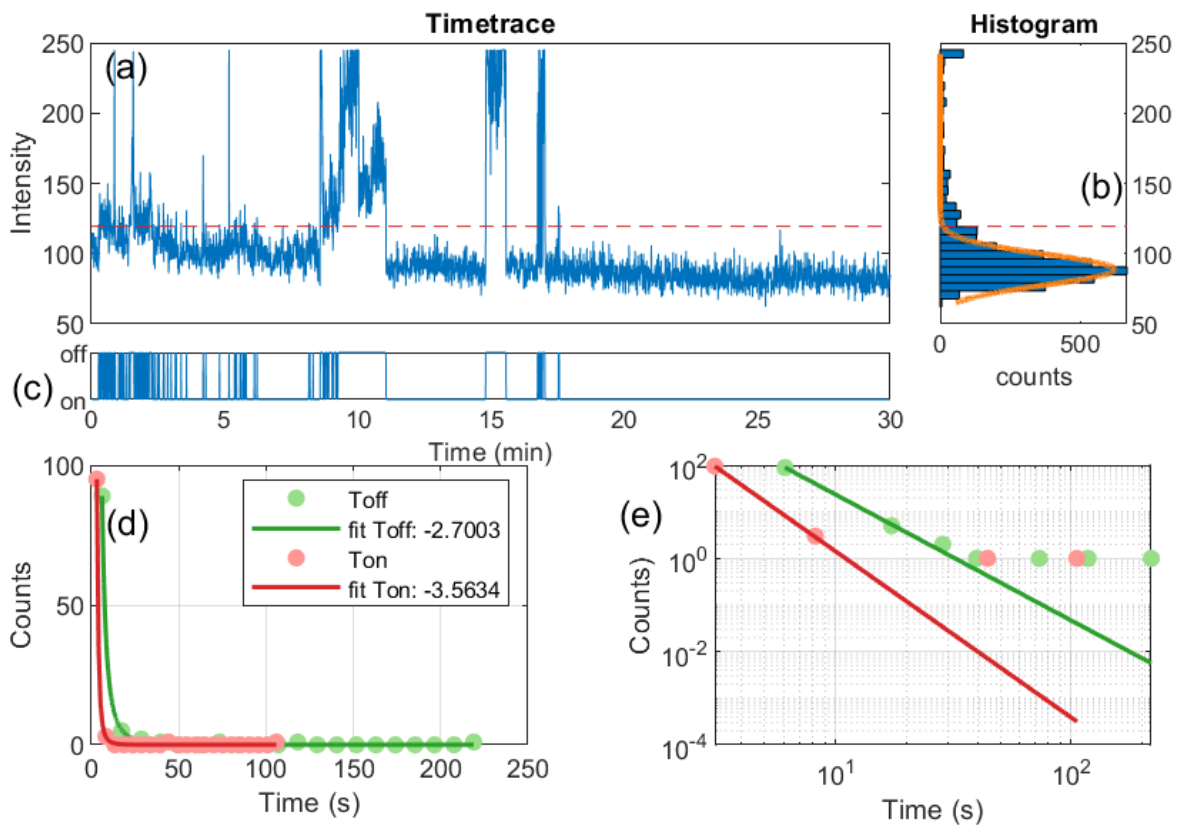


Figure A.3: (a) time trace of photon counts from one SiNP, (b) bin of intensities to identify the threshold, (c) plot showing binary on-off in the time trace, (e) power law statistics of "on" and "off" times from a single SiNP and (e) logarithmic plot of (d).

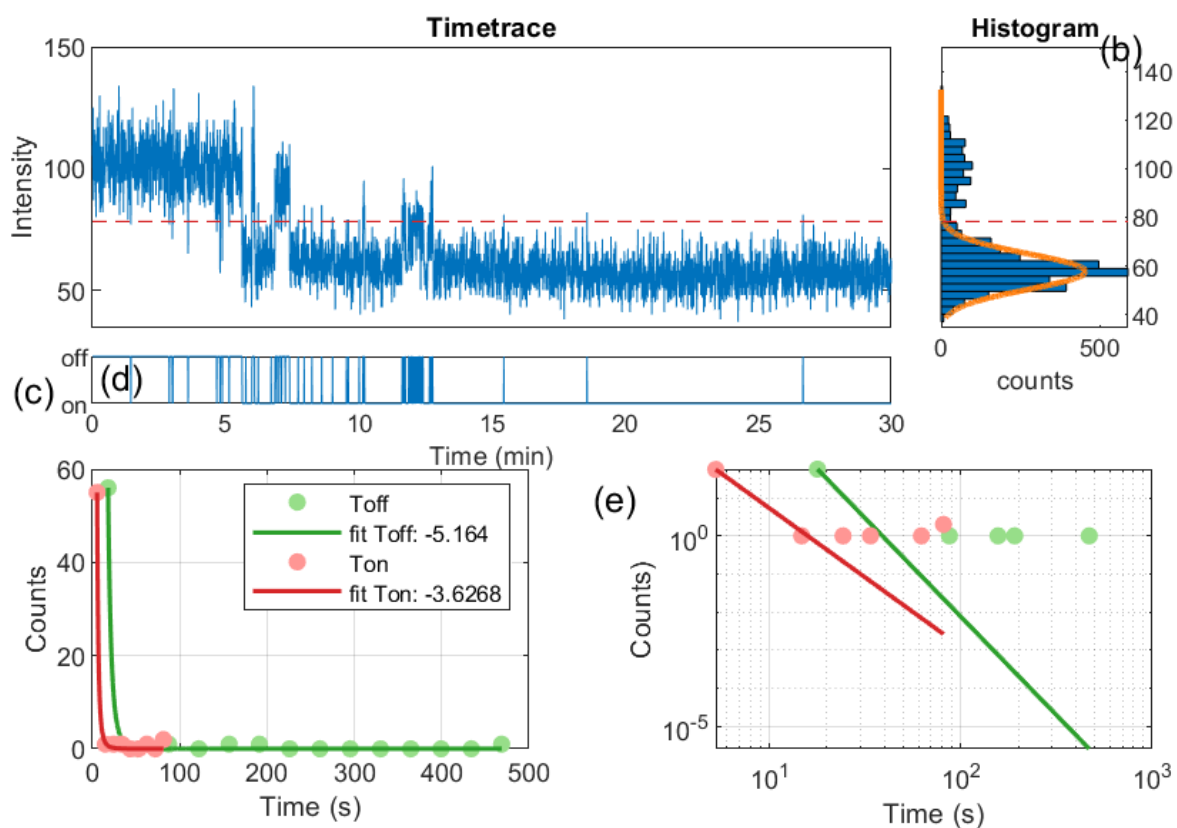


Figure A.4: (a) time trace of photon counts from one SiNP, (b) bin of intensities to identify the threshold, (c) plot showing binary on-off in the time trace, (e) power law statistics of "on" and "off" times from a single SiNP and (e) logarithmic plot of (d).

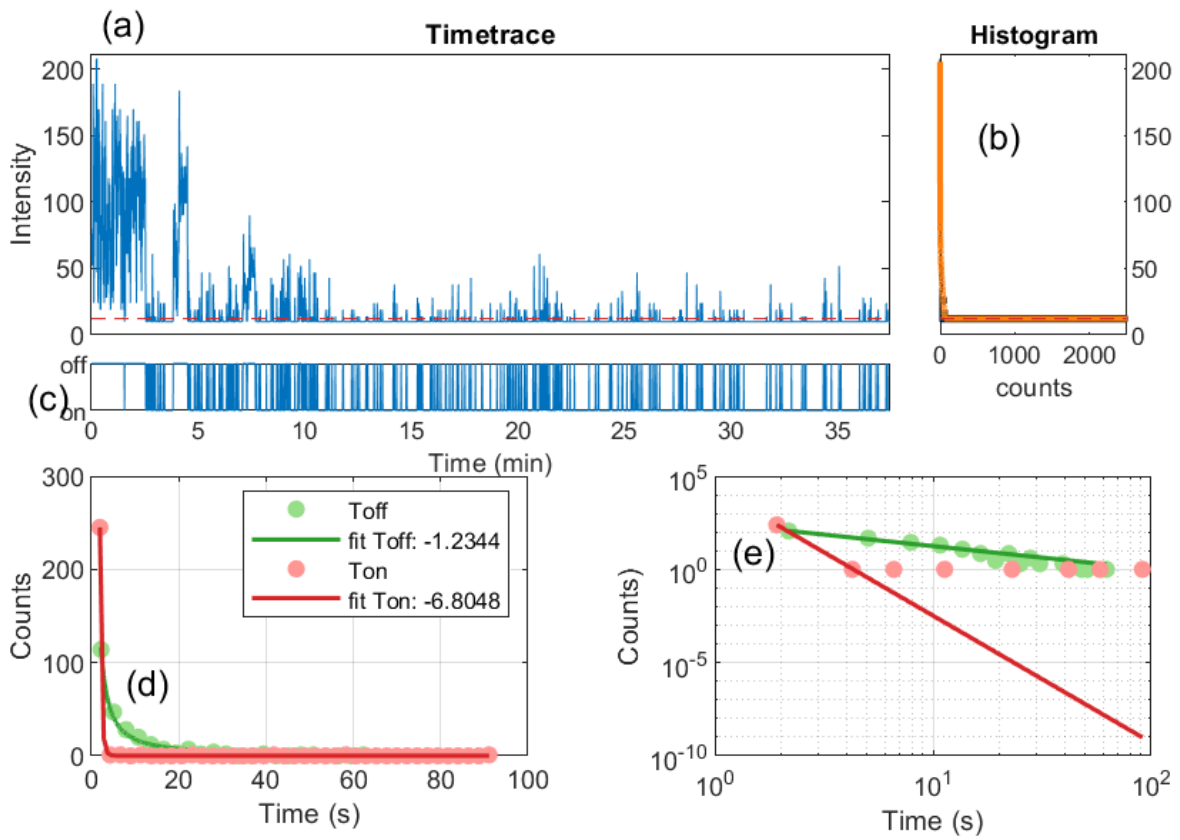


Figure A.5: (a) time trace of photon counts from one SiNP, (b) bin of intensities to identify the threshold, (c) plot showing binary on-off in the time trace, (e) power law statistics of "on" and "off" times from a single SiNP and (e) logarithmic plot of (d).

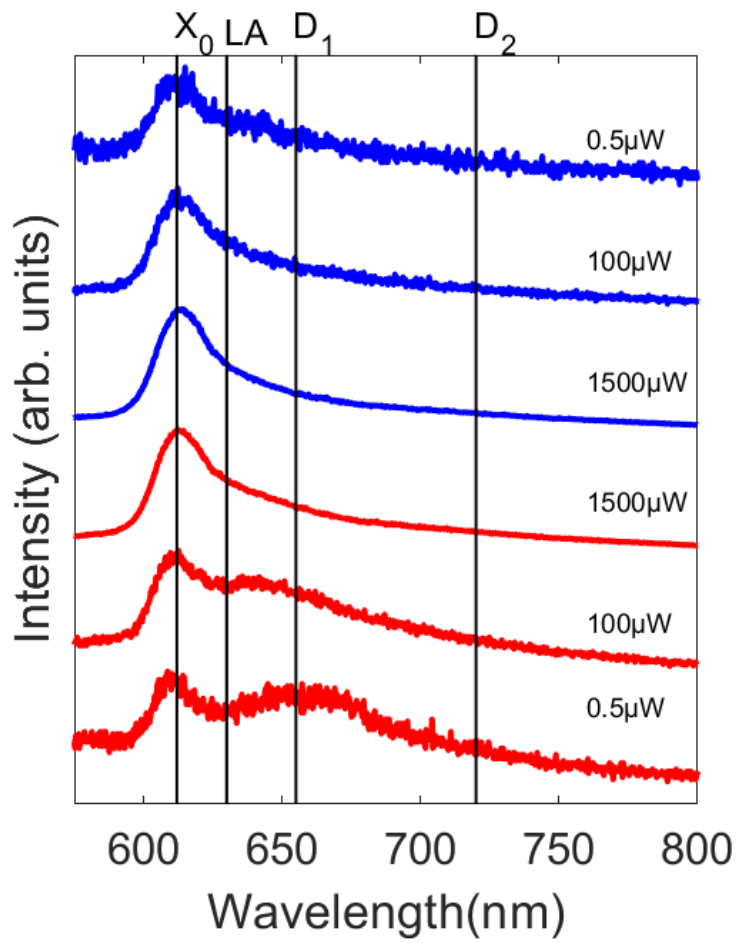


Figure A.6: PL spectra of WS<sub>2</sub> monolayer at 83K at different excitation power for flakes irradiated with  $6000\mu\text{m}^{-2}$  fluence of Xe<sup>30+</sup> ions.

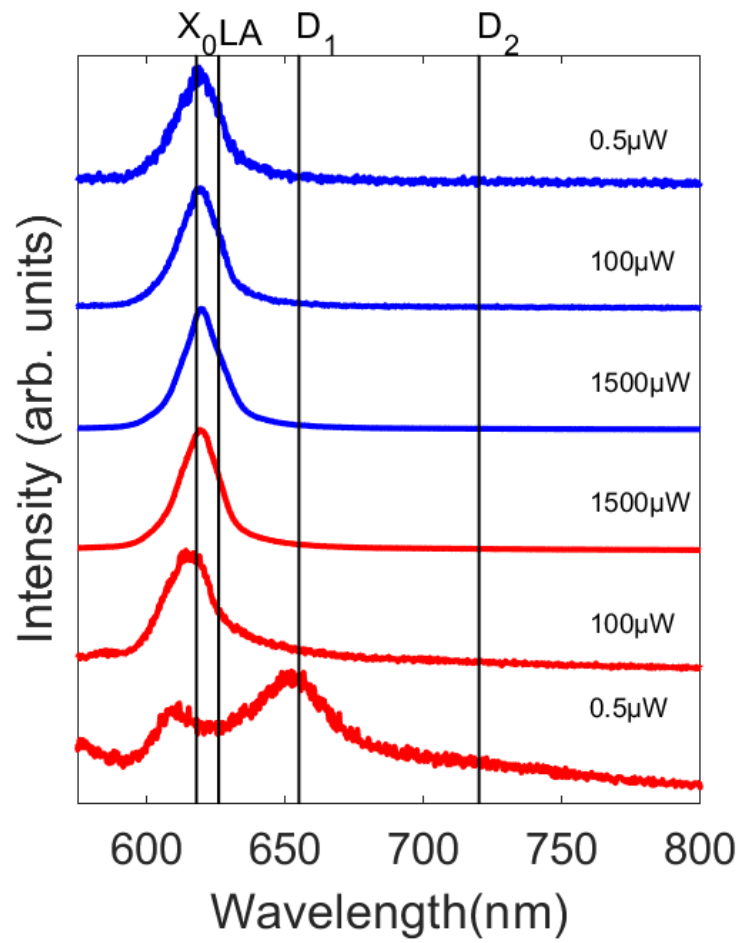


Figure A.7: PL spectra of WS<sub>2</sub> monolayer at 83K at different excitation power for flakes irradiated with  $4500\mu m^{-2}$  fluence of Xe<sup>30+</sup> ions.

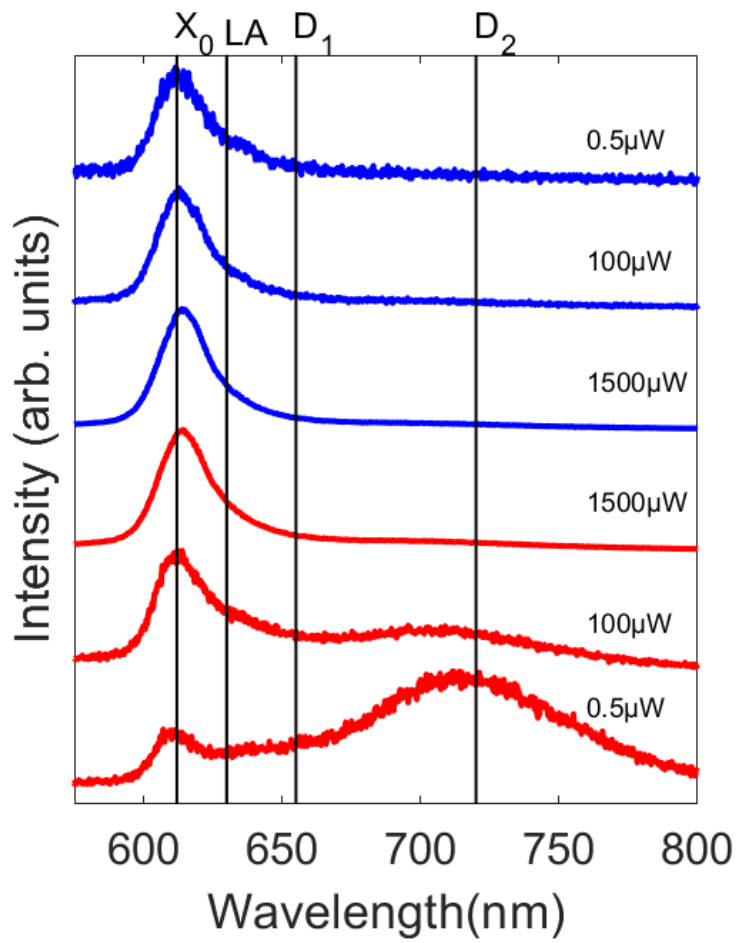


Figure A.8: PL spectra of WS<sub>2</sub> monolayer at 83K at different excitation power for flakes irradiated with  $3500\mu\text{m}^{-2}$  fluence of Xe<sup>30+</sup> ions.

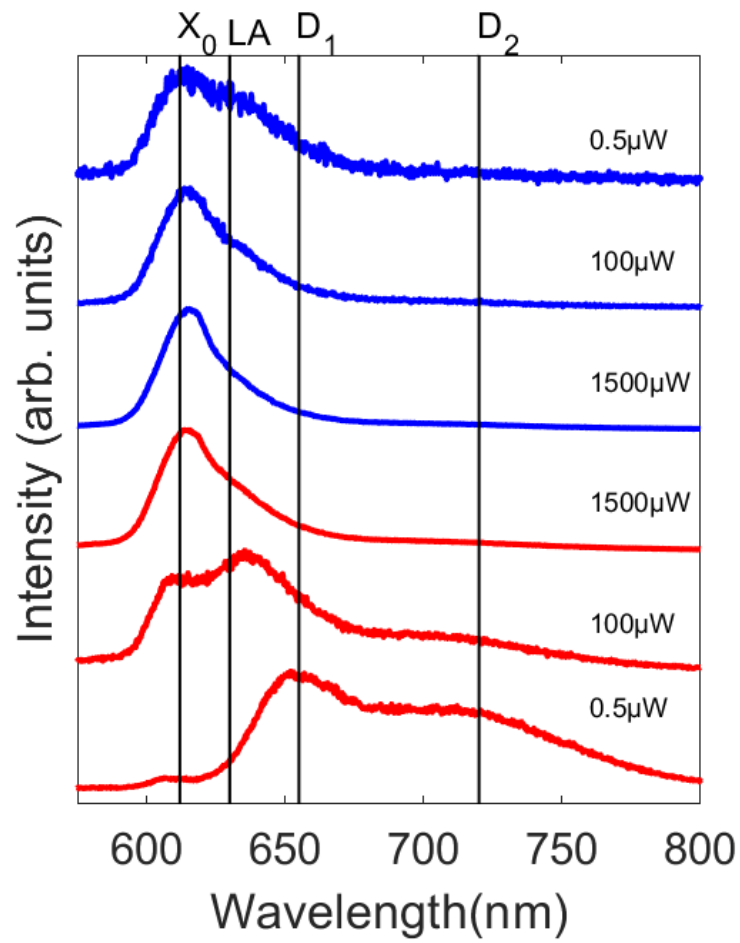


Figure A.9: PL spectra of WS<sub>2</sub> monolayer at 83K at different excitation power for flakes irradiated with  $2500\mu m^{-2}$  fluence of Xe<sup>30+</sup> ions.

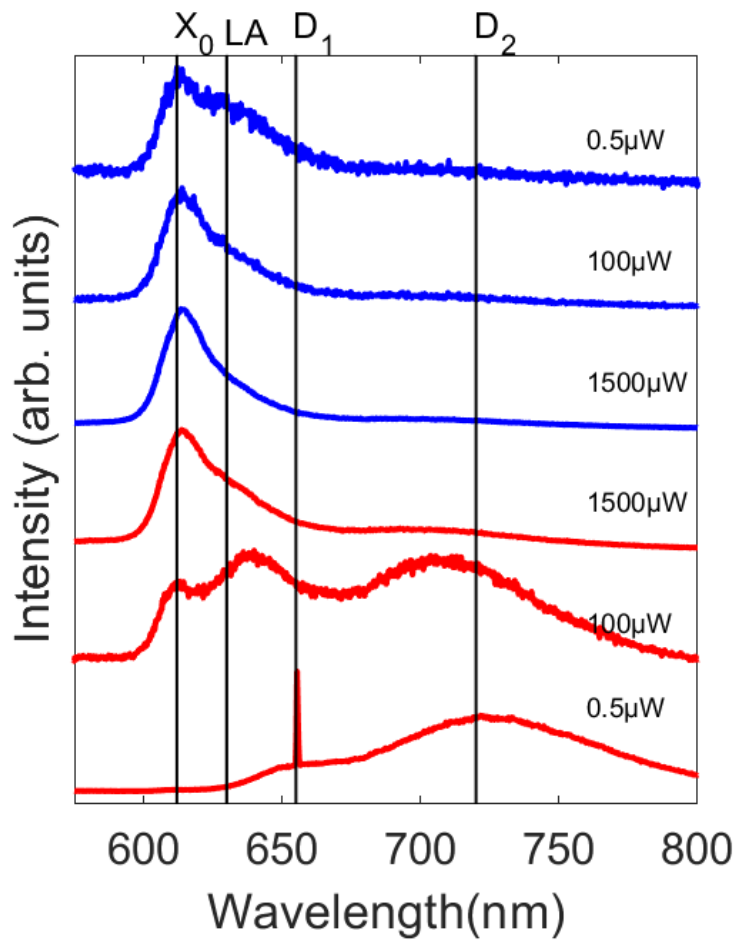


Figure A.10: PL spectra of WS<sub>2</sub> monolayer at 83K at different excitation power for flakes irradiated with  $500\mu m^{-2}$  fluence of Xe<sup>30+</sup> ions.

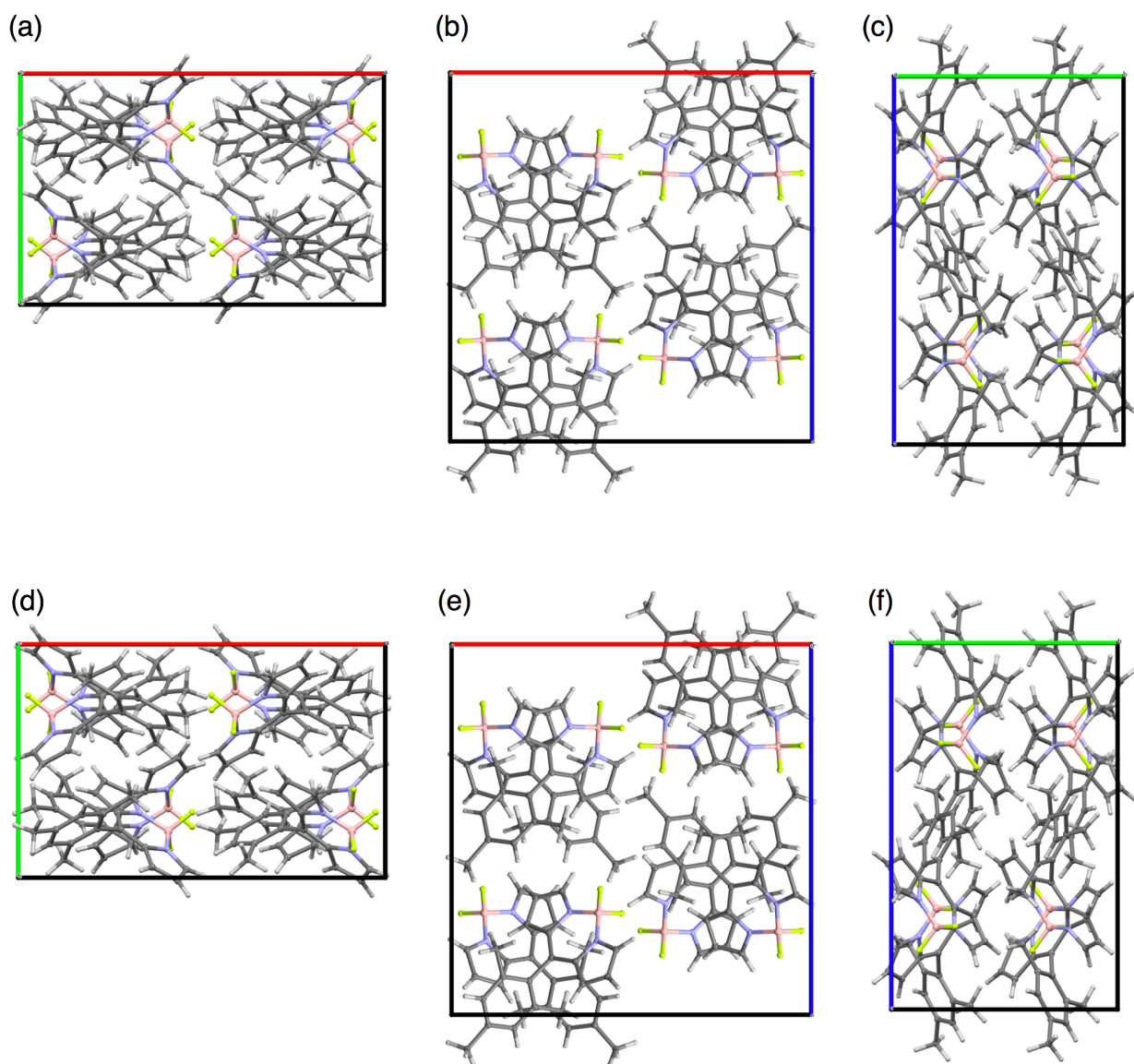


Figure A.11: Packing diagrams of BODIPY(r) at 298 K (a–c) and 96 K (d–f) viewed along crystallographic *a* (a, d), *b* (b, e), and *c* (c, f) axes. B, F, C, and H are colored in pink, yellow, gray, and white, respectively.

	T = 298 K	T = 93.15 K
Crystal system	Orthorhombic	orthorhombic
Space group	Pbca	Pbca
Unit cell dimensions	a = 16.9962(5) Å	a = 16.7485(3) Å
	b = 10.7979(3) Å	b = 10.66195(17) Å
	c = 17.3124(5) Å	c = 17.2437(3) Å
	a = 90°	a = 90°
	b = 90°	b = 90°
	g = 90°	g = 90°
Volume	3177.21(15) Å <sup>3</sup>	3079.25(10) Å <sup>3</sup>
Z	8	8
Density (calculated)	1.297 g cm <sup>-3</sup>	1.338 g cm <sup>-3</sup>
Absorption coefficient	0.759	0.783
F(000)	1296	1296
Crystal size	0.405 x 0.058 x 0.013 mm <sup>3</sup>	0.414 x 0.026 x 0.011 mm <sup>3</sup>
Theta range for data collection	5.055 to 73.135°	5.059 to 76.05°
Index ranges	-15 ≤ h ≤ 21, -11 ≤ k ≤ 13, -21 ≤ l ≤ 21	-16 ≤ h ≤ 20, -12 ≤ k ≤ 11, -20 ≤ l ≤ 14
Reflections collected	11396	9583
Final R indices [I > 2 σ(I)]	0.0582	0.0459
R indices (all data)	0.0449	0.045

Figure A.12: Crystal data and structure refinement for BODIPY(r) at 298 K and 93 K.

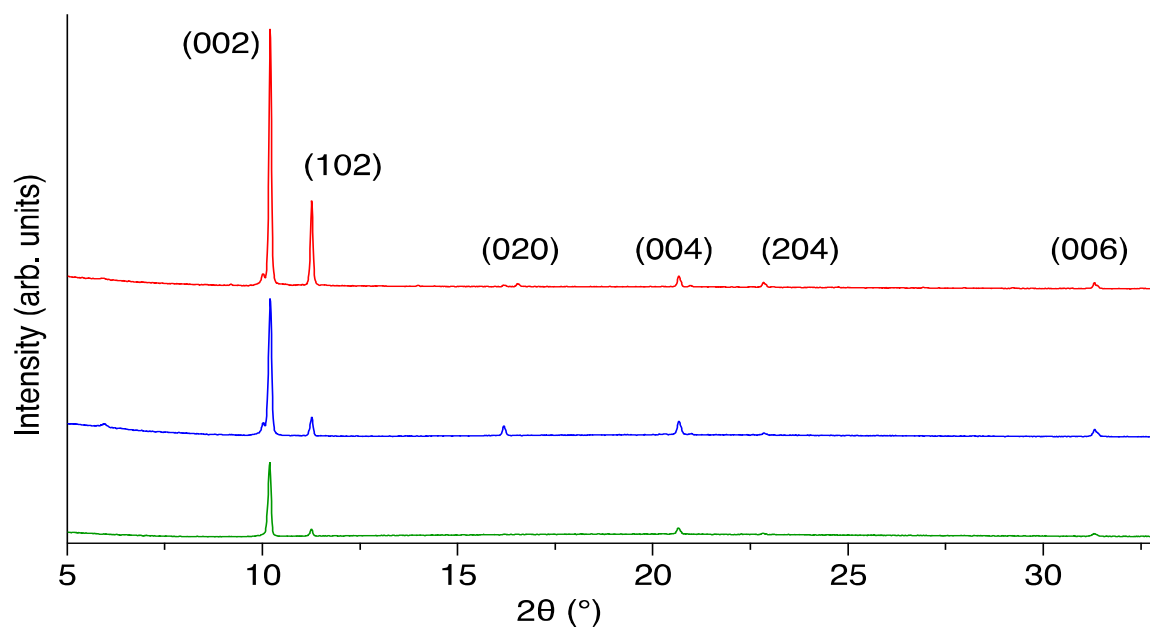


Figure A.13: Powder XRD patterns of red, striped, and green BODIPY crystals (top to bottom). Note that the orientation of the microcrystals on the sample stage affects the XRD patterns. Therefore different powder preparations exhibit different peak amplitudes.

---

## First authored/ co-authored publications from during the Ph.D.

- A. Asaithambi, D. Okada, G. Prinz, H. Sato, A. Saeki, T. Nakamura, T. Nabeshima, Y. Yamamoto and A. Lorke, Polychromatic Photoluminescence of Polymorph Boron Dipyrromethene Crystals and Heterostructures, *The Journal of Physical Chemistry C* **123**, 5061 (2019).
- R. Kaupmees, M. Grossberg, M. Ney, A. Asaithambi, A. Lorke, and J. Krustok, Tailoring of Bound Exciton Photoluminescence Emission in WS<sub>2</sub> Monolayers, *physica status solidi (RRL) – Rapid Research Letters* 1900355 (2019).

## Research visits

- 08/2017 - 10/2017 : Visit to Prof. Yohei Yamamoto's lab at University of Tsukuba, Tsukuba, Japan as a part of DAAD collaboration project.

# Acknowledgment

Credit should be given where it is due. I would like to express my gratitude to a lot of people who have contributed to the completion of this thesis.

First and foremost, many thanks to IMPRS-SurMat and university of Duisburg-Essen for providing me with the necessary scholarship during my Ph.D. time.

My sincerest gratitude to Prof. Dr. Axel Lorke, couldn't have asked for a better boss. Boss was always there whenever I hit a roadblock and also providing me with opportunities for the betterment of my professional and personal well being.

I am grateful for the weekly meeting inputs from the boss people of the group Dr. Martin Paul Geller, Dr. Nicolas Wörhl, Dr. Günther Prinz, and Prof. Dr. Axel Lorke. Also, they were into "laufen" and encouraged running together, especially Günther and Nicolas.

I would like to single out Dr. Günther Prinz, he was my designated second boss in the group. I am extremely grateful to have had Günther as my second boss. Everyday discussions with Günther not only helped me with my work, the discussions themselves were something that I was looking forward to everyday. He is easily approachable and would not hesitate to entertain my "stupid" questions without judgements. Again, couldn't have asked for a better second boss.

I extend my thanks to the master students worked in the PL lab, Mr. Thomas Exlager and Mr. Marcel Ney. Thomas worked for three months in the group as a part of his master thesis and I was able to learn a lot about certain evaluation methods from him. Marcel started his master thesis in the group and worked alongside me, he made the lab better with his excellent labview skills and I could learn a lot from him. I am grateful for everything they have taught me.

There are several people who worked alongside me in the PL lab. I learned valuable skills, characters etc. from all of these wonderful people. It is only fair to acknowledge them here by spelling out their names. Dr. Roland Kozubek, Dr. Daichi Okada, Mr. Osamu Oki, Ms. Sae Nakajima, Ms. Airong Qiagedeer, Mrs. Kornelia Huba, Mr. Dennis Oing, Mr. Vasilis Dergianlis, Ms. Reelika Kaumpmees, and Prof. Dr. Martin Mittendorf. I am thankful to all these wonderful people.

This thesis wouldn't have been possible without our collaborators who provided us with excellent samples. I would like to thank Prof. Dr. Uwe Kortshagen from university of Minnesota, USA for the silicon nanoparticles. I thank Dr. Cecilia Mattevi, Dr. Francesco Reale, Dr. Roland Kozubek and Prof. Dr. Marika Schleberger for the WS<sub>2</sub> monolayers and the xenon ion irradiation measurements on the monolayers. Last but not least, I would like to thank Prof. Dr. Yohei Yamamoto and Dr. Daichi Okada for the organic semiconductor micro-rods.

I was fortunate enough to have excellent colleagues, both present and past. Dr. Daniel Braam, Dr. Annika Kurzman, Mr. Kevin Eltrudis, Ms. Fangfei Li, Mr. Mathias Bartsch, Mr. Jens Kerski, Mr. Amran Al-Ashouri, Mrs. Jennifer Stein, Mrs. Pia Lochner, Mr. Dennis Oing, Mr. Sebastian Tigges, Mr. Vasilis Dergianlis and Mrs. Marion Hannemon, I would like to thank all

---

these amicable people who provided an ideal work environment.

I would like to single out Fangfei and Jens for lending their ears during the tough times I had.

My gratitude towards Prof. Dr. Gerd Bacher, my second supervisor for the invaluable discussions during the yearly meetings and the encouraging words.

Football has been an integral part of my life and has provided me with many friends. Likewise, I have been fortunate to continue playing football here and made friends outside work. I thank all my football friends who made my Ph.D. time more enjoyable and such interaction outside work is imperative to cheer oneself up.

I would also like to thank my friends Gaurav and Tanumoy who helped me during my low points of Ph.D. life.

Last but not least, I would like to thank my family, my sister Asst. Prof. Eluckiaa Asai, my mother Elilselvi Kasi and my father Asaithambi Manickam for all the love they have given me.

# Declaration

Die Gelegenheit zum vorliegenden Promotionsverfahren ist mir nicht kommerziell vermittelt worden. Insbesondere habe ich keine Organisation eingeschaltet, die gegen Entgelt Betreuerinnen und Betreuer für die Anfertigung von Dissertationen sucht oder die mir obliegenden Pflichten hinsichtlich der Prüfungsleistungen für mich ganz oder teilweise erledigt. Hilfe Dritter wurde bis jetzt und wird auch künftig nur in wissenschaftlich vertretbarem und prüfungsrechtlich zulässigem Ausmaß in Anspruch genommen. Mir ist bekannt, dass Unwahrheiten hinsichtlich der vorstehenden Erklärung die Zulassung zur Promotion ausschließen bzw. später zum Verfahrensabbruch oder zur Rücknahme des Titels führen können.

---

Ort, Datum, Name